CHARACTERIZATION OF EARLY-STAGE MATERIAL DAMAGE IN CEMENT-BASED MATERIALS USING NONLINEAR ULTRASOUND

A Dissertation
Presented to
The Academic Faculty

by

Gun Kim

In Partial Fulfillment
of the Requirements for the Degree
Doctor of Philosophy in the
School of Civil and Environmental Engineering

Georgia Institute of Technology
December 2016

CHARACTERIZATION OF EARLY-STAGE MATERIAL DAMAGE IN CEMENT-BASED MATERIALS USING NONLINEAR ULTRASOUND

Approved by:

Dr. Laurence J. Jacobs, Co-Advisor
School of Civil and Environmental Engineering
The George W. Woodruff School of Mechanical Engineering
Georgia Institute of Technology

Dr. Kimberly E. Kurtis, Co-Advisor
School of Civil and Environmental Engineering
Georgia Institute of Technology

Dr. Jin-Yeon Kim
School of Civil and Environmental Engineering
Georgia Institute of Technology

Dr. Karim Sabra
The George W. Woodruff School of Mechanical Engineering
Georgia Institute of Technology

Dr. Yang Wang
School of Civil and Environmental Engineering
Georgia Institute of Technology

Date Approved: November 2, 2016

To My Mom, Dad, and Sister

ACKNOWLEDGEMENTS

My deepest gratitude goes to three amazing advisors – Dr. Laurence J. Jacobs, Dr. Kimberly E. Kurtis, and Dr. Jin-Yeon Kim.

First of all, I will be forever indebted to my advisor and friend, Dr. Laurence J. Jacobs for his encouragement over the years and support during all of the challenges I have ever faced, and the success of my Ph.D. could not have realized without his guidance. He showed me an example of what the noble professor was in both the School of Civil and Environmental Engineering and the George W. Woodruff School of Mechanical engineering.

I would like to express my sincerest thanks to my advisor, Dr. Jin-Yeon Kim. Having learned under his groundbreaking direction always helped me not only immerse myself in the areas of nonlinear ultrasound and applied mechanics, but engrave ethical values for being a true scholar in my heart.

My deepest gratitude goes to my advisor, Dr. Kimberly E. Kurtis, for introducing me the beautiful world of concrete. I have been lucky enough to have the discussion, and advice from her. Her insightful direction and guidance were the fundamental to the achievement of my Ph.D. research.

Many thanks have to go to Dr. Karim Sabra, for sharing his encyclopedic knowledge on acoustics, and wave propagation with me. He enabled me to receive M.S. degree in the George W. Woodruff School of Mechanical Engineering. I would like to thank Dr. Yang Wang for reviewing my thesis and for serving on my Ph.D. committee. Special thank is owed to Dr. John S. Popovics at the University of Illinois at Urbana-

Champaign, for his ideas and insights that resulted in bettering my efforts to conduct the research in the area of concrete NDE. Particularly, I was very honored to interact with Dr. T.J. Ulrich at Los Alamos National Laboratory, Dr. Joseph Turner at the University of Nebraska-Lincoln, and Dr. Jianmin Qu at Tufts University. They inspired me to learn the experimental and theoretical aspects of nonlinear acoustics and helped me develop my academic career.

My sincere gratitude goes to my former advisor Dr. Moon-Kyum Kim, Dr. Tae-Sup Yun, Dr. Hyoungkwan Kim, Dr. Tong Seok Han, Dr. Jung-Hoon Kim, Dr. Kyoungsoo Park, and Dr. Yun Mook Lim. Particularly, Dr. Moon-Kyum Kim provided me with insight into the applied mechanics and inculcated me with passion for pursuing doctoral study.

I would like to thank the following funding sources for their financial support of this research − the Electric Power Research Institute. In particular, I appreciate Dr. Maria Guimaraes and Dr. James Wall of the EPRI, Dr. Yann Le Pape of Oak Ridge National Laboratory, and Dr. Eric Giannini at the University of Alabama for providing me great environment where I could successfully conduct the research projects.

The School of Civil and Environmental Engineering and the George W. Woodruff School of Mechanical Engineering at Georgia Tech have truly provided me a collaborative environment where I could pursue the multidisciplinary research. I would especially like to thank Dr. Giovanni Loreto for all his open mentorship.

It has been a great experience working with all of the students in both NDE and Material laboratories. Many thanks to the “generations of Germans" from Stuttgart University, Germany. Special thanks thereby goes to Sebastian Thiele, Fabian Schempp, Anne Romer, Florian Morlock, Tobian Oberhardt, and Daniel Grün for having fruitful

discussions regarding nonlinear acoustics and ultrasound. Thank you to the current and former members of the NDE Lab. (Katie Matlack, Chi-Won In, David Torello, Mehdi Rashidi, Katie Scott, Fuchs Brian, Alexander Lakocy, Maggie Smith, and Kevin Arne), for the research assistance and friendship. I also appreciate groupmates in the Material Lab. (Elizabeth Nadelman, Alvaro Paul, Bradley Dolphyn, Lisa Burris, Behnaz Zaribaf, and Prasanth Alapati) providing me such an excellent atmosphere.

Thank you to Ji Min for being my constant support, and making me happy through every step of this journey.

Last but absolutely not least, I would like to express my sincerest gratitude to my family - Mom, Dad, Mi Ra, In Chul, and beautiful niece E.L., for their endless love, and prayer. Their unlimited support is the unique force that drives me to accomplish everything I set in mind.

TABLE OF CONTENTS

LIST OF TABLES

LIST OF FIGURES

LIST OF SYMBOLS AND ABBREVIATIONS

α	Hysteretic parameter
a	Attenuation coefficient
ɑ	Radius of transducer
β	Acoustic nonlinearity parameter
δ_{ij}	Kronecker delta
ε_{kl}	Strain tensor
θ_{crit}	Critical angle
λ_L, λ_S, λ_R	Wavelength of longitudinal, shear and Rayleigh surface wave
λ, μ	Lamé's constants
v	Poisson's ratio
ρ	Density
σ_{ij}	Stress tensor
σ_{ij}^{PK}	First Piola-Kirchhoff stress tensor
σ (f)	Dissipation rate
φ	Scalar potential (Helmholtz decomposition)
ψ	Vector potential (Helmholtz decomposition)
ω	Fundamental angular frequency
A	Undeformed body in Lagrangian coordinate
A^*	Deformed body in Eulerian coordinate
A_1	Fundamental harmonic amplitude
A_2	Second harmonic amplitude
A, B	Non-trivial parameters

b_j	Body force tensor
C_P	Longitudinal wave (P-wave) velocity
C_R	Rayleigh surface wave (R-wave) velocity
C_S	Shear wave (S-wave) velocity
C_{ijkl}	Fourth-order elastic stiffness tensor
C_{ijklmn}, M_{ijklmn}	Higher-order elastic tensor
C_{111}	Third-order elastic constant in Voigt notation
D	Diffusivity
d	Unit vector
E	Young's modulus
E_{ij}	Green strain tensor
e_i	Unit normal vector
F_{ij}	Second-order deformation gradient tensor
f	Frequency
I	Second-order identity tensor
k_L, k_S, k_R	Wavenumber of longitudinal, shear and Rayleigh surface wave
k_{Si}, k_{Lr}, k_{Sr}	Wavenumber of incident shear, reflected longitudinal and shear wave
P	Spectral source energy density
p	Unit propagation vector
S	Surface
s	Normalized frequency
t	Time
t_j	Traction tensor
u_i	Displacement tensor
V	Volume

x	Position vector
x, x^*	Reference (Lagrangian) and current (Eulerian) configuration
AE	Acoustic emission
ASR	Alkali-silica reaction
AC	Air-coupled
CWI	Coda wave interferometry
DAET	Dynamic Acoustoelastic Testing
DRUW	Dry rodded unit weight
FEM	Finite element method
FFT	Fast Fourier Transform
FM	Fineness modulus
ITZ	Interfacial transition zone
MSA	Maximum size of aggregate
NCA	Non-reactive coarse aggregate
NDE	Nondestructive evaluation
NDT	Nondestructive testing
NFA	Non-reactive fine aggregate
NIRAS	Nonlinear impact resonance acoustic spectroscopy
NLA	Nonlinear acoustics
NLU	Nonlinear ultrasound
NRUS	Nonlinear resonant ultrasound spectroscopy
QXRD	Quantitative X-ray diffraction
RFA	Reactive fine aggregate
RH	Relative humidity
SHG	Second harmonic generation

SHM	Structural health monitoring
SNR	Signal-to-noise ratio
SRA	Shrinkage-reducing admixture
SSD	Saturated surface dry
SSM	Scaling Subtraction Method
TGA	Thermogravimetric analysis
TOF	Time-of-flight
TS	Time shift
UPV	Ultrasonic pulse velocity

SUMMARY

The assessment of civil infrastructure like concrete containment vessels, dams, and bridges requires ability to nondestructively characterize their damage state, and thus reducing rehabilitation costs, and enhancing public safety. A critical step in achieving this goal is the ability to monitor microcrack development, since these microscale defects directly affect the early-stage material performance, and thus the entire service life of concrete civil infrastructure. Although excellent progress has been made in the development of nondestructive evaluation (NDE) and structural health monitoring (SHM) techniques for concrete, the evaluation of microstructural condition is still challenging due to the low sensitivity of the conventional NDE parameters.

Nonlinear ultrasonic (NLU) and nonlinear acoustic (NLA) techniques have attracted significant attention in the last decades, since unlike conventional linear parameters such as wave velocity and attenuation, nonlinearity parameters have great sensitivity to changes in the microstructure of cement-based materials. Previous research has helped establish the feasibility of nonlinear techniques for monitoring the early-early damage state of cement-based materials [1–6] and successfully demonstrated that the NDE of microscale degradation in concrete is possible.

In spite of significant progress in the area of NLU and NLA, several issues on the NDE of concrete are still open for research. For instance, it is not fully validated that the existing nonlinear techniques are indeed effective for monitoring in-service concrete structures since the feasibility of these techniques is only limited to small size concrete specimens – the detection of microscale defects in the full-scale concrete structures still

poses problems. Another issue is that those concrete structures allow only limited access due to their complex geometry; a local measurement technique should be implemented in this complex measurement condition.

To overcome the current issues in the application of NLU to concrete, this research develops an SHG technique using Rayleigh surface waves in the frequency range of 40 to 120 kHz. A non-contact, air-coupled detection technique is developed and implemented to characterize the damage state in cement-based materials. One objective of this research is to demonstrate the feasibility and applicability of the proposed SHG setup for monitoring microcracking development in concrete. Then, using the acoustic nonlinearity parameter, β from the SHG setup developed, five independent tasks are conducted: (1) monitoring the effect drying shrinkage on microcracking development, (2) understanding the role of SRA in mitigating drying shrinkage, (3) quantifying the state of carbonation in concrete specimens; (4) examining the state of alkali-silica reaction (ASR) induced damage at two different times in large-scale concrete slabs, and (5) developing an in situ nonlinear technique to quantify the development of microcracks induced by creep and cyclic loading. Through a comparison with the experimental results, a comprehensive understanding of the early-stage material state in concrete is reviewed by the acoustic nonlinearity parameter, β.

CHAPTER 1. INTRODUCTION

1.1 Motivation and Objective

The "grand challenge" for sustainable and resilient structural systems is to satisfy multiple and conflicting requirements for optimal performance. The 2013 report card of the American Society of Civil Engineers (ASCE) [7] urges an enhancement of the service life of civil infrastructure: the overall grade of America's infrastructure is estimated to D+, while the grade of bridges is C+. Note that a $20.5 billion investment is estimated to be needed in order to eliminate the deficient backlog by 2028. While the service life of civil infrastructure can possibly be assessed using a series of destructive tests, this is not a practical option. Oftentimes it is very difficult or almost impossible to theoretically model the exact wear or damage that has occurred in a structure.

Of particular interest is the development of nondestructive evaluation (NDE) methods since NDE techniques can assess the functionality of in-service structures and monitor the internal degradation and changes of material properties of concrete in a rapid, and cost-efficient manner [8,9]. Recent trends in the nondestructive evaluation (NDE) and structural health monitoring (SHM) are moving into the realm of simple and reliable in-situ monitoring with high-accuracy material characterization. Of particular importance for developing NDE techniques is the assessment of concrete, not only because a great portion of the infrastructure is composed of concrete, but also because the composition of concrete is prone to deterioration by atmospheric conditions, mechanical loads, and any catastrophic disasters. Therefore, the significance of monitoring small-scale damage in concrete that represents early-stage damage state (nano to microscale) cannot be overemphasized.

However, a major bottleneck is the gap between knowledge of the fundamentals of physical/chemical phenomena in engineering materials and the needs for engineering practice as applied to in-service structures.

The current development of concrete NDE exhibits several challenges that must be overcome. For instance, the impact-echo method [10–12] is known as a powerful field-applicable technique. Some examples demonstrate that this method can detect the presence of macroscale damage, e.g., internal air-filled flaws in large-scale concrete structures. On the other hand, it can be difficult to sense the early-stage damage state with impact-echo methods. This is due to the low sensitivity, meaning that the wavelength of the excited signal is much larger than microscopic scale damage. Similarly, linear ultrasonic pulse velocity (UPV) and attenuation measurements show that their sensitivity is only capable of monitoring large cracks and voids in concrete due to the lack of sensitivity and high scattering effects. That is, these techniques are not capable of detecting small size damage evolution.[13–16]

For these reasons, trends in concrete NDE move beyond these traditional approaches, and in recent decades, new NDE techniques have emerged to overcome the described limitations. Nonlinear ultrasonic methods have the ability to meet the requirements of early-stage damage state detection in concrete. It is well-known that nonlinear ultrasound (NLU) provides a quantitative damage parameter that is sensitive to microstructural features – the damage parameter is directly related to the material's nonlinear elastic behavior [1,3,17–20]. It is worthy of notice that new nonlinear ultrasonic parameters that can scrutinize the complex microscale or nanoscale damage evolution has been developed by Johnson et al. [21,22], Guyer et al. [23], Nagy et al. [24], and Canterell

et al. [25]. Such remarkable progress has eventually opened up the precise material characterization of granular medium, and metallic materials. Furthermore, recent research [20,22,25–28] has highlighted that the nonlinear methods are capable of establishing a correlation between the early-age damage evolution and the nonlinear constitutive relationship.

Based on them, nonlinear NDE methods have been applied to assess the small scale defects in concrete. For instance, Chen et al. [4], and Payan et al. [29] introduced the Nonlinear Impact Resonance Acoustic Spectroscopy (NIRAS) technique, and Nonlinear Resonant Ultrasound Spectroscopy (NRUS) technique respectively, and demonstrated that the nonlinearity parameter allows an interpretation of the microscale damage evolution such as ASR [19], freezing-thawing [2] and thermal damage [30] in concrete. Although all of these methods are effective in evaluating material nonlinearity, however their application to the field has not been reported yet. Above all, these techniques which measure resonance frequencies are naturally not applicable to large-scale specimens or in-service civil infrastructure since the magnitudes of an impact is limited only to small size specimens. Additionally, the fact that access to both sides of the specimen is needed further limits their practical application for the in-situ interrogation of civil structures that allow only limited access due to their complex geometry.

The objective of this research is to characterize early-stage material damage in concrete over a range of drying shrinkage, shrinkage mitigation (through the use of shrinkage-reducing admixture), self-healing (by carbonation), alkali-silica reaction (ASR), and sustained and cyclic loading using the nonlinear ultrasonic technique of second harmonic generation (SHG). Quantitative material characterization is then carried out using

SHG measurements, and the evolution of the micro-scale damage state is discussed. Two specific objectives are as follows:

Objective 1: Determine the feasibility and applicability of SHG technique to quantify microscopic features in concrete.

Recognizing the lack of the ultrasonic results on microstructural features in concrete, this research develops second harmonic generation (SHG) in Rayleigh surface waves to nondestructively quantify microcracks. For the generation and detection of nonlinear Rayleigh surface waves, a wedge transmitter (50 kHz) and a specially designed air-coupled receiver (100 kHz) are implemented. The acoustic nonlinearity parameter, β is measured using the designed setup. Then, three types of material phenomena including drying shrinkage, shrinkage mitigation, and carbonation are nondestructively characterized by monitoring the acoustic nonlinearity parameter, β.

Objective 2: Develop "in-situ" SHG technique to monitor microcracking development in concrete subjected to sustained and cyclic loading.

Having established the accuracy and sensitivity of SHG to characterize microscale damage in concrete, the objective of this portion is to develop a procedure capable of in situ monitoring of micro-scale damage in both large-scale components and concrete subjected to sustained and cyclic loading. First, alkali-silica reaction (ASR) damage is quantified using the full-scale concrete slabs to demonstrate the potential for localized

damage evaluation of in-service concrete structures. Next the SHG setup is modified to make measurements of β in cylindrical concrete specimens. This modification makes it possible to make in situ measurements of concrete cylinders under sustained and cyclic loading. Using this approach, a number of key material issues such as elastic recovery and progressive microcracking development are quantitatively investigated. Addtionally, the influence of critical environmental parameters such as temperature and relative humidity (RH) on the microstructure is studied.

1.2 Structure of Thesis

The structure of this dissertation is organized as follows. The first chapter introduces the motivation and significance of developing nonlinear ultrasonic techniques to nondestructively monitor damage in concrete, and provides two main objectives of this research. Chapter 2 presents the fundamentals of wave propagation in solids, and the properties of Rayleigh surface waves. Chapter 3 provides a review of linear and nonlinear techniques for concrete NDE, and concrete performance. Chapter 4 explains the principle of second harmonic generation in Rayleigh surface waves, and demonstrates the feasibility of the SHG measurement for monitoring microscale material state in concrete, and the effect of shrinkage-reducing admixture (SRA) on mitigating shrinkage cracking in hardened concrete. Chapter 5 evaluates carbonation reaction and its role in enhancing the durability of concrete as a self-healing mechanism. Chapter 6 quantifies the phenomenon of drying shrinkage, and provides a comprehensive understanding of microstructural condition in hardened concrete by the influence of both shrinkage-reducing admixture

(SRA) and carbonation. Chapter 7 focuses on the assessment of ASR damage in large-scale concrete structures. Chapter 8 introduces new in-situ NDE technique, and presents experimental evidences on understanding microcracking development due to the creep and cyclic loading. Finally, Chapter 9 gives an insight in the material characterization of hardened concrete, and provides a contribution of this research, and recommendations for future research in concrete NDE.

CHAPTER 2. BACKGROUND INFORMATION

This chapter first presents the fundamentals of wave propagation in a continuous medium. With the mathematical derivation of the linear wave equation, the associated phenomena including mode conversion, the principle of Rayleigh surface waves will be derived.

2.1 Wave Propagation in Solids

The derivation of linear wave equation of motion builds the starting point of nonlinear elastic wave behavior that enable understanding of physical/chemical phenomena in concrete. This chapter discusses the fundamentals of linear wave propagation in isotropic, and macroscopic solids based on Malvern [31], Achenbach [32], and Viktorov [33]. Then, by considering nonlinear constitutive relationship, the acoustic nonlinearity parameter, β in the propagating Rayleigh surface waves is derived.

2.1.1 Wave Equation for a Linear Elastic Solid

Cauchy's equation of motion: The derivation of the equation of motion starts with Newton's second law. Figure 2.1 describes a body in an elastic regime subjected to the traction and gravitational force. The integral form of the balance of linear momentum in Eulerian for a body with the surface S, and density ρ enclosing volume V and can be written as

$$\int_V \rho \ddot{u}_i dV = \int_S t_j dS + \int_V \rho b_i dV \,. \tag{2.1}$$

where, t_j is the traction, b_j the body force, and u_i the displacement tensor. With Cauchy's stress equation, the traction term in Eq. (2.1) is expressed in terms of the Cauchy's stress, σ_{ij} and the outward unit vector, n_i.

$$\int_V \rho \ddot{u}_i dV = \int_S \sigma_{ij} n_i dS + \int_V \rho b_i dV \tag{2.2}$$

Using the divergence theorem, the surface integral form can be converted to the volume integral form and thus, Eq. (2.2) is expressed in a unified volume integral form.

$$\int_V \rho \ddot{u}_i dV = \int_V \sigma_{ij,j} dV + \int_V \rho b_i dV \tag{2.3}$$

Thus, Eq. (2.3) is rewritten as

$$\int_V (\sigma_{ij,j} + \rho b_i - \rho \ddot{u}_i) dV = 0 \,. \tag{2.4}$$

Since this form holds for every arbitrary volume, this results in Cauchy's first law of motion following as

$$\rho \ddot{u}_i = \sigma_{ij,j} + \rho b_i \,. \tag{2.5}$$

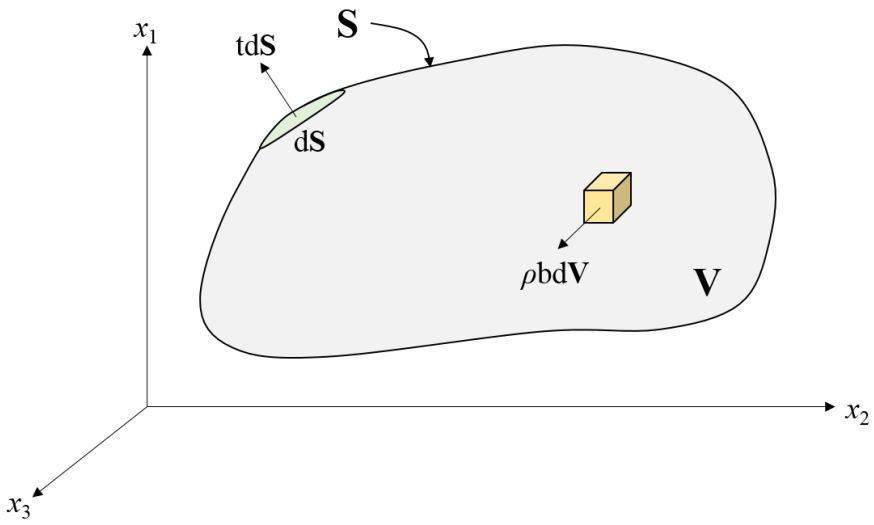

Figure 2.1. Balance of momentum (Cauchy's first law of motion).

Linear stress and strain: The general constitutive relationship is expressed in terms of stress σ_{ij}, strain ε_{kl}, and the fourth-order elastic stiffness tensor, C_{ijkl}.

$$\sigma_{ij} = C_{ijkl}\ \varepsilon_{kl} \tag{2.6}$$

C_{ijkl} having 81 components describes the mechanical properties of the material. For the case of a linear isotropic material, the stiffness tensor can be simplified as

$$\sigma_{ij} = \lambda \varepsilon_{kk} \delta_{ij} + 2\mu\varepsilon_{ij}\,. \tag{2.7}$$

where, λ, and μ are the Lamé's constants.

$$\lambda = \frac{E\nu}{(1+\nu)(1-2\nu)}, \qquad \mu = \frac{E}{2(1+\nu)} \tag{2.8}$$

Note that E represents the Young's modulus and ν the Poisson's ratio. Since the infinitesimal strain tensor is formed following the relationship,

$$\varepsilon_{ij} = \frac{1}{2}(u_{i,j} + u_{j,i}) \tag{2.9}$$

Linear elastic wave equation: Combining Eq. (2.7) and Eq. (2.9) yields Navier's equation of motion with the displacement field.

$$\rho\ddot{u}_i = \mu u_{i,jj} + (\lambda + \mu)u_{j,ji} \tag{2.10}$$

This form neglects the body force action on the arbitrary volume and can be read as vector from instead of index notation

$$\rho\ddot{u} = \mu\nabla^2 u + (\lambda + \mu)\nabla\nabla \cdot u \tag{2.11}$$

The most common method to achieve a solution for Eq. (2.11) is to use the Helmholtz decomposition (2.12), which uncouples the displacement filed u into the gradient of the scalar potential, φ and the curl of the vector potential, ψ

$$u = \nabla\varphi + \nabla \times \psi \qquad where\ \nabla \cdot \psi = 0\,. \tag{2.12}$$

Plugging Eq. (2.12) into Navier's equation of motion, Eq. (2.10) yields two PDEs.

$$\nabla^2\varphi = \frac{1}{C_P^2}\ddot{\varphi}, \qquad \nabla^2\psi = \frac{1}{C_S^2}\ddot{\psi} \tag{2.12}$$

where C_P, and C_S denotes the longitudinal (P-wave) and shear (S-wave) wave velocity, respectively. Note that both velocities are only dependent on elastic constants (Lamé's constants) and density, and thus Eq. (2.12) can be defined by

$$C_P = \sqrt{\frac{\lambda + 2\mu}{\rho}}, \qquad C_S = \sqrt{\frac{\mu}{\rho}}. \tag{2.13}$$

With the elastic material constants, C_P describes the propagation of dilatational disturbances, and C_S indicates the propagation of rotational distortion.

Plain wave propagation in an elastic medium: A displacement of a plain wave propagating with the velocity *c* can be mathematically described as:

$$u = f(x \cdot p - ct)d \tag{2.14}$$

with the unit vector *d*, the position vector *x*, the unit propagation vector *p*, and time *t*. Substituting Eq. (2.14) into Eq. (2.11) leads to

$$(\mu - \rho c^2)d + (\lambda + \mu)(p \cdot d)p = 0 \tag{2.15}$$

The Eq. (2.15) is only satisfied in two ways, either

$$d = \pm p \quad or \quad p \cdot d = 0 \tag{2.16}$$

1) If the unit propagation vector, p is parallel to the unit vector d, then the first relationship in Eq. (2.16) is only valid, and this matches up with the propagation direction parallel to a particle motion, meaning a longitudinal wave propagation.

2) If the unit propagation vector, p is perpendicular to the unit vector d, then the solution of Eq. (2.15) is $p \cdot d = 0$, and this describes the propagation direction perpendicular to a particle motion, i.e., a propagating shear wave.

Harmonic wave: Harmonic plane wave is a special mathematical form of the plane waves propagating through an elastic medium, providing a solution of the complex phenomena between the propagating waves and the medium. A typical equation of the harmonic form is given by

$$f(x \cdot p - ct) = \exp[ik(x \cdot p - ct)]. \tag{2.17}$$

where, k ($=\omega / c = 2\pi / \lambda$) is the wavenumber, ω the angular frequency of the wave, and λ the wavelength. Given an amplitude A as a complex form, a general solution for this equation is

$$u = A\exp[ik(x \cdot p - ct)]d\,. \tag{2.18}$$

Mode conversion, transmission, and reflection at a boundary: In a general case of in-plane motion, each incident wave has two reflected and two refracted waves at a solid-solid interface due to the mode conversion. As shown if Figure 2.2, when an incident plain wave, $P^{(o)}$ (P- or SV-wave) with the wavenumber, k_o hit a boundary between two solids where $\sigma_{11} = \sigma_{12} = 0$, it causes both a reflected P-wave, $P^{(1)}$ with the wavenumber k_{Lr}, and a reflected SV-wave, $P^{(2)}$ with the wavenumber k_{Sr}. Note that $\theta_0 = \theta_1$ and $\theta_1 > \theta_2$. According to Snell's Law, the angles can be determined with the velocity of each material and the following relationship can be established.

$$k_0 \sin(\theta_0) = k_{Lr} \sin(\theta_1) = k_{Sr} \sin(\theta_2) \tag{2.19}$$

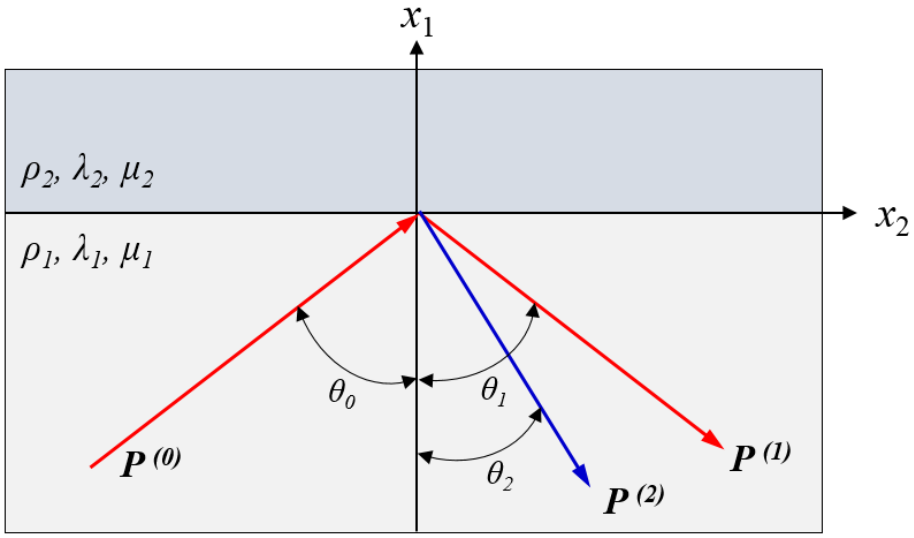

Figure 2.2. Reflection of P-wave incident at a solid interface.

Of particular importance in the reflection of P-wave incident is the generation of Rayleigh surface waves because the Rayleigh surface waves can be only excited when the incident P-wave hits the boundary at a critical angle (θ_{crit}) where both reflected P- and S-waves combine together and propagate through the interface with a single wave form. Eq. (2.20) describes how to determine the critical angle. In a design of the experimental setup, the angle of a transmitter or receiver is calculated based on Eq. (2.20).

$$\theta_{crit} = \arcsin\left(\frac{C_S}{C_L}\right) \tag{2.20}$$

2.2 Rayleigh Surface Waves

Theory of Rayleigh surface waves: Consider a two dimensional Rayleigh surface wave propagating along the x axis in an isotropic, macroscopically homogeneous, and linear elastic half space where z axis refers to the depth of the material. First, the displacement field of the propagating Rayleigh wave can be given by

$$u_x = Ae^{-bz}\, e^{i\{k_R(x-c_Rt)\}},$$
$$u_z = Be^{-bz}\, e^{i\{k_R(x-c_Rt)\}}. \tag{2.21}$$

where, C_R is the phase velocity of the Rayleigh surface wave, and k_R the wavenumber. Since both displacement components satisfy Eq. (2.11), thus the solution of the non-trivial parameters A and B can be obtained as

$$(C_L^2 b^2 - k_R^2(C_L^2 - C_R^2))(C_S^2 b^2 - k_R^2(C_S^2 - C_R^2)) = 0\,. \tag{2.22}$$

Only two solutions for Eq. (2.22) are physically acceptable as shown in Eq. (2.23), thereby providing the solutions for the non-trivial parameters A, and B.

$$b_1 = k_R\left(1 - \frac{C_R^2}{C_L^2}\right)^{1/2},$$
$$b_2 = k_R\left(1 - \frac{C_R^2}{C_S^2}\right)^{1/2} \tag{2.23}$$

$$\left(\frac{B}{A}\right)_1 = -\frac{b_1}{ik_R},$$
$$\left(\frac{B}{A}\right)_2 = \frac{ik_R}{b_2} \tag{2.24}$$

Then, using both Eq. (2.23) and (2.24), Eq. (2.21) can be rewritten as

$$u_x = (A_1 e^{-b_1 z} + A_2 e^{-b_2 z}) e^{i\{k_R(x - c_R t)\}},$$
$$u_z = \left(-\frac{b_1}{ik_R} A_1 e^{-b_1 z} + \frac{ik_R}{b_2} A_2 e^{-b_2 z}\right) e^{i\{k_R(x - c_R t)\}}. \tag{2.25}$$

Using the boundary condition at the interface, $\sigma_{xz} = \sigma_{zz} = 0$, $z = 0$, the relationship between A_1 and A_2 are obtained as shown in Eq. (2.26), and this leads to the displacement formulation of the propagating Rayleigh surface waves.

$$A_2 = -\frac{2b_1 b_2}{k_R^{\,2} + b_2^{\,2}} A_1 \tag{2.26}$$

$$u_x = A_1 \left(e^{-b_1 z} - A_2 \frac{2b_1 b_2}{k_R^{\,2} + b_2^{\,2}} e^{-b_2 z}\right) e^{i\{k_R(x - c_R t)\}},$$
$$u_z = iA_1 \frac{b_1}{k_R} \left(e^{-b_1 z} - \frac{2k_R^{\,2}}{k_R^{\,2} + b_2^{\,2}} e^{-b_2 z}\right) e^{i\{k_R(x - c_R t)\}}. \tag{2.27}$$

The following characteristic equation provides the phase velocity of the Rayleigh wave at $z = 0$ [32,33].

$$\left(2-\frac{C_R^2}{C_S^2}\right)^2-4\left(1-\frac{C_R^2}{C_L^2}\right)^{1/2}\left(1-\frac{C_R^2}{C_S^2}\right)^{1/2}=0 \tag{2.28}$$

An approximate solution for Eq. 2.28 holds the relationship shown in Eq. (2.29).

$$C_R \approx \frac{0.862+1.14\,\nu}{1+\nu} C_S \tag{2.29}$$

It is noticeable that the Eq. (2.28) is independent on the wavenumber k_R, which supports the non-dispersive characteristic at the free surface of an elastic half-space. Additional note that the particles of the medium at the surface show an ellipsoidal motion with the counterclockwise direction, while the direction of motion turns into the clockwise with increasing depth.

CHAPTER 3. LITERATURE REVIEW

With an objective of understanding existing nondestructive evaluation (NDE) techniques for evaluating damage in concrete, this chapter presents a thorough overview of the conventional linear NDE techniques, the nonlinear NDE techniques, and the progress toward the material characterization, respectively. Then, as a target of evaluation, mechanical and chemical phenomena that affect early-stage material state in concrete are reviewed.

3.1 Review of Linear NDE Techniques

It is well known that linear ultrasonic techniques are well tuned to evaluate the macroscopic damages in concrete such as the visible cracks, and changes in material properties. Using the wave theory in Chapter 2.1, a number of researcher have been successfully developed a series of the linear ultrasonic techniques such as ultrasonic pulse velocity, impact echo, attenuation coefficient, and diffuse ultrasound.

3.1.1 Ultrasonic Pulse Velocity (UPV)

The idea behind the UPV method is to measure the time-of-flight of the elastic waves propagating through concrete [8,14,15,34]. The phase velocity is calculated by dividing path length by the measured travel time. During this travel, if the excited waves pass through any macro-scale cracks or flaws in the material, this causes the delayed arrival time and thus the decrease in the phase velocity. It is well demonstrated that this technique

is capable of sensing the internal cracks and crack depth [35]. Furthermore, by solving Eq. (2.13), the material properties can be inversely obtained. The previous work [36] has well validated that the effective frequency range for measuring the velocity for concrete is approximately from 0 to 100 kHz. Most of all, the instrumentation is simple, thereby easy to measure the velocity.

However, there are some physical restriction in the UPV technique. First, the wavelength of these frequencies is too large to sense small size defects such as air void. Second, if the wavelength is decreased, there must be the significant scattering effect due to the coarse aggregates. In addition, recent research [37] has reported that the change in the phase velocity due to the microcracking is comparable to the measurement error. Due to these reasons, monitoring of early-stage material damage by using the UPV method is almost impossible.

3.1.2 Impact Echo

The principle of this technique [10,38] is that a stress wave (below 100 kHz frequency) generated by mechanical impact experiences the multiple reflection and thus reveals the position, and depth of flaws, delamination, and any internal damage progression in concrete. Outstanding development that implemented air-coupled sensing technique with broad frequency response has been achieved by Zhu et al [11] and Kee et al [12]. In spite of these advantages, this method is still confined to monitor the macroscopic damages and furthermore, it requires a highly skilled technician to precisely interpret the recorded signals [36].

3.1.3 Pulse-Echo Method

The basic concept of the pulse-echo method is closely similar to that of impact-echo method. However, while the impact-echo technique relies on a hammer or steel ball, the pulse-echo method uses the ultrasonic transducers capable of controlling the amplitude of the generated impact [10]. This method use the transmitter and receiver mounted on the same side of concrete specimen within the frequency range of 0 to 200 kHz; the receiver detects the reflected waves from both boundary and the existence of a defect. Recent research by Hoegh et al. [39] has highlighted that the pulse-echo method with advanced array system could find location of defects with an image of internal structure. However, similar to the UPV method, the sensitivity or resolution of this technique has not been allowed to detect the microscale flaws in concrete. General acceptance is that although the pulse-echo based approach has great potential for the inspection of in-service concrete structures, but it is not still applicable for the precise material characterization.

3.1.4 Surface Wave Method

With increasing needs for the inspection of in-service structures, developing NDE technique based on surface waves can be more practical option since a number of chemical reaction such as ASR [40], carbonation [41], and sulfate attack [42] initiates from the surface in concrete. The surface wave-based techniques are well-suited to evaluate material properties such as the density, Poisson's ratio, and the shear modulus at the surface. Thus, investigation of concrete using surface waves is attracting interest, and thus have been extensively utilized to characterize delamination and cracks near surface [35,43–45] .

However, due to the fact that the penetration depth of surface waves is on the order of a wavelength, monitoring deeper cracks where the location of cracks is larger than the wavelength is impossible. In addition, the higher the wavelength is, the lower the sensitivity to small scale defects is. With these reasons, linear ultrasonic NDE using surface waves is still challenging.

3.1.5 Attenuation coefficients

Attenuation is defined as a decay and diminution of the wave amplitude, followed by energy-conservation dissipation [46,47]. The characteristics of geometric spreading and material attenuation are appeared in the attenuation coefficients capable of detecting flaws in concrete with high sensitivity. Due to this advantage, extensive experimental and numerical results have been reported. For instance, Shah et al. [16,48] have investigated the ultrasonic attenuation in concrete subjected sustained and cyclic loading and demonstrated that the attenuation measurement is suitable to monitor the load-induced microcracking development. Philippidis et al. [48] have investigated the w/c effect using ultrasonic attenuation in concrete. Saint-Pierre et al. [49] have also demonstrated that the attenuation has great sensitivity to ASR-induced damages than the wave velocity. More advanced technique considering diffraction correction (beam spreading) is introduced by Ruiz et al. [50]. Kim et al. [51] have also developed a theoretical model for concrete using the dynamic effective medium theory and demonstrated that the attenuation coefficients from the proposed analytical model is well matched up with the experimental results. Owino et al, and Punurai et al. [52] have applied the attenuation measurement techniques

to cement paste and successfully characterized entrained air voids with the effect of size, volume fraction, grain size, and porosity. Recently, in an effort of understanding the sensitivity to micro-scale flaws such as microcracks, and voids, Kim et al. [37,53] has presented that the sensitivity of the attenuation coefficients for Rayleigh surface waves is approximately 3 times higher than that of the velocity. The equations for the attenuation with diffraction correction is expressed in Eq. (3.1), and Figure 3.1 describes the experimental setup for the attenuation measurement using the spectral ratio technique. Nevertheless, the ultrasonic attenuation method is wavelength limited. The wavelength always must be on the order of the damage for accurate (sensitive) detection. This literally dictates the use of high-kHz/low-MHz pulses in order to detect microscale damage, yet these high frequency pulses cannot guarantee avoiding the scattering problem the concrete microstructure, thus limiting their utility.

$$\alpha(\mathrm{f}) = \frac{ln\left[\frac{\mathrm{S}(\mathrm{z}_1)}{\mathrm{S}(\mathrm{z}_2)}\right] - ln\left[\frac{\mathrm{D}_\mathrm{R}(\mathrm{z}_1)}{\mathrm{D}_\mathrm{R}(\mathrm{z}_2)}\right]}{\mathrm{z}_2 - \mathrm{z}_1} \tag{3.1}$$

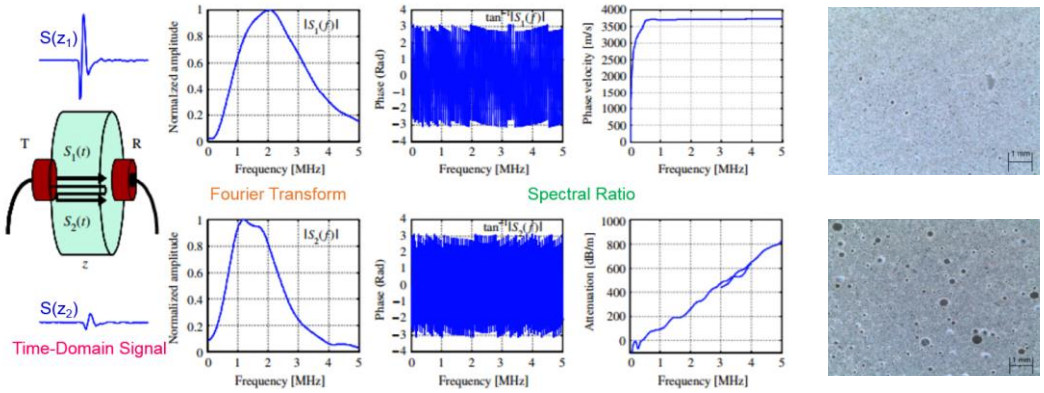

(a) Attenuation measurement using spectral ratio technique (b) Air-entrained voids

Figure 3.1. Experimental setup for attenuation measurement using spectral method [52].

3.1.6 Diffuse Ultrasound

Unlike other linear ultrasonic techniques, the diffuse ultrasound has a number of advantages [36,54–57]. Theoretical background on this technique is the time evolution of the spectral energy density in ultrasonic wave [36]. Eq. (3.2) explains the principle of diffuse ultrasonic parameters (diffusivity, and dissipation). Main advantage of this technique is that, if the spectral energy density of an ultrasonic wave fields is obtained, the use of high frequency can be available, regardless of the scattering effects. This means that monitoring the small size defects, or early-age damage state is possible in this technique. Also the fact that it is not necessary to consider an interaction of the propagating waves with geometry of the specimen guarantees the satisfactory quantification of defects in cement-based materials. Moreover, the instrumentation is simple and robust as compared to other linear ultrasonic methods.

$$D(f)\nabla^2\langle E(x,t,f)\rangle - \frac{\partial}{\partial t}\langle E(x,t,f)\rangle - \sigma(f)\langle E(x,t,f)\rangle = P(x,t,f), \forall x \in \mathrm{B} \qquad (3.2)$$

where, where, P(x,t,f) is the spectral source energy density, $D(f)$ is the frequency dependent diffusivity (m^2/s) and $\sigma(f)$ is the dissipation rate (1/s).

For those reasons, previous researchers have been paid attention to prove the applicability of the diffuse ultrasound to concrete. Weaver et al. [54] has first utilized this technique and found theoretical and experimental evidences demonstrating that diffusion of high frequency ultrasonic energy is suitable to detect the damage state in heterogeneous materials. Deroo et al. [57] has also measured the diffusivity and dissipation parameters from the diffuse approximation, thereby assessing the ASR damage in concrete, and In et

al. has shown cutting-edge developments in this field as shown in Figure 3.2. However, there also seems to exist some limitations in this technique. That is, this technique always requires a numerical or analytical evidence that supports the experimental results. As a result, the pure signal can be distorted, and thus the diffuse ultrasonic parameter can be manipulated by the analytical parameter.

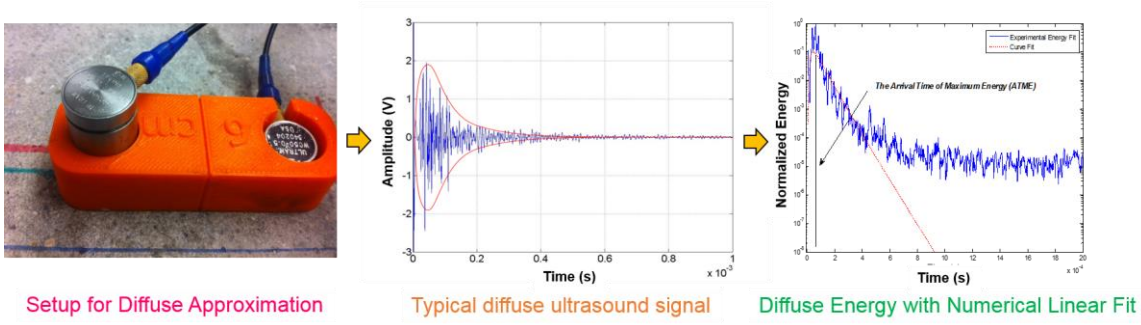

Figure 3.2. Experimental setup for diffuse ultrasound [36].

Recently, NDE using nonlinear wave propagation and dynamics is of growing interest as they can provide a damage indicator which, in turn, distinguishes the nano- to micro-scale damage level. Therefore, it is believed that the NLU techniques have the great potential to lead to the quantitative evaluation of microcracking development due to the load-induced damages in concrete.

3.2 Review of Nonlinear NDE Techniques

This section reviews the principles of a series of nonlinear NDE techniques, and their application to microcracking detection in cement-based materials. As described earlier, nondestructive evaluation (NDE) using nonlinear ultrasound/acoustics has been

extensively attractive since unlike the linear ultrasonic parameters such as wave velocity and attenuation, these nonlinear acoustic parameters have great sensitivity to the microstructural attributes of concrete [2,18,37,53,55,58–60]. Therefore, it can be stated that the nonlinear techniques allow the quantification of early-stage material damage. Also, it is well-described in the literature that the nonlinear elastic behavior can be observed in different ways including second harmonic generation (SHG) [25,26,61,62], a shift of the resonance frequency [20–23,63,64], and nonlinear mixing [65]. Numerous researchers have been explored a variety of nonlinear techniques and have put their efforts to characterize damage evolution in cement-based materials that originates from its complex microstructural characteristics at multiple length scale from cm to *n*m.

3.2.1 Second Harmonic Generation

Second harmonic generation technique is first reported by Breazeale et al.[66], and continuously studied by Cantrell et al. [25,61,67], Nazarov et al. [26], Shui et al. [68], and Kim et al. [27,62]. The principle of the SHG is as follows: the interaction of the propagating fundamental harmonic wave with a frequency, ω with the existing nonlinearity sources results in the generation of the second harmonic wave with a frequency, 2ω [25,58,69]. As it propagates further, the amplitude of the generated second harmonic wave is increased [70–73]. Kim et al. [27] has theoretically demonstrated the essential characteristics of the distortions in the fundamental harmonic waves by proposing an elastoplastic contact model. Such phenomena are well quantified with the measured acoustic nonlinearity parameter, β.

Recent development has highlighted that second harmonic generation (SHG) methods using nonlinear Rayleigh surface waves have great advantages [72–75]. First, the unwanted system nonlinearity from the instrumentation can be isolated by varying the propagation distance. Second, implementing an air-coupled receiver allows a more consistent measurement of the acoustic nonlinearity parameter [76]. Most importantly, among the existing NLU techniques, SHG is a unique field applicable technique since not only it requires one side of the specimens, but also as a local measurement technique, it can evaluate damage levels at different suspected location. The setup for the SHG in Rayleigh surface wave using air-coupled received is depicted in Figure 3.3. Despite these advantages, a few experiments of nonlinear Rayleigh wave in cement-based materials have been reported probably due to several reasons: (1) the lack of understanding microscale damage evolution in concrete, (2) inadequate use of a frequency pair for excitation and detection, and thus (3) high attenuation caused by scattering from its heterogeneous microstructure.

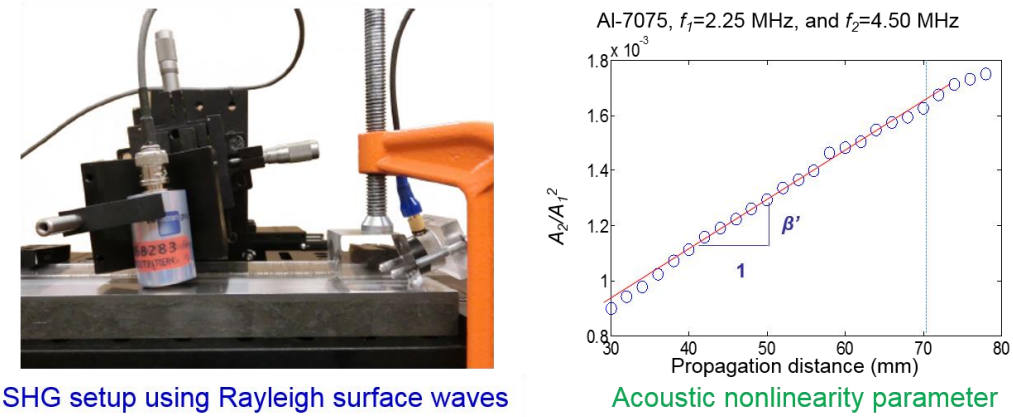

Figure 3.3. Setup for the SHG measurement with air-coupled detection [73].

3.2.2 Resonance-Based Techniques (NRUS and NIRAS)

As shown in Eq. (3.3), physical principle of these techniques is the shift in the resonance frequency with increasing level of excitation [20–22,64,77,78]. The damage state in concrete can be appeared into this nonlinear hysteresis behavior by following that the higher the damage level is, the higher the shift (left) of the resonance frequency is [20,22,23,78]. It is worthy of notice that the hysteretic parameter, a that governs a hysteretic nonlinear elastic behavior in heterogeneous materials is appeared in odd harmonics [79]. It can be therefore stated that the acoustic nonlinearity parameter, β due to the generation of even (second) harmonic is not relevant to the hysteretic parameter, a. Chen et al. [4,80] and Leśnicki et al. [5,6] have established the nonlinear impact resonance acoustic spectroscopy (NIRAS) technique based on the shift of the resonance frequency of concrete; the NIRAS method excites the fundamental resonance of the concrete prism by impact hammer and detects the vibration signal using an accelerometer. Figure 3.4 describes an example of the experimental setup for the NIRAS techniques. Payan et al. [3,29], and Bouchaala et al. [59] have successfully deployed the nonlinear resonant ultrasound spectroscopy (NRUS) technique to probe damage in cement-based materials. Compared to the conventional ultrasonic NDE techniques, the hysteresis nonlinearity parameter by NRUS and NIRAS shows great sensitivity to early-stage material damage, and thus has significant potential to be applicable to monitoring micro-scale damage evolution.

$$\frac{\Delta f}{f} = \alpha \cdot \Delta\varepsilon \tag{3.3}$$

Therefore, a considerable amount of quantitative studies based on the resonance-based NDE techniques have been extensively conducted to characterize the microscale defects in concrete such as the formation of microcracks, with much greater sensitivity than conventional linear ultrasonic methods. For instance, Chen et al. [4,80], and Leśnicki et al. [5,6] have applied the NIRAS technique to rapidly identify reactive aggregate from mortar bar and concrete prism tests. As a result, they have pointed out that aggregates type and size can cause the different rate of the shift, and assessed the influence of progressive alkali-silica reaction (ASR) damage on microstructure using the nonlinearity parameter. Bouchaala et al. [38] has applied this technique to monitor the carbonation and demonstrated that the measured material nonlinearity appears to be decreased by the progress of carbonation. In addition, the resonance-based techniques have been successfully applied to characterize freezing-thawing [2], and thermal damage [30] in concrete. The achievement by these techniques has helped establish the feasibility of nonlinear acoustic techniques for monitoring the material state of cement-based materials.

Nevertheless, these resonance-based techniques are only limited to relatively small-sized specimens, so they are impractical for the interrogation of large or complicated components. Also, those resonance methods measure the changes in global damage state of the specimen; the measured nonlinearity in this case represents an averaged value for the entire specimen. Therefore, evaluation of damage state by any locally initiated damage mechanism in concrete e.g., drying shrinkage, carbonation, and sulfate attack (from the surface) can be substantially underestimated. Note that only surface wave-based nonlinear techniques can be applicable to characterize those damage mechanisms. Additionally, these techniques are not suitable to specimens, have the complex geometry.

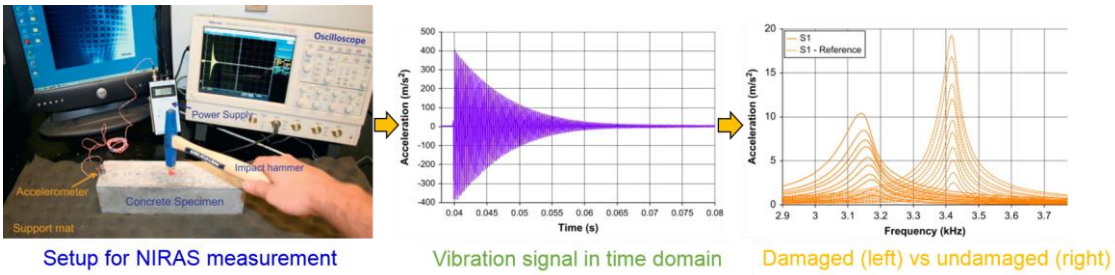

Figure 3.4. Procedure of the NIRAS measurement [5,6].

3.2.3 Coda Wave Interferometry

Coda wave interferometry (CWI) refers to the relationship between the velocity change in conjunction with the increasing stress and the strain gradient [81]. Since this relationship can be constituted by the quadratic nonlinearity parameter in nonlinear stress-strain equation, the stress-dependent velocity changes can yield the acoustic nonlinearity parameter, β. Larose et al. [82], and Payan et al. [1] have carried out the CWI measurements using concrete specimens and successfully extracted the nonlinearity parameters. An example of material characterization is reported by Schurr et al. [56]. As shown in Figure. 3.5, they have considered much longer wave path compared to the direct path, thereby increasing the sensitivity to microscale damage in concrete, and thus demonstrated that the nonlinearity parameter is monotonically increased by thermal shock and cyclic loading.

Recent research [83] has also achieved to simplify the CWI technique (called TS method) based on an assumption that the velocity change is identical to the time shift, and applied the TS method to monitor ASR damage in large-scale concrete structures. Nevertheless, progress of the CWI technique has been restricted due to several reasons. First, instrumentation of the CWI technique is not simple, compared to other nonlinear

techniques – that is, impact loading is mostly required in order to obtain the stress and strain gradient. Moreover, the fact that the impact loading is necessary means that this method is not capable of monitoring the large-scale or in-service concrete structures.

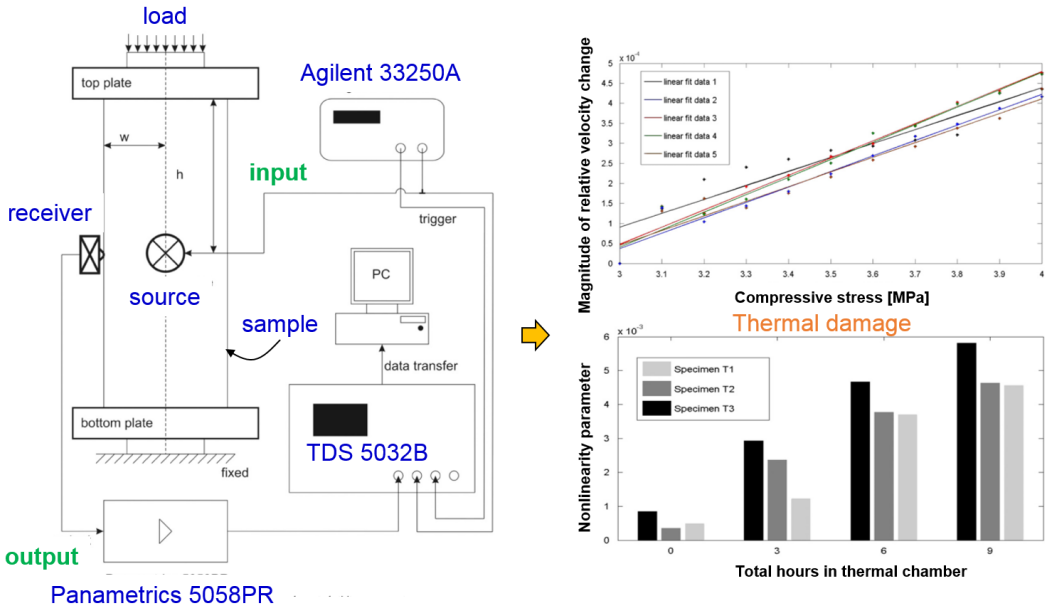

Figure 3.5. Setup for the CWI measurement: effect of thermal shock [56].

3.2.4 Other Nonlinear NDE Techniques

Scaling Subtraction Method (SSM): Unlike the analysis in frequency domain, this method uses the time domain signal to obtain the nonlinearity parameter – this technique is advantageous to subtract the instrumentation nonlinearity and has been applied to characterize the load-induced damage in concrete [28,28,30].

Dynamic Acoustoelastic Testing (DAET): DAET technique monitors the change in elastic modulus while the specimen undergoes dynamic loading. Application of this technique to cement-based material has been recently reported by [60,84].

Wave Mixing Technique: The concept of this technique is that two ultrasonic waves having different frequency (ω_1, ω_2) interact and generate new ultrasonic waves of frequency ($\omega_1 - \omega_2$). The component of three different waves is distinguished in the frequency spectrum, and therefore nonlinearity parameter can be obtained. Application to characterize ASR damage is achieved by [85].

3.3 Review of Concrete Performance

The heterogeneity of concrete, as a porous material, has direct connection with the nonlinear ultrasound − that is, the nonlinear ultrasonic waves is capable of monitoring the microcracking development in concrete. Since the microcrack is an origin of the damage evolution in concrete, the acoustic nonlinearity parameter, β can be directly used as a "stethoscope" that allows us to read the current damage state in concrete.

3.3.1 Drying Shrinkage & Shrinkage-Reducing Admixture

Of particular interest for the evaluation of concrete structural health is the characterization of the time-dependent evolution of microstructure and environmental interactions [86–90]. In an environment which is dry relative to concrete, water evaporates to the air. As pores empty, tensile stresses are generated, and when the tensile capacity – which can be limited in cement-based materials, and particularly so at earlier ages – is exceeded, cracking develops. It is therefore expected that microcracks are significantly developed by drying shrinkage, and because the drying front develops from an exposed

surface, much of the source of microstructural nonlinearity will be concentrated near these surfaces in drying environments.

There have been long-standing efforts in assessing the microstructural development by drying shrinkage [86,91–94]. For instance, it has been postulated that surface experiences drying shrinkage much faster than the inner bulk area [95–97] that leads to the logarithmically increasing of shrinkage with time. A number of the experimental evidences demonstrated the effects of pore size [98], water-to-cement ratio [92,99], the environmental condition [100,101], and the aggregate restraining [89,102–104] on the rate of drying shrinkage. Later, some NDE-based approaches have been applied to characterize drying shrinkage. It has been well reported that acoustic emission (AE) technique [105] can catch the crack development in cement and mortar. Some ultrasonic pulse velocity (UPV) measurements have been also reported by [106].

Recently, a number of researchers [87,107–110] have introduced shrinkage-reducing admixture (SRA) and demonstrated that SRA has great effect on reducing the surface tension of the concrete pore solution, and the capillary stresses that induce cracking in paste. This decrease in both surface tension and stress eventually results in mitigating the autogenous and drying shrinkage, so early-age cracking can potentially be mitigated by appropriate dosages of SRA.

3.3.2 Carbonation

Exposure of in-service concrete infrastructure to the natural environment causes continuous changes in microstructure and composition, often starting from their surfaces. It is well known that carbonation is a common occurrence in cement-based materials. During carbonation, calcium hydroxide ($Ca(OH)_2$) contained in hydrated cement paste reacts with carbon dioxide, present in air or water, forming calcium carbonate ($CaCO_3$) and water (H_2O). The formation of carbonation is explained by the following equations:

$$CO_2 + Ca(OH)_2 \rightarrow CaCO_3 + H_2O \tag{2.48}$$

$$Ca^{2+} + CO_3^{2-} \rightarrow CaCO_3. \tag{2.49}$$

Importantly, the formation of $CaCO_3$ is irreversible, meaning that the $CaCO_3$ is unable to decompose to the Ca^{2+} and CO_3^{2-} once it precipitates.

The gradual process of carbonation alters the surface properties and decreases the pH value of the pore solution from typical values (12-13.0) to a 9 or less [111–113] due to the virtually insolubility of the carbonation product ($CaCO_3$) relative to the slightly soluble reactant [114]. More recently, processes to intentionally carbonate ordinary portland cement concrete and concrete produced with alternative cements are of growing interest as potential options for carbon sequestration [115,116].

However, over time in reinforced concrete, as the relatively low-pH “carbonation front” reaches greater depths from the surface, depassivation of the reinforcement steel can occur and corrosion can initiate. Corrosion of reinforcement is considered to be a serious

durability concern which ultimately limits the service life of reinforced concrete structures [117–119].

Hence, for a number of reasons, it is critical to detect carbonation in concrete. Methods to do so non-destructively are preferred such that elements or structures can be monitored over time as carbonation progresses. Also, on large-scale structures, destructive testing is either not permitted or cost-prohibitive and is not capable of providing a representative statistical sampling of the structural condition. Automated monitoring using embarked nondestructive devices is the most promising approach to a full-extent degradation mapping of structures like atmospheric cooling towers or nuclear containment buildings.

Various evaluation methods have been used to detect carbonation in concrete. The use of an indicator solution, like phenolphthalein, is the most well-known method to measure the depth of the carbonation, and this must be done on a freshly fractured surface [3, 10]. Also, analytical methods like thermogravimetric analysis (TGA) [111–113,120–122] and quantitative X-ray diffraction (QXRD) analysis [120,123] can be used to assess the relative amount of $Ca(OH)_2$ and $CaCO_3$ at various depths in a sample obtained from a structure. Most recently, indentation methods, (i.e., micro [124] and nanoindentation [125]) have been used to characterize carbonation depths and the process of carbonation. Accordingly, it is well-established that carbonation significantly influences density, strength, elasticity moduli, pore size, and permeability among other properties of cement-based materials [126–128]. Research has also been directed toward increasing the durability against carbonation, which has been shown to be controlled by the use of SCMs [129–133], water-to-cement ratio (w/c) [120,134,135], curing conditions and time

[136,137], aggregate type [120], the different alkali contents [134], and environmental factors [133].

3.3.3 Alkali-Silica Reaction (ASR)

Alkali-silica reaction (ASR) is one of the most deleterious damage mechanism in concrete that can induce microcrack development, visible macrocracks, and thus serious durability problems [86,138,139]. It is reported that a series of sequential chemical reactions result in the ASR damage process: (1) dissolution of silica by hydroxyl attack [140]; (2) ASR gel formation [141]; (3) swelling of the ASR gels [142]; and (4) stress, expansion, and cracking [86,143–145]. To characterize these phenomena, multiple evaluation methods have been introduced. For instance, Kurtis et al. [140] investigated the role of ASR gel in expansion based on the x-ray microscopy technique. Haha et al. [146] implemented scanning electron microscope (SEM) to quantify the reactivity of aggregates. Progress in studying the effects of lithium-based compounds on ASR reactivity has been also reported by [147,148]. The observations from these studies have demonstrated that the ASR gel and its swelling are closely associated with distress, loss of strength, and thus decreasing elastic modulus in concrete. For the expansion measurements, it is reported that there are several discrepancies in standardized test methods [149,150] thus, some efforts have been made by [151,152] to enhance their reliability. More recently, Rajabipour et al. [40] reported an integrated summary on the ASR mechanisms, the accompanying aggregate properties, and the mitigation methods. Vayghan et al. [153] carried out a rheological investigation of the properties of ASR gel and highlighted that the yield stress

of the ASR gel and swelling pressure are highly dependent on the gel's chemical composition, i.e., the amount of calcium and sodium contents. Research has also been directed toward developing the modelling of ASR by Multon et al. [154,155].

3.3.4 Creep & Cyclic Loading

In practice, great portion of concrete structures experiences a continuous degradation due to several factors associated with applied stress, e.g., creep, periodic load and pressurization, and tendon relaxation. It is therefore vital to understand the phenomenon of microstructural development by various types of the compressive loads leading to crack initiation and growth. It is well known that sustained and cyclic loading are the most common damage types that can describe these phenomena in concrete.

Many researchers have put extensive efforts to characterize the effect of creep and cyclic loads on the material properties in concrete [86,91–94]. Extensive experimental and numerical evidences demonstrated the microcrack formation, growth, and propagation in concrete subjected to the creep and cyclic loading [16,156–159]. Among the literature, it should be emphasized that Shah et al. [16] has revealed that concrete could be either strengthened [160] or weakened, depending on the applied loading level and time. Another important observation is that Carrasquillo et al. tracked the crack density by increasing loading level in furthering the understanding of the progressive microcracking inside of the specimen [161].

CHAPTER 4. SECOND HARMONIC GENERATION (SHG) FOR CONCRETE NDE

4.1 Overview

The objective of this chapter is to demonstrate the feasibility of the SHG technique using Rayleigh surface waves for monitoring early-stage material damage in concrete. The high attenuation of ultrasonic waves in cement-based materials has made the practical measurement of SHG difficult to implement in this material. There are also severe repeatability issues with the contact detection of ultrasound in concrete caused by its inconsistent surface roughness and coupling conditions. In order to solve these issues, the SHG setup using non-contact, air-coupled detection technique is designed in the frequency range 40 to 100kHz, and the feasibility of the proposed setup is validated through the measure of the nonlinear Rayleigh surface waves and the acoustic nonlinearity parameter, β. To demonstrate the effectiveness of this air-coupled detection of the SHG in Rayleigh waves in concrete, the effect of shrinkage-reducing admixture (SRA), as it influences microcrack formation in these materials, is considered as an example of evaluation.

4.2 Theory of SHG in Rayleigh Surface Waves

The derivation of the nonlinear wave equation is followed by reviewing the reference [61,162].

Nonlinear stress-strain relationship: The derivation of nonlinear stress-strain relationship in a solid medium normally starts with a consideration of the strain energy W per unit mass as follows.

$$\rho_0 W = \frac{1}{2!} C_{ijkl} E_{ij} E_{kl} + \frac{1}{3!} C_{ijklmn} E_{ij} E_{kl} E_{kl} + \ldots \tag{4.1}$$

where, C_{iljk} and C_{ijklmn} represent the fourth- and sixth-order elastic constants. Note that the Eq. (4.1) describes an expansion for small strain. Thus the infinitesimal (or Green) strain tensor in terms of a Lagrangian coordinates should be considered as

$$\begin{gathered} E = \frac{1}{2}(\mathrm{F}^{\mathrm{T}} \cdot F - I) \\ or \\ E = \frac{1}{2}\left(\frac{\partial \mathrm{u_i}}{\partial \mathrm{x_j}} + \frac{\partial \mathrm{u_j}}{\partial \mathrm{x_i}} + \frac{\partial \mathrm{u_k}}{\partial \mathrm{x_i}} \frac{\partial \mathrm{u_k}}{\partial \mathrm{xj}}\right) \end{gathered} \tag{4.2}$$

where I is the second-order identity tensor, and F the second-order deformation gradient tensor.

$$\begin{gathered} F_{ij} = x^*_{i,j} \\ or \\ F_{ij} = \frac{\partial \mathrm{x_i^*}}{\partial \mathrm{x_j}} \end{gathered} \tag{4.3}$$

which shows a deformation mapping where x^* relates to the current configuration (Eulerian coordinate) and the x to the reference configuration (Lagrangian coordinate). Figure 4.1 describes the kinematics of deformation in Euclidian space.

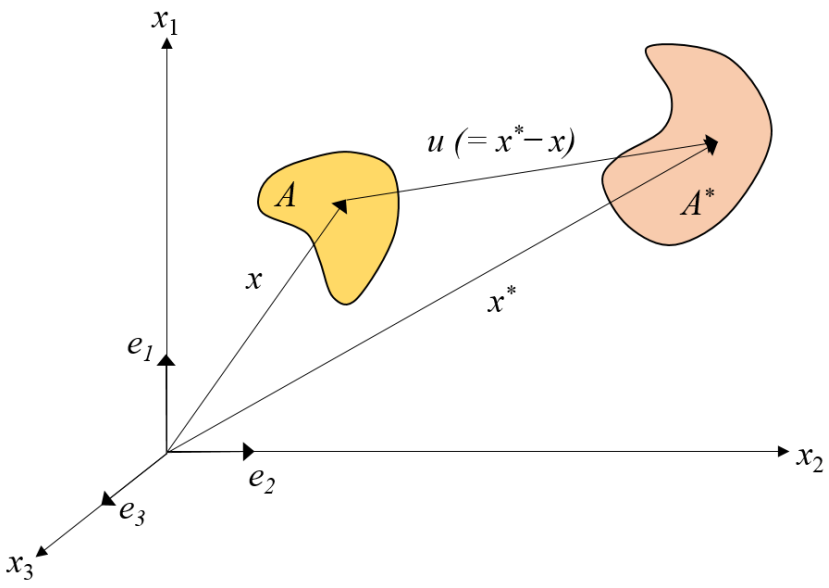

Figure 4.1. Material and spatial coordinates in Euclidian space.

In Figure 4.1, A represents undeformed body in Lagrangian coordinate while A^* indicates the deformed body with Eulerian coordinate, and the displacement u at a given time, t becomes the difference between x^* and x. Note that e_i indicates the unit normal vector. Using the first Piola-Kirchhoff stress tensor as shown in Eq. (4.4), the nonlinear stress-strain relationship can be rewritten as

$$\sigma^{PK} = \frac{\rho_0}{\rho}\sigma \cdot F^{-T} \tag{4.4}$$

$$\sigma_{ij}^{PK} = C_{ijkl}\frac{\partial u_k}{\partial x_l} + \frac{1}{2}M_{ijklmn}\frac{\partial u_k}{\partial x_l}\frac{\partial u_m}{\partial x_n} + \ldots \tag{4.5}$$

where,

$$M_{ijklmn} = C_{ijklmn} + C_{ijnln}\delta_{km} + C_{jnkl}\delta_{im} + C_{jlmn}\delta_{ik}\,. \tag{4.6}$$

Figure 4.2 explains the difference between Eq. (2.10) and Eq. (4.5).

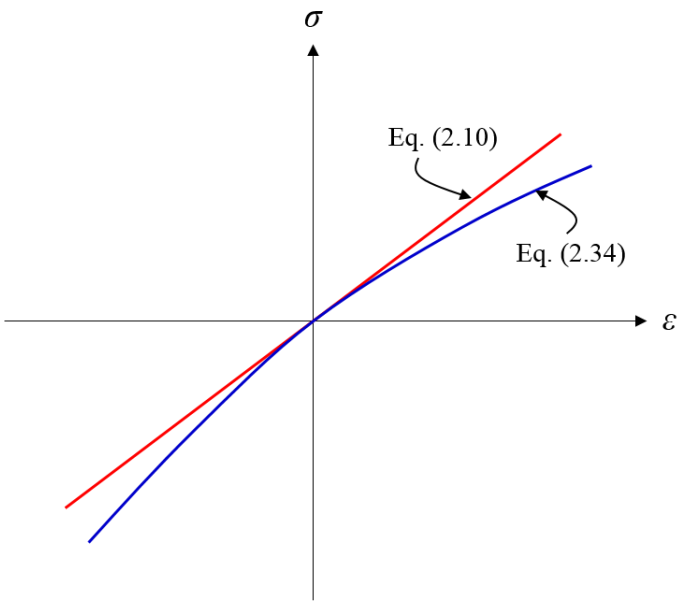

Figure 4.2 Linear vs nonlinear constitutive relationship.

Theory of second harmonic generation (SHG): Analogously, considering the equation of motion in Lagrangian coordinate shown in Eq. (4.7) with Eq. (4.6) leads to the nonlinear wave equation.

$$\rho_0 \frac{\partial u_i}{\partial t^2} = \frac{\partial \sigma^{PK}}{\partial x_j} \tag{4.7}$$

$$\rho_0 \frac{\partial^2 u_i}{\partial t^2} = \frac{\partial^2 u_k}{\partial x_j \partial x_l} \left(Ci_{jkl} + \frac{1}{2} M_{ijklmn} \frac{\partial u_m}{\partial x_n} + \ldots \right) \tag{4.8}$$

For purely longitudinal wave, Eq. (4.8) can be simplified to

$$\frac{\partial^2 u_1}{\partial t^2} = C_L \frac{\partial^2 u_1}{\partial x_1^2} \left(1 - \beta \frac{\partial u_1}{\partial x} \right) \tag{4.9}$$

where, β is the quadratic material nonlinearity parameter, C_{111} the third-order elastic constant in Voigt notation, and C_L the longitudinal wave velocity.

$$\beta = -\left(\frac{3}{2} + \frac{C_{111}}{2\rho_0 C_L^2} \right) \tag{4.10}$$

It is important to note that the distortion of the nonlinear wave is accompanied by the higher harmonic waves depending on the β, and this physical phenomenon is characterized by observing the amplitudes of both fundamental and second harmonic waves. Consider the fundamental longitudinal harmonic wave with amplitude, A and the frequency, ω.

$$u(x,t) = A \sin(k_L x - \omega t) \tag{4.11}$$

A displacement perturbation of this form can be solved with Eqns. (4.6) and (4.10).

$$\begin{aligned} u(x,t) &= A_1 \sin(k_L x - \omega t) + A_2 \sin(2k_L x - 2\omega t) + \ldots \\ &= A_1 \sin(k_L x - \omega t) + k_L^2 A_1^2 x \sin(2k_L x - 2\omega t) + \ldots \end{aligned} \tag{4.12}$$

where, A_1 and A_2 indicate the fundamental and second harmonic amplitudes.

Finally, Eqns. (4.10) to (4.12) provides the form of the quadratic nonlinearity parameter such that

$$\beta = \frac{A_2}{A_1^2}\frac{8C_L^2}{\omega^2 x_1}. \tag{4.13}$$

As clearly shown in Eq. (4.13), the quadratic material nonlinearity parameter can be acoustically obtained by measuring both A_1 and A_2 with the constant C_L over the propagation distance [163]. This enables us to denote the β as quadratic (or absolute) acoustic nonlinearity parameter. Figure 4.3 illustrates the principle of the second harmonic generation (SHG) observed in nonlinear ultrasonic measurement [62].

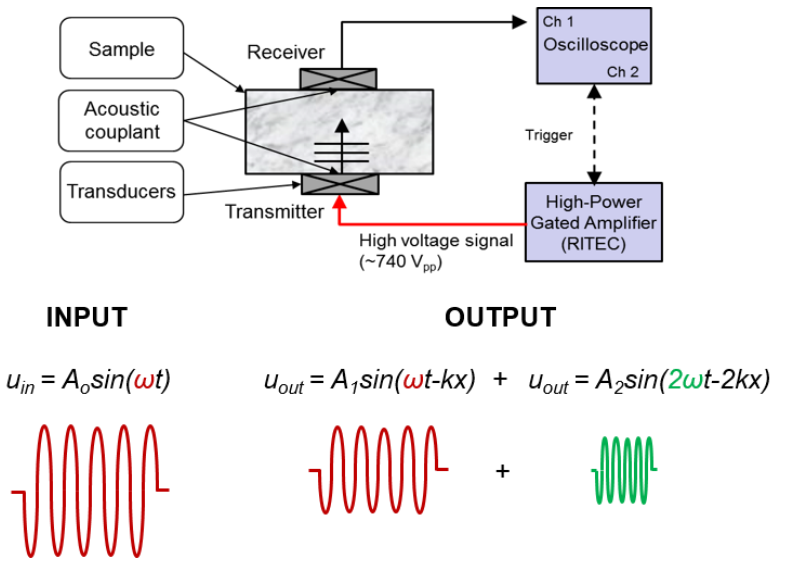

Figure 4.3. Schematic of the SHG measurement with longitudinal wave.

The SHG in Rayleigh surface waves: Consider a plain Rayleigh surface wave propagating along the x axis in an isotropic, macroscopically homogeneous, and elastic

half space where z axis refers to the depth of the material. First, the displacements in *x* and *z* directions can be written in Eq. (4.14) and both displacement components indicate the shear (*x* direction) and longitudinal (*z* direction) wave contributions.

$$u_x(\omega) = A_1\left(e^{b_1 z} - \frac{2b_1 b_2}{k_R^2 + b_2^2} e^{b_2 z} \right) e^{i\{k_R(x - c_R t)\}} \tag{4.14a}$$

$$u_z(\omega) = iA_1 \frac{b_1}{k_R}\left(e^{b_1 z} - \frac{2k_R^2}{k_R^2 + b_2^2} e^{b_2 z} \right) e^{i\{k_R(x - c_R t)\}} \tag{4.14b}$$

where, C_R is the speed of Rayleigh surface waves, ω is the fundamental angular frequency, $b_1 = \sqrt{{k_R}^2 - {k_l}^2}$ and $b_2 = \sqrt{{k_R}^2 - {k_s}^2}$ with k_l, k_s, and k_R are the wave numbers of the longitudinal wave, the shear wave, and the Rayleigh waves.

In an isotropic material that has weak quadratic nonlinearity, the displacements of the second harmonic Rayleigh waves in the far-field can be expressed as [74,76]:

$$u_x(2\omega) \approx A_2\left(e^{2b_1 z} - \frac{2b_1 b_2}{k_R^2 + b_2^2} e^{2b_2 z} \right) e^{i\{2k_R(x - c_R t)\}} \tag{4.15a}$$

$$u_z(2\omega) \approx iA_2 \frac{b_1}{k_R}\left(e^{2b_1 z} - \frac{2k_R^2}{k_R^2 + b_2^2} e^{2b_2 z} \right) e^{i\{2k_R(x - c_R t)\}} \tag{4.15b}$$

Acoustic nonlinearity parameter, β: Hermann et al. [74] showed that the acoustic nonlinearity parameter can be expressed by the out-of-plain displacement components of the propagating Rayleigh waves at the surface (z = 0) as shown in Eq. (4.16).

$$\beta = \frac{u_z(2\omega)\big|_{z=0}}{u_z{}^2(\omega)\big|_{z=0}} \frac{8b_i i}{k_l{}^2 k_R x}\left(1 - \frac{2k_R^2}{k_R^2 + b_2^2}\right) \tag{4.16}$$

where, β is quadratic (or absolute) acoustic nonlinearity parameter. The relationship between the fundamental and second harmonic components and the acoustic nonlinearity parameter can be written as

$$\frac{A_2}{A_1^2} \propto \frac{\beta \omega^2 x}{C_R{}^2} \tag{4.17}$$

Since the wave speed of the Rayleigh surface wave is independent of the frequency of the wave, A_2 / A^2_1 is directly proportional to β at fixed distance as shown in Eq. (4.18). It is well established that the relationship between A_2 / A^2_1 and the propagation distance is a good approximation for calculating the acoustic nonlinearity parameter for a short propagation distances. This research denotes $A_2 / A^2_1 x$ as the acoustic nonlinearity parameter, β as shown in Eq. (4.19). Figure 4.4 describes the SHG setup for the Rayleigh surface waves.

$$\beta \propto \frac{A_2}{A_1^{\,2} x} \tag{4.18}$$

$$\beta \equiv \frac{A_2}{A_1^{\,2} x} \tag{4.19}$$

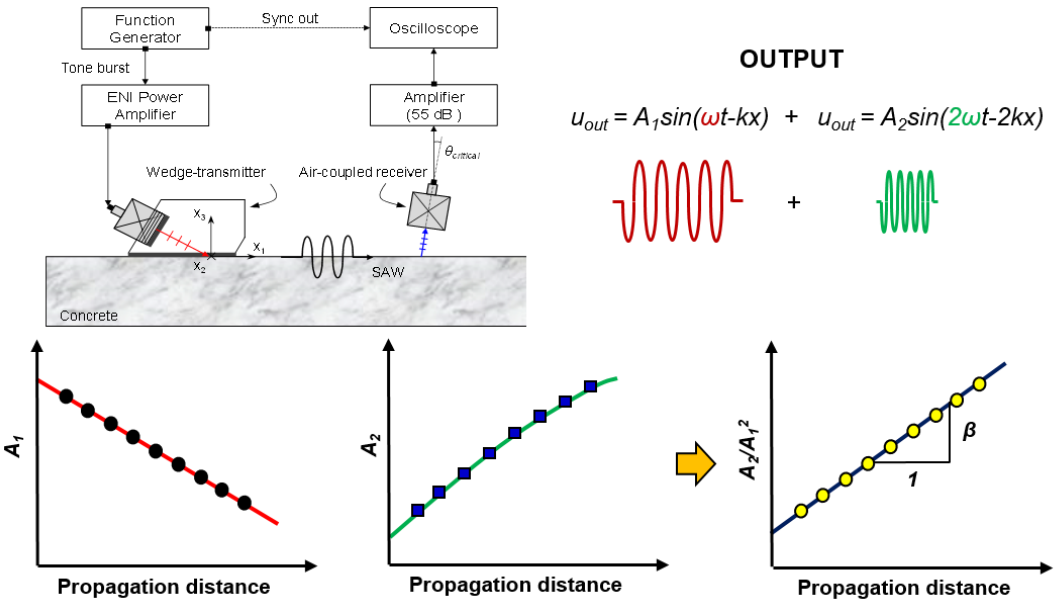

Figure 4.4. Schematic of the SHG measurement with Rayleigh surface wave.

Note that the received out-of-plane components of the second harmonic wave is due to the distortion of longitudinal waves since the acoustic nonlinearity parameter is rarely existed for shear waves. Previous research has demonstrated that the acoustic nonlinearity parameter is experimentally obtained not only in a homogeneous material, but also in a nickel-base superalloy, concrete, and sandstone [27,28,31,32]. Importantly, the significance of the SHG measurements is attributed to the fact that the wavelength for both fundamental (ω) and second harmonic (2ω) frequencies can be determined based upon the target material or the defect size, meaning that the SHG setup enable the multi-scale

material characterization. However, once the ratio of wavelength to the target size is optimized, then the wavelength would become fixed during the entire monitoring period. Most importantly, during the accumulation of the material nonlinearity into the second (even) harmonic waves, a hysteretic nonlinear elastic behavior should be ignored because the hysteretic nonlinearity parameter, a is only observed in odd harmonics [79]. Therefore, it is worthwhile to note that understanding of early-stage microcracking development in cement-based materials should be followed closely with the SHG measurements.

4.3 Sample Preparation

Two sets of specimens are considered, one pair of concrete specimens and one pair of mortar specimens. For each pair, one specimen is prepared with SRA (BASF SRA 20) and a second identical specimen without SRA. To focus on changes in drying shrinkage due to SRA, a water-to-cement ratio (w/c) of 0.60 is used [87,107]. SRA is dosed at 3.4% of the total mass of water in concrete and 3% in mortar. The amount of the added SRA shown in Table 1 provides evidence that different microcracks have formed by the SRA in each pair. Table 1 shows further details on the mixture proportions, which are based on ACI 211.1[165]. Type I Portland cement (ASTM C 150) is used in the mix designs [166]. For the concrete specimens, pea gravel with a MSA (maximum size of aggregate) of approximately 12.7 mm is chosen for the coarse aggregate and a natural sand with a fineness modulus of 3.04 is used as fine aggregate. To homogenize the chemical interaction between the fine aggregate and the cement, the fine aggregate-to-cement ratio is fixed at 2.2 for all specimens while keeping the specimen volume constant. As a result, larger

quantities of the fine aggregate, water, and cement are used in the mortar samples than in the concrete samples.

The freshly mixed concrete and mortar specimens are placed into molds (21.5 × 56.5 × 17.5 cm), compacted by a rod, and finished with a trowel. They are then covered by polyethylene sheeting and cured at the ambient temperature for 14 days and demolded. The demolded specimens are transferred into an environmental chamber (23˚C and 95% relative humidity) until 28 days of age. Finally, all specimens are placed in a drying chamber (23˚C and 52% relative humidity) for 14 days to bring them to an equilibrium moisture content.

Table 4.1 Mixture design of concrete and mortar mixtures, kg/m^3 (lb/yd^3).

	Concrete	Concrete with SRA	Mortar	Mortar with SRA
Water	217 (365)	209 (352)	373 (628)	365 (615)
Cement (Type1)	361 (608)	361 (608)	621 (1046)	621 (1046)
Water-to-cement ratio (w/c)	0.6	0.6	0.6	0.6
Coarse Aggregate	872 (1470)	872 (1470)	-	-
Fine Aggregate	784 (1322)	784 (1322)	1397 (2354)	1397 (2354)
SRA	-	8 (13)	-	8 (13)

4.4 Development of SHG Measurement Setup

4.4.1 Experimental Setup

The physical principle of the SHG method is that a propagating ultrasonic wave with a fundamental harmonic frequency, ω interacts with the internal microstructure (including the damage state) and some energy of the fundamental harmonic wave is converted to generate a second harmonic wave with the frequency 2ω. The amplitude of

the second harmonic wave is directly dependent on the sources of the material nonlinearity such as microcracks [27]; the SHG method using Rayleigh surface waves is capable of quantifying microcracks in concrete. The relationship between this material nonlinearity and a propagating ultrasonic wave is shown in Eq. (4.19) [37,58].

A schematic of the designed SHG setup using Rayleigh surface waves is described in Fig. 4.5. A function generator (AGILENT 33250A) generates a tone-burst signal of 16 cycles at 45 kHz excitation frequency which has a peak-to-peak voltage of 400 mV and occurs over a burst period of 200 ms. The signal is then amplified by a power amplifier (ENI Power Amplifier) as much as 50 dB and fed to the transmitting transducer. The entire measurement is synchronized by a trigger signal from the function generator. Note that the effective frequency range of the SHG setup for concrete is within 40 to 120 kHz. A 50 mm diameter, narrow-band, piezoelectric transducer with a center frequency of approximately 50 kHz (Ultran GRD 50) is employed as a transmitter and is tightly coupled to the Teflon wedge with vacuum grease. It is confirmed that the tone-burst signal at 45 kHz frequency has a better steady-state shape and higher amplitude than 50 kHz frequency. The wedge is carefully designed in such a way that the detected Rayleigh surface wave amplitude is maximized and the insertion loss is minimized. The longitudinal wave speed in the Teflon (1450 m/s) and the Rayleigh surface wave speed in the concrete specimen (2450 m/s) are measured and then the wedge angle is determined to be 36.3 degrees according to Snell's law. The wedge transducer is attached to the prepared specimens using the same vacuum grease. For the detection of propagating Rayleigh waves, a non-contact, air-coupled transducer with a center frequency of approximately 100 kHz (Ultran GRD 100) is employed. The air-coupled transducer is then tilted by 8 degrees, which is the

Rayleigh wave critical angle (θ) at the air-concrete interface, and it should be noted that critical angle is slightly adjusted in the range of 8 to 10 degrees based on the phase velocity for each specimen. The lift-off distance between the receiver and the surface is fixed at 3.3 cm. At this distance, one can avoid the multiple reflection of the leaky Rayleigh wave signal between the concrete surface and transducer surface and also minimize the attenuation and diffraction effects in the air. Figure 4.6 shows the experimental setup for the SHG in Rayleigh surface waves. To ensure a high SNR (signal-to-noise ratio), the received signal is amplified by 58 dB using a broadband preamplifier (Digital Wave Inc.) and then averaged 256 times with an oscilloscope (Tektronix TDS 5034B Digital). The calculated signal-to-noise ratio (SNR) of the received time-domain signal is about 50 dB.

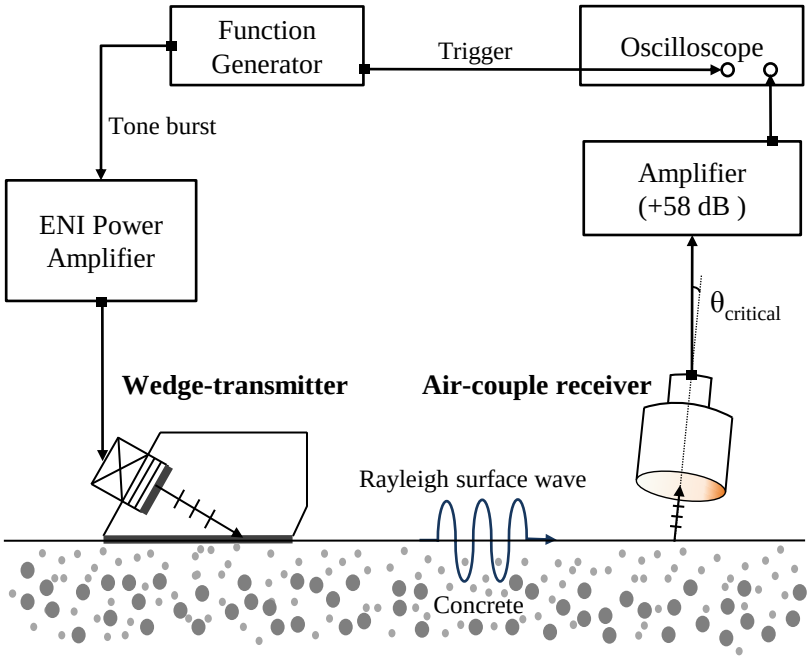

Figure 4.5. Schematic of the designed SHG measurement setup with Rayleigh surface waves.

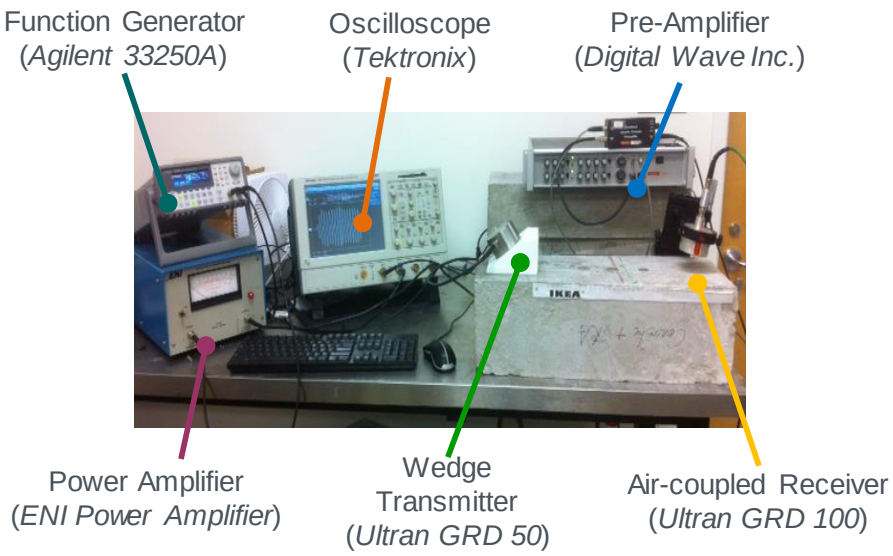

Figure 4.6. The SHG measurement setup for a non-contact detection of Rayleigh surface waves using air-coupled receiver.

The averaged signal is recorded and transferred to a computer for post-processing. In the post-processing, a Hann widow and fast Fourier Transform (FFT) are applied to the steady state part (8 cycles) of the averaged time domain signal to calculate the frequency spectrum. The air-coupled transducer is then shifted to the next measurement location and again acquires the time domain signal. In this way, the fundamental (A_1) and second harmonic (A_2) amplitudes are obtained at multiple locations along the propagation path (the acoustic axis). In this measurement, the propagation distance is approximately 3 cm; this measurement range is limited by the selected frequency and the specimen size. Figure. 4.7 shows that not only A_1, but also A_2 are clearly appeared in the obtained frequency spectrum. Moreover, as shown in Fig. 4.8 (a), the measured A_2 tend to be monotonically increasing with the increasing propagation distance while A_1 keeps decreasing. As described earlier,

both trends are in good agreement with the theory of second harmonic generation. Therefore, the ratio of A_2 to A_1^2 shows in a linear fashion with the propagation distance – the coefficient of determination (R^2) for the linear fit is higher than 99%. Note that the acoustic nonlinearity parameter, β is the slope of the linear fit for the repeated SHG measurements. Therefore, it is clearly demonstrated that the proposed SHG setup within the 40 to 120 kHz frequency range is capable of measuring the acoustic nonlinearity parameter, β in concrete.

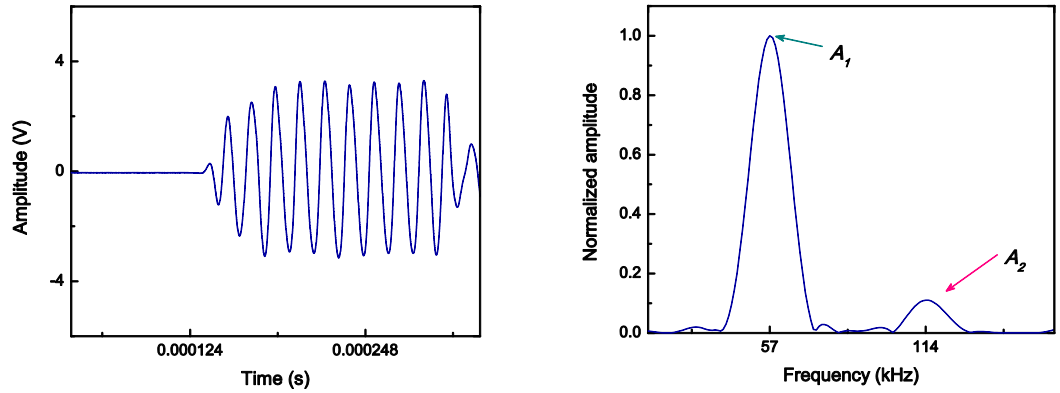

(a) Received time domain signal (b) Frequency spectrum by FFT

Figure 4.7. Results from SHG measurements.

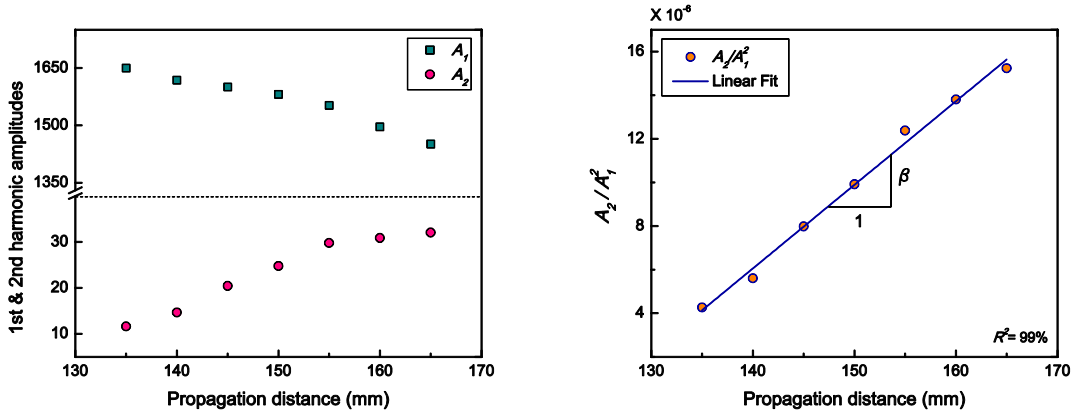

(a) Trend of A_1 and A_2 with propagation distance (b) A_2/A_1^2 versus propagation distance

Figure 4.8. Results from SHG measurements.

4.4.2 Robustness of Non-Contact Detection Technique

Since this research implements the air-coupled detection method for the first time in the nonlinear Rayleigh wave measurement of cement-based materials, the repeatability of the measurements needs to be examined. To evaluate this repeatability, this chapter compares the trends of the acoustic nonlinearity parameters from the setup using a non-contact, air-coupled receiver with a second identical system, except that it uses a contact wedge receiver. In these experiments, the transmitting wedge is fixed and the receiver is removed and re-attached. The measurement is repeated 5 times for the same propagation distance. Figure 4.9 (a) shows that the measured β, the slope of the line on the ratio (A_2/A_1^2) versus the propagation distance, calculated from the wedge-receiver are neither consistent nor repeatable since the propagated Rayleigh surface wave becomes distorted by inconsistencies between the wedge and the randomness of the rough concrete surface. In contrast, the measured β from the air-coupled receiver is more linear showing that linear fits have R^2 correlation coefficients of 0.98 or higher and the multiple nonlinearity parameters are close to one another as shown in Fig. 4.9 (b). Note that the received signal from the air-coupled method, unlike the signal from the wedge receiver, is amplified by the preamplifier; the amplitude of the ratio measured from the air-coupled receiver shown in Fig. 4.9 (b) is therefore much higher than that from the wedge receiver. These experimental results demonstrate that the air-coupled detection method provides a consistent, rapid, and repeatable measurement of the nonlinearity, enabling the accurate comparison of the damage state in cement-based materials.

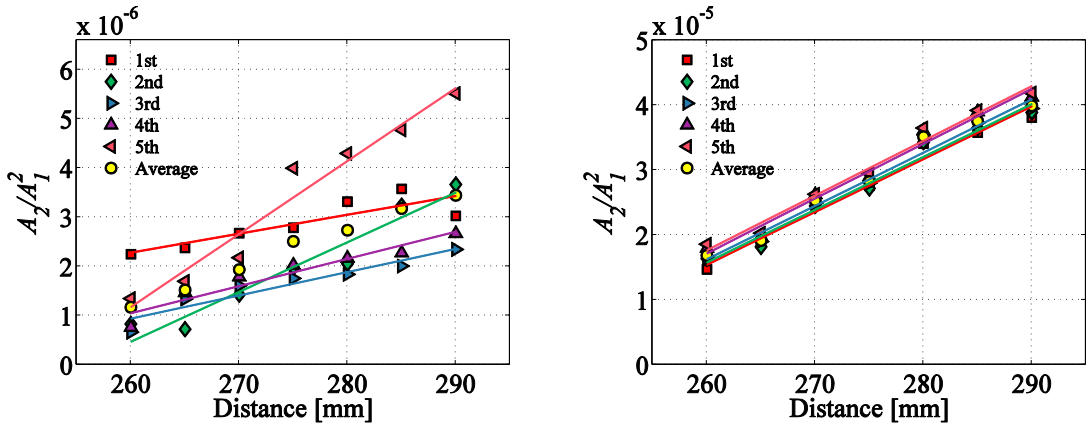

(a) The calculated acoustic nonlinearity parameter from the wedge receiver

(b) The calculated acoustic nonlinearity parameter from the air-coupled receiver

Figure 4.9. The accuracy and repeatability of air-coupled (AC) detection method.

4.5 Application to Microcracking Detection

4.5.1 Influence of Shrinkage-Reducing Admixture (SRA) on Microstructure

As a target of evaluation, this research experimentally quantifies the effects of shrinkage reducing admixture (SRA) on reducing the microcracks induced by autogenous and drying shrinkage [107]. A number of researchers [87,107,108,167,168] have shown that SRA reduce the surface tension of the concrete pore solution, and the capillary stresses that induce cracking in paste. This decrease in both surface tension and stress reduces the autogenous and drying shrinkage, so early-age cracking can potentially be mitigated by appropriate dosages of SRA. The current study examines concrete and mortar specimens with identical compositions, the only difference being that some should contain shrinkage cracks, while the others should be relatively shrinkage crack free.SRA is considered as a

good candidate for counteracting drying shrinkage. Figure 4.10 describes the influence of SRA on mitigating drying shrinkage [169].

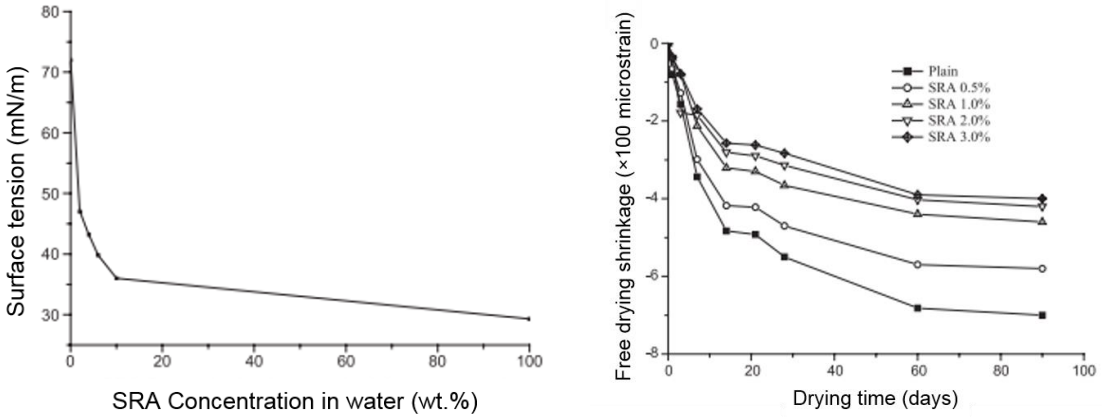

(a) Surface tension vs SRA (b) SRA dosage vs drying shrinkage

Figure 4.10. Effect of SRA concentration on reducing surface tension [169].

4.5.2 Linear Ultrasonic Measurements

To demonstrate the sensitivity of both linear and nonlinear ultrasonic parameters, Rayleigh wave velocity and attenuation coefficient are measured. The Rayleigh phase velocity is obtained by the time-of-flight (TOF) method in which the distance between two different locations of the receiver is divided by the difference in arrival times. For the accuracy, the Rayleigh wave velocity is also measured by following the procedure in [50]. Eqns. (4.20), and (3.1) show the expression for the phase velocity and the attenuation.

$$v(f) = \frac{2\pi f (z_2 - z_1)}{\arg\left(\frac{S_1}{S_2}\right)} \tag{4.20}$$

The results of wave velocity from the using the spectral ratio technique is shown in Fig. 4.11. Importantly, the experimental result supports that the concrete specimen can be treated as a weakly dispersive medium since the phase velocity for the specimen at each carbonation state is almost constant within the effective frequency range (approximately 40-100 kHz). In addition, it is confirmed that the measured velocities from the TOF method is almost identical to those from the spectral ratio method (both are approximately 2450 m/s). Figure 4.12 and 4.13 show the measured phase velocity and attenuation for the same sets of specimens. And Table 3 summarizes the measurements of the linear ultrasonic parameters.

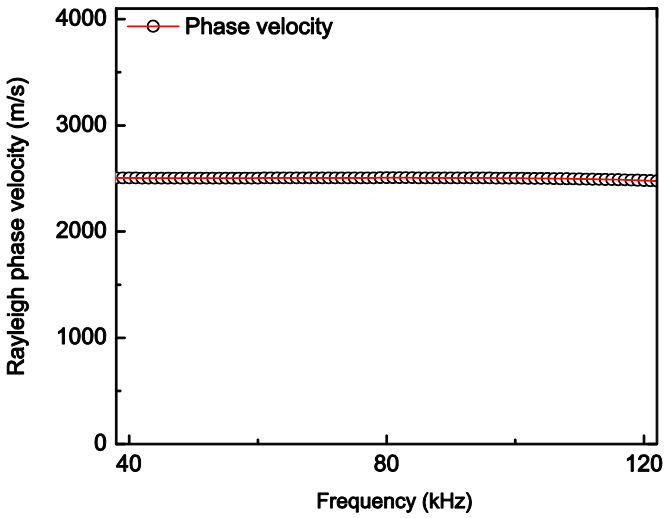

Figure 4.11. Weakly dispersive characteristics in concrete.

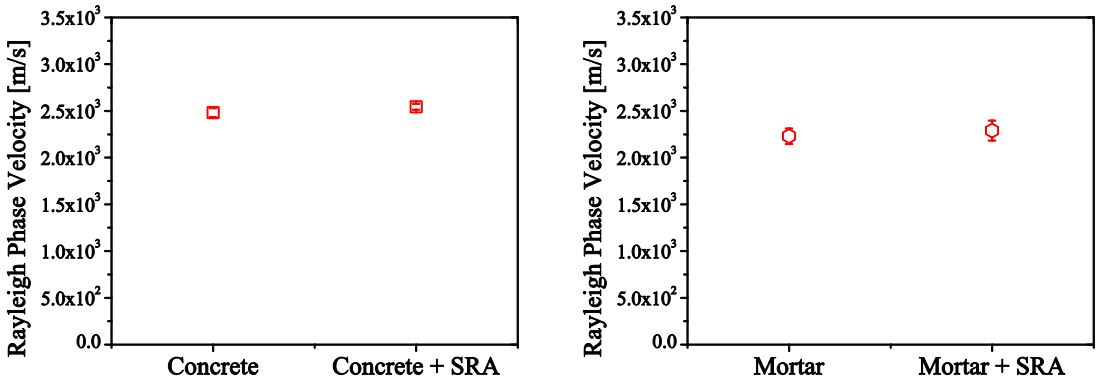

(a) The Rayleigh wave velocity (Concrete). (b) The Rayleigh wave velocity (Mortar).

Figure 4.12. Comparison of the measured phase velocity.

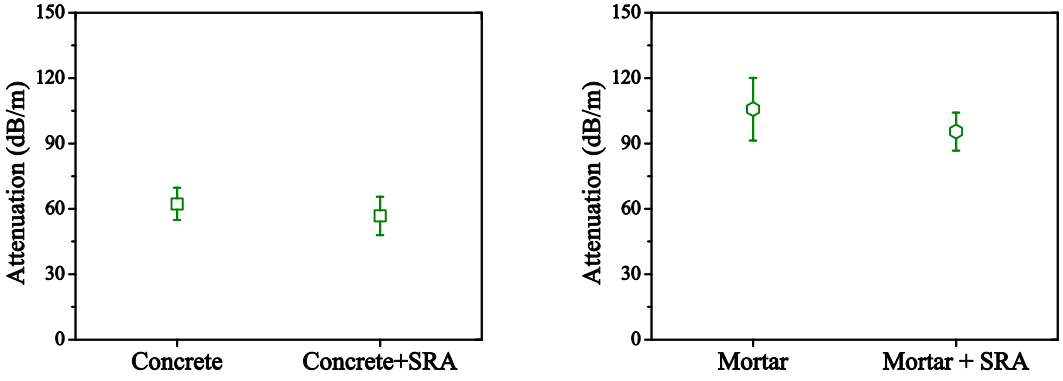

(a) The attenuation coefficient (Concrete). (b) The attenuation coefficient (Mortar).

Figure 4.13. Comparison of the measured attenuation coefficient.

Table 4.2 The measured Rayleigh wave velocities and attenuation coefficients.

	Concrete	Concrete with SRA	Mortar	Mortar with SRA
Averaged phase velocity (m/s)	2482	2543	2230	2290
Averaged attenuation (dB/m)	62	57	106	95

4.5.3 SHG Measurements

Nonlinear Rayleigh surface waves are measured in these specimens with the proposed non-contact, air-coupled detection method. The fundamental and second harmonic frequencies are 45 kHz and 90 kHz respectively. The wave length (27.2 mm) of a sinusoidal signal at 90 kHz is on the same order of magnitude with the size of the largest coarse aggregate (12.7 mm) in the concrete specimen; therefore, the effects of the scattering are not negligible [27-28]. However, the measured second harmonic amplitudes are repeatable and consistent in this multiple-scattering environment. Finally, the results are analyzed and interpreted to examine the effect of SRA in reducing microscale shrinkage cracks. It should be noted that prior to each measurement, the concrete and mortar samples were carefully examined for visible cracking. No visible cracks were apparent on any of these samples throughout the test period. Figure 4.14 and Table 4.3 show a comparison of all measured β's for each pair. The error bars for each propagation distance shown in Fig. 4.14 represent the variability of the 15 to 20 different measurements, where the air-coupled receiver is re-aligned. Note that the linear fits of the averaged β of each specimen have R^2 correlation coefficients higher than 94%. The results of the experimentally measured acoustic nonlinearity parameters, β_{re} for all four specimens are shown in Figure 4.15 and Table 4.3; here the values of the concrete specimens with SRA are decreased by 27% from that of the specimens without SRA, while the mortar specimens with SRA have a measured acoustic nonlinearity of 36% less than the comparable mortar specimen without SRA. Note that the amount of the coarse and fine aggregate, water-to-cement ratio, and fine aggregate-to-cement ratio are maintained to be the same in the two different sets of specimens as shown in Table 4.1, and the error bars shown in Figure 4.15 indicate the range of the

nonlinearity for all tests when the wedge transducer and air-coupled receiver were re-aligned. Importantly, the microcracks are the main source of nonlinearity in the concrete and mortar and that SRA has significant capabilities for mitigating the formation of microscale shrinkage cracks, leading to a significant reduction in the acoustic nonlinearity in these specimens with SRA.

Most importantly, Figure 4.15 shows that the acoustic nonlinearity parameters, β are decreased in both the concrete and mortar specimens by the addition of SRA and that this decrease is primarily attributed to the reduced drying shrinkage and the associated microcracks caused by the addition of SRA. These results demonstrate that the SHG technique using nonlinear Rayleigh surface waves provides an effective method for characterizing damage such as microcracks in cement-based materials.

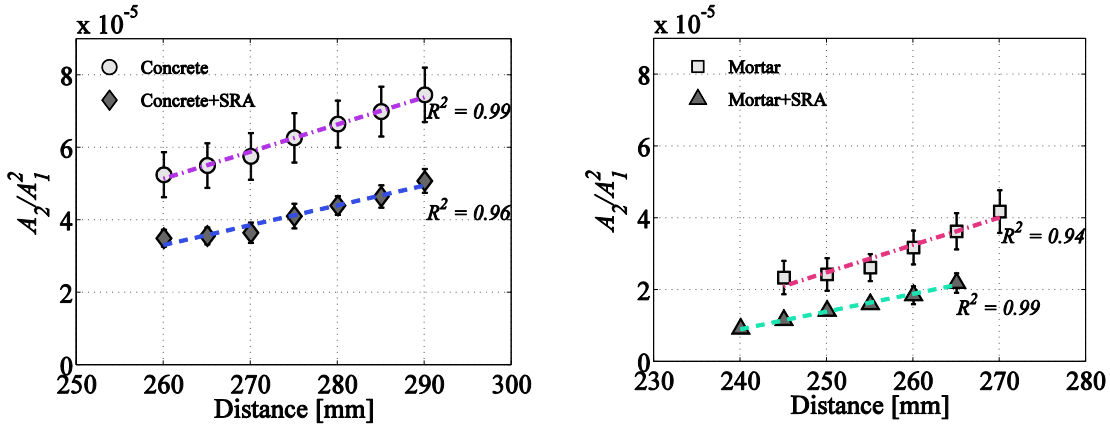

(a) The measured A_2/A_1^2 (Concrete) (b) The measured A_2/A_1^2 (Mortar)

Figure 4.14. Comparison of the measured A_2/A_1^2 and the effect of SRA on material nonlinearity.

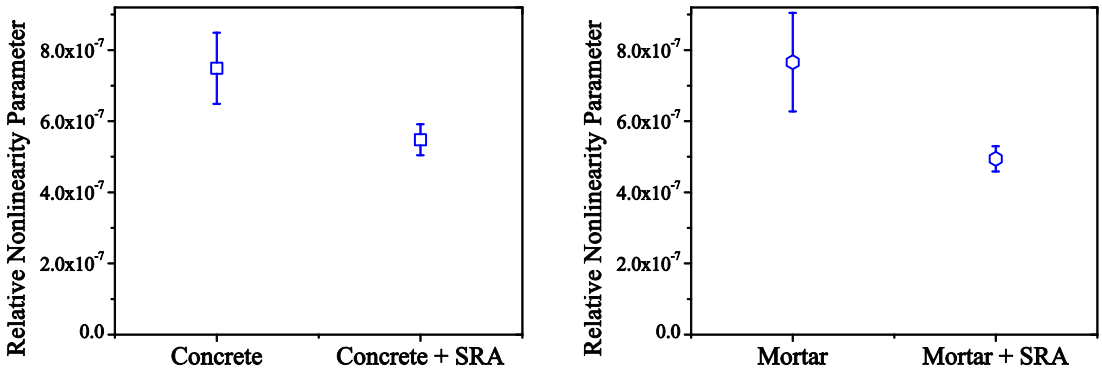

(a) β (Concrete). (b) β (Mortar).

Figure 4.15. Comparison of the measured acoustic nonlinearity parameter.

Table 4.3 The measured acoustic nonlinearity parameters.

	Concrete	Concrete with SRA	Mortar	Mortar with SRA
Acoustic nonlinearity parameter (β)	7.49×10^{-7}	5.48×10^{-7}	7.66×10^{-7}	4.94×10^{-7}

4.5.4 Sensitivity Study

To demonstrate the sensitivity of the nonlinear ultrasonic parameter to the reduced microcracks by the addition of SRA, comparisons are made to linear parameter, phase velocity and attnuation for the same four specimens. Figure 4.16 summarizs the sensitivity of each parameters. It is interesting to note tha the phase velocity (the red line in Fig. 4.16) in the concrete specimen with SRA is only 2.4% higher than in those without SRA. The results of the mortar specimens also show less than a 3% increase due to the addition of the SRA. These results also confirm an approximately frequency-independent phase velocity in the specimens within the frequency range 40 – 100kHz, meaning that the specimens can be treated as a non-dispersive medium. Therefore, it is demonstrated that

the measured nonlinearity is cumulative and solely due to microcracking damage, and not due to the dispersion. It is observed that the sensitivity of the attenuation parameter is relatively higher than that of the phase velocity as the green lined indicats in Fig. 3.18; the decrease in the attenuation cofficient are approximately 8.9% for concrete and 9.7% for mortar by the addition of the SRA. However, as the error bars in Fig. 4.16 indicated, the deviations in the attenuation parameters are too large to distinguish the effect of the SRA. Figure 4.17 shows the effect of 3.4% dosage of SRA on the mitigation of drying shrinkage in concrete. The addition of SRA results in a reduction in the surface tension, drying shrinkage, microcracks, and thus distinguishable decrease in the acoustic nonlinearity; 27% decrease in concrete, and 36% decrease in mortar. Furthermore, it is worthwhile to note that the sensitivity of the acoustic nonlinearity parameter, β is approximately 12 times greater than the Rayleigh wave velocity, and 3 times greater than the attenuation coefficients. Overall, Chapter 3 has investigated drying shrinkage and the mitigation by SRA and concluded that the SRA plays a crucial role in reducing shrinkage microcracks by moisture loss and in enhancing the durability of concrete.

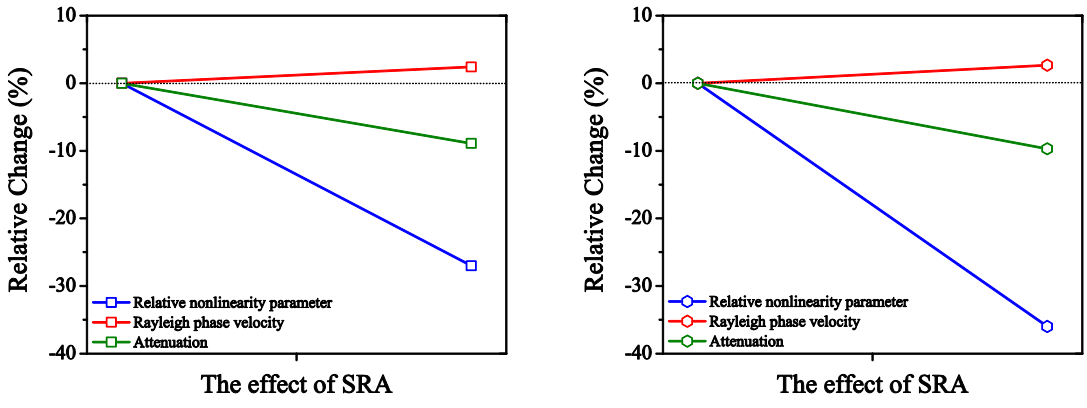

(a) Concrete (b) Mortar

Figure 4.16. Sensitivity of the acoustic nonlinearity parameter to the changes in microcracks.

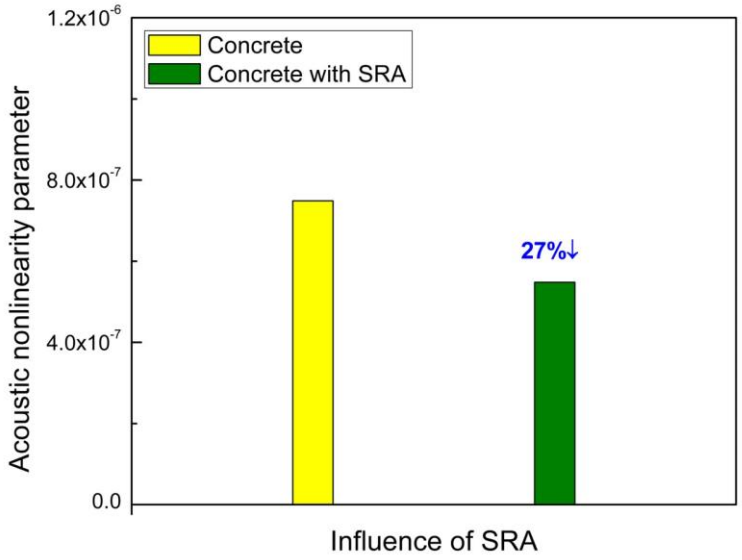

Figure 4.17. Influence of SRA on the acoustic nonlinearity parameter, β.

4.6 Summary and Conclusions

This chapter presents a new experimental technique for the application of SHG in Rayleigh surface waves in cement-based materials. A non-contact detection procedure using an air-coupled transducer is proposed to improve the applicability of nonlinear ultrasonic measurements for the possible in-situ interrogation of concrete structural components. The repeatability of the air-coupled detection method is also validated by comparison with the wedge detection method. The experimental results obtained by the air-coupled detection show that the acoustic nonlinearity parameter is repeatable and consistent, compared to the results of the conventional wedge detection technique. In

addition, the inconsistency from the surface roughness of the specimen is less important in this air-coupled detection method.

The proposed setup is then applied to quantitatively evaluate the effect of SRA on mitigating microcracks in concrete and mortar. The measured acoustic nonlinearity parameters, β are significantly decreased in specimens with the SRA and the parameters are used as an indicator for interpreting the changes in microstructure in cement-based materials. The results clearly indicate that the SRA has affected the formation of microcracks by autogenous and drying shrinkage in cement-based materials. Therefore, these results imply that the proposed SHG technique can effectively detect the presence of microcracks in cement-based materials. Most importantly, it is validated that the non-contact, air-coupled detection method provides potential field applicability for the in situ measurements of the acoustic nonlinearity parameter, β in real concrete structures.

CHAPTER 5. EVALUATION OF CARBONATION IN CONCRETE

5.1 Overview

It is well demonstrated in the Chapter 3 that the acoustic nonlinearity parameter, β can be obtained using the proposed second harmonic generation measurements. Similarly, the general process of the characterization of carbonation reaction in concrete is followed by the SHG theory. By monitoring the trends of fundamental (A_1) and second (A_2) harmonic amplitudes, the acoustic nonlinearity parameter, β is measured.

The majority of this Chapter is that the acoustic nonlinearity parameter, β as an indicator of the material state, is capable of quantitatively evaluating the progress of carbonation under accelerated conditions. The supplementary measurement tracks the profile of carbonation depth. The sensitivity of the nonlinearity parameter to microstructural condition is also verified by comparing with the measured Rayleigh wave velocity. Overall, this chapter discuss the beneficial aspect of carbonation on the durability of concrete and the advantage of the SHG technique with Rayleigh surface waves to assess the altered properties near surface of concrete.

5.2 Sample Preparation

Based on ACI 211.1[165], one concrete specimen (21.5 × 56.5 × 17.5 cm) with Type I Portland cement (ASTM C 150) [166]is prepared for both accelerated carbonation tests and nonlinear ultrasonic (NLU) measurements. River gravel coarse aggregate with a MSA (maximum size of aggregate) of 12.7 mm, and dry rodded unit weight (DRUW) of 1,646 kg/m^3 (103 pcf) and a natural sand with a fineness modulus (FM) of 3.04, absorption capacity of 1.93%, and saturated surface dry (SSD) specific gravity of 2.65 are used as aggregate. A water-to-cement ratio (w/c) of 0.60 is selected to accelerate the rate and depth of carbonation [120]. Table 5.1 shows further details on the mixture design of prepared concrete.

As described in Fig. 5.1, the freshly mixed concrete is cast, and cured for 14 days at ambient temperature while covered by polyethylene sheeting. The demolded specimen is then placed in an environmental chamber (23˚C and 95% relative humidity) in relatively moist conditions to facilitate hydration until it reaches 28 days of age. Finally, the specimen is transferred into an environmental chamber (23˚C and 50±2% relative humidity) to dry for 14 days to bring it to an equilibrium moisture condition. Additionally, five concrete blocks, each sealed on 5 sides for one-dimensional penetration of CO_2, are prepared according to the same mix design and cured and conditioned in the same manner. An indicator solution, 1% solution of phenolphthalein in deionized water with 10% v/v ethanol, are prepared for tracking the carbonation depth on freshly cut concrete surfaces.

Table 5.1 Mixture design of concrete specimen, kg/m^3 (lb/yd^3).

	Concrete
Water	271 (365)
Cement (ASTM C150 Type I)	361 (608)
Water-to-cement ratio (w/c)	0.60
Coarse Aggregate	872 (1470)
Fine Aggregate	784 (1322)

(a) Casting (b) Curing with by tarp (c) Curing in the chamber (d) Drying (completed)

Figure. 5.1. Specimen preparation.

5.3 Experimental Procedure

5.3.1 Carbonation Reaction in Concrete

The accelerated carbonation test on the prepared concrete specimen and blocks is carried out for 40 days in a carbonation chamber (Fig. 5.2), with temperature, relative humidity, and CO_2 concentration control. It has been reported in the literature that the maximum carbonation rate occurs at approximately 55-65% RH [112,170]. In this experiment, the RH is fixed to 55%. The temperature in the environmental chamber is maintained at 26℃. During the accelerated carbonation test, a continuous supply of CO_2 gas is maintained by the pressure regulator mounted on the pressurized steel cylinder and

20% CO_2 is continuously fed into the chamber [124]. Table 5.2 summarizes the environmental conditions.

Figure. 5.2. Environmental chamber for accelerated carbonation process.

In this condition, the increase in carbonation depth due to increases in temperature is negligible; the rate of carbonation is governed by the diffusion of CO_2. The test is interrupted after 0, 7, 14, 25, and 31 days of exposure so as to estimate the level of carbonation penetration in each block and the phenolphthalein indicator solution is applied to a freshly cut surface.

Table 5.2 Carbonation conditions in the environmental chamber.

Type	Fine Aggregate
CO_2 Concentration	20 %
Relative Humidity (RH)	55 %
Temperature	26 ℃

5.3.2 Depth Profile using Phenolphthalein Indicator Solution

The destructive tests are performed to determine the carbonation depth. The indicator is sprayed uniformly on each freshly broken surface of the carbonated blocks after 0, 7, 14, 25, and 31 days of carbonation in the chamber. The results show that the uncarbonated area, of pH higher than approximately 9.2, appears as purple, while the carbonated area remains colorless. Figure 5.3 shows the photographs of each cross-section of the carbonated blocks. The depth of carbonation is then measured by averaging at 7 points perpendicular to one face of the split concrete blocks, and the measured depths are 1.7, 9, 14, 18, and 21 mm, respectively. Therefore, as described in Fig. 4.4, it is determined that the carbonation depth is nonlinearly increased over time, as expected [124].

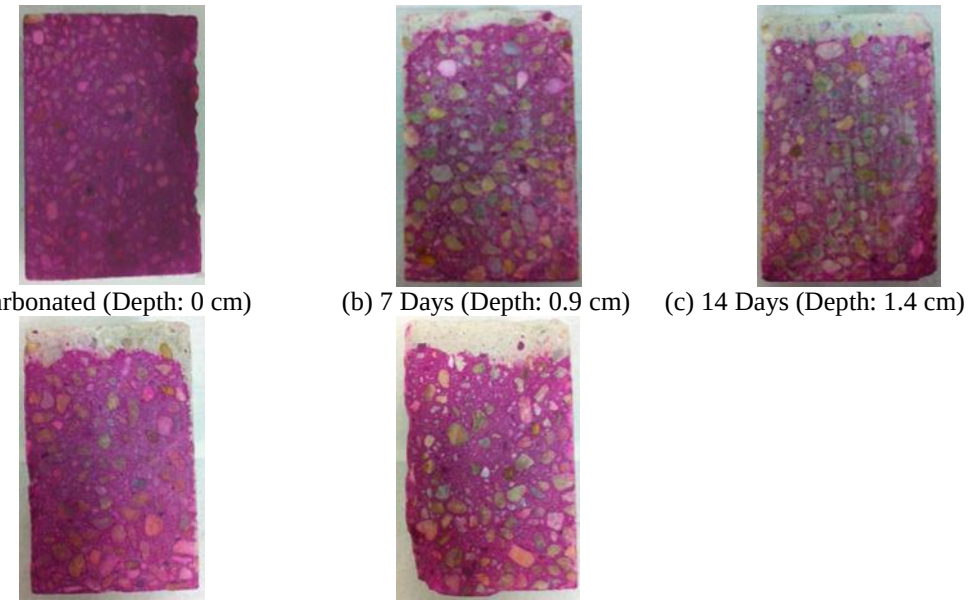

(a) Uncarbonated (Depth: 0 cm) (b) 7 Days (Depth: 0.9 cm) (c) 14 Days (Depth: 1.4 cm)

(d) 25 Days (Depth: 1.8 cm) (e) 31 Days (Depth: 2.1 cm)

Figure 5.3. Carbonation depth using the phenolphthalein indicator solution.

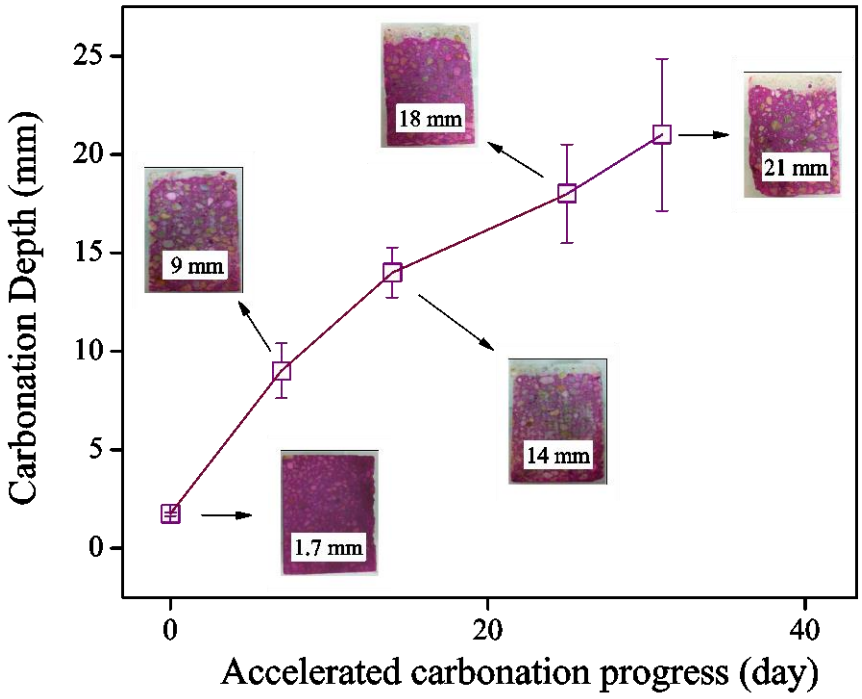

Figure 5.4. Averaged carbonation depth using phenolphthalein indicator solution.

5.3.3 SHG Measurements

The nonlinear ultrasonic technique of second harmonic generation is developed and implemented to characterize the effects of carbonation on concrete. The non-contact (air-coupled) measurements of SHG in Rayleigh surface waves are performed with the setup shown in Figure 5.5. Details on the experimental procedure to calculate the nonlinearity parameter in concrete are identical to the one described in Chapter 4. During the accelerated carbonation process, the specimen is periodically removed from the chamber for the ultrasonic measurements, which are made after 0, 3, 7, 10, 14, 19, 25, 31, and 40 days of carbonation. It is well monitored that the measured fundamental amplitude, A_1 tends to

decrease with propagation distance mainly due to the beam spreading and attenuation effects in concrete. On the other hand, due to the cumulative nonlinear effects, the second harmonic amplitude, A_2 increases with propagation distance.

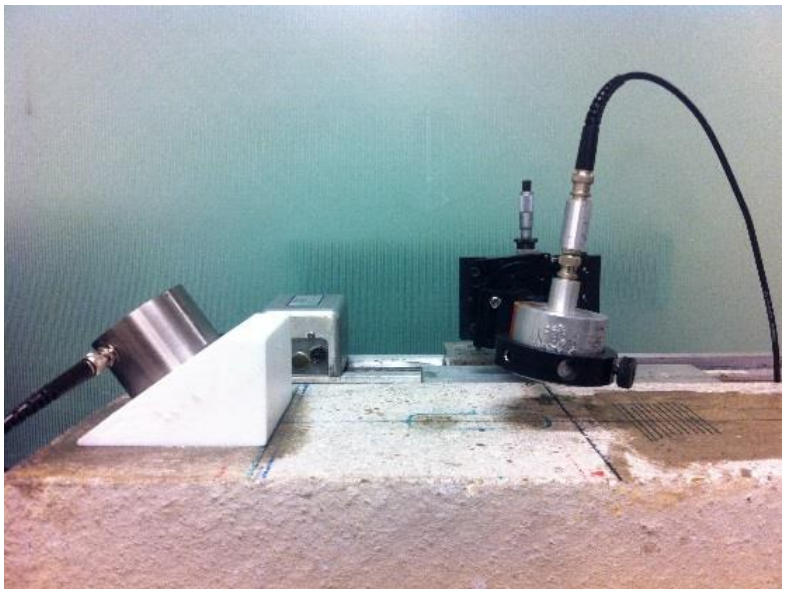

Figure 5.5. Wedge transmitter and air-coupled receiver (Rayleigh surface waves).

5.4 Evaluation of Carbonation

5.4.1 Linear Ultrasonic Measurements

The phase velocity is measured using the time domain signals received at two different propagation distances. The distance between the two measurement positions is divided by the difference in arrival times to obtain the phase velocity. The resulting phase velocities during the carbonation process are shown in Fig. 5.6 and Table 5.3. It is interesting to note that the measured phase velocity increases with the carbonation process. This increase suggests that the elastic moduli in fact increase more than the increase in density by the $CaCO_3$ formation. However, the results show only a maximum of 5.5% change during the curing for 40 days. Furthermore, the changes in phase velocity are comparable to the measurement error bars. For these reasons, it is difficult to use the phase velocity as an indicator to detect microstructural changes due to the carbonation reaction.

Additionally, it is confirmed that the concrete specimen can be treated as a weakly dispersive medium, in agreement with the results of [37], since the phase velocity for the specimen at each carbonation state is almost constant within the effective frequency range (approximately 40-100 kHz). This is important since the carbonation layer could cause dispersion; a half-space with a finite layer of different material is in general, dispersive. However, our additional measurements on these carbonation specimens demonstrate that the measured velocity difference (velocities at the fundamental versus second harmonic frequencies) is quite small (maximum 4.9% from the specimen with a 24 mm carbonation layer). Figure 3(b) also shows a cumulative second harmonic, so the effects of dispersion

are negligible and the phase velocity matching of this second harmonic is approximated in this weakly dispersive system at these relatively small propagation distances (0.03 m).

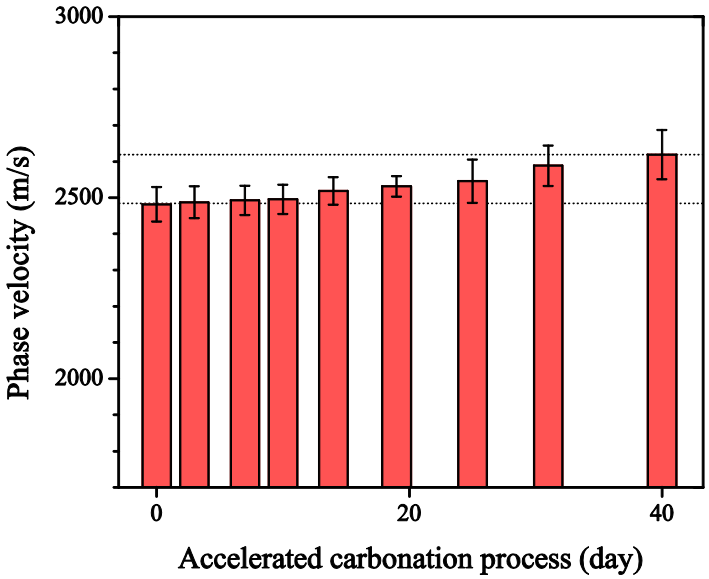

Figure 5.6. Trend of measured Rayleigh velocity with the accelerated carbonation tests.

Table 5.3 The averaged Rayleigh wave velocity.

Exposure time (day)	0	3	7	10	14	19	25	31	40
Phase velocity (m/s)	2482	2487	2493	2496	2519	2531	2546	2588	2619

5.4.2 SHG Measurements

The measurement of the SHG in nonlinear Rayleigh surface waves is performed on the concrete specimen as it is exposed to the accelerated carbonation process for 40 days. This measurement uses 45 kHz for the fundamental frequency of the transmitted Rayleigh surface waves. The wavelength at the second harmonic frequency is approximately 27.2 mm, which is greater than the maximum size of the aggregate (MSA) of 12.7 mm so that the measured second harmonic amplitudes are minimally influenced by acoustic scattering. The acoustic nonlinearity parameter, β is measured at days 0, 3, 7, 10, 14, 19, 25, 31, and 40. Each data point in Fig. 5.7 represents an average of the results from 15 to 20 repeated measurements on this specimen. The repeatability of air-coupled detection of the SHG is examined in chapter 3, and the magnitude of the error bars in this figure is mainly due to variations in the contact condition between the wedge transducer (transmitter) and the specimen surface when the wedge transducer is removed and reattached to the specimen for repeated measurements.

Figure 5.8 shows the slope of the linear fit of the A_2/A_1^2 versus the propagation distance, which represents β. Note that all of these β have R^2 correlation coefficients higher than 0.92. All measured acoustic nonlinearity parameters, β during the carbonation process are listed in Table 5.4; the measured β are shown to decrease by a maximum of 64.2% from that of the uncarbonated concrete specimen. Comparing the results in Fig. 5.6. and 5.8, the measured nonlinearity parameters are shown to decrease in a monotonic fashion while the carbonation depth is increasing in an inversely proportional fashion to the nonlinearity parameter. It is interesting to note that the values of β tend to asymptotically approach a constant value after this maximum measurement period of 40 days since the carbonation

depth is almost developed up to the wavelength (~ 27 mm) of the second harmonic Rayleigh surface waves, i.e. beyond this penetration depth, the Rayleigh waves at this frequency lose their sensitivity to the progression of carbonation.

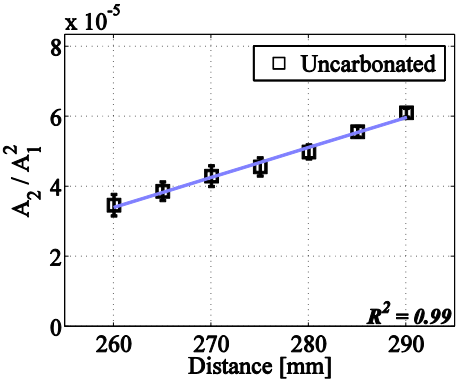

(a) Uncarbonated

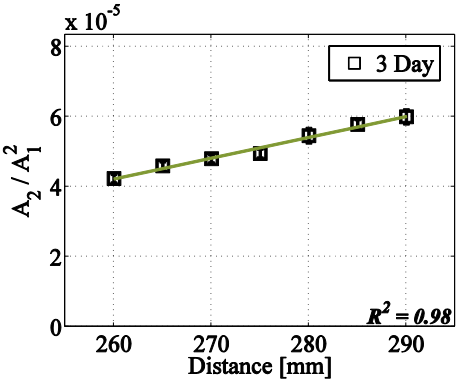

(b) 3 Days

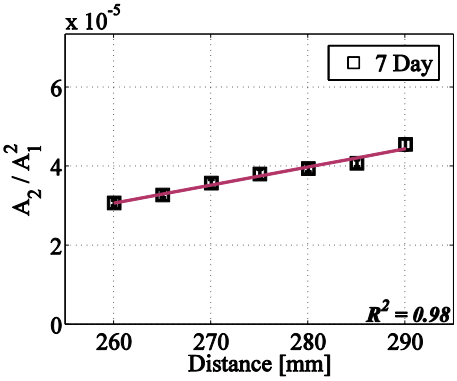

(c) 7 Days

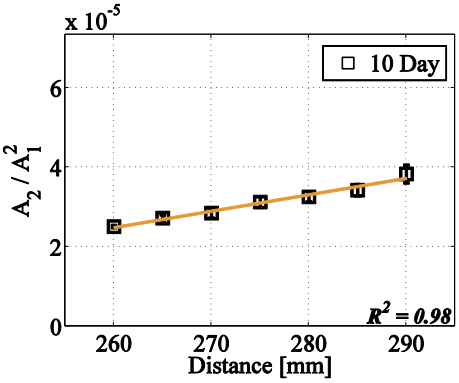

(d) 10 Days

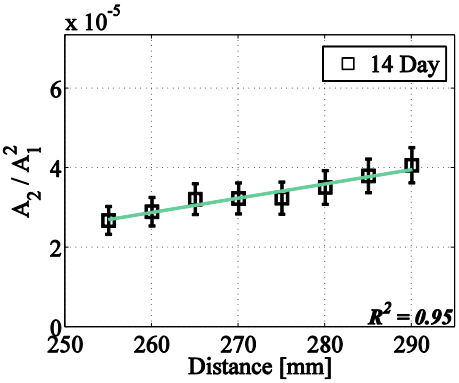

(e) 14 Days

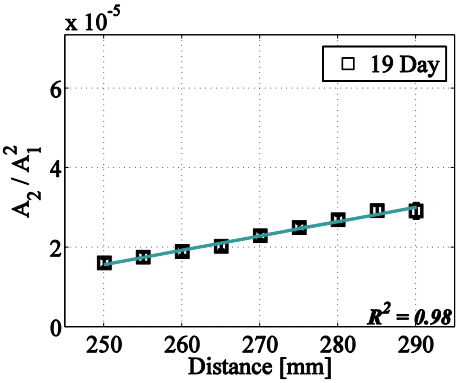

(f) 19 Days

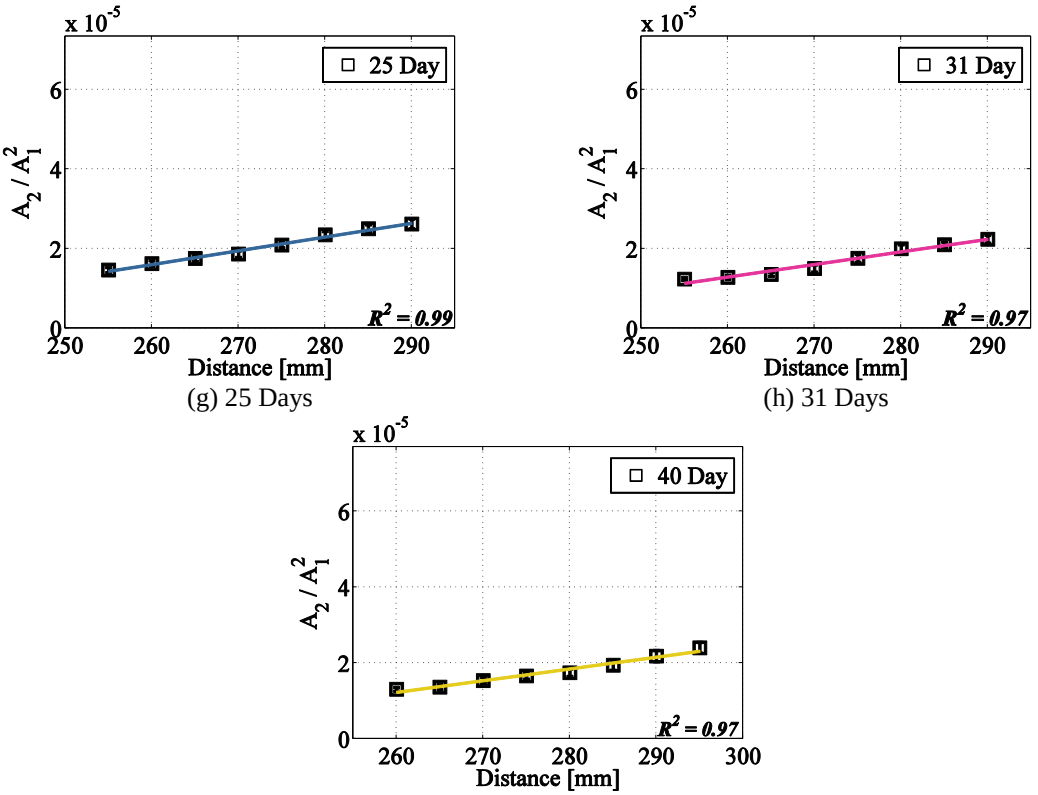

(g) 25 Days (h) 31 Days

(i) 40 Days

Figure 5.7. Averaged acoustic nonlinearity parameter by carbonation process.

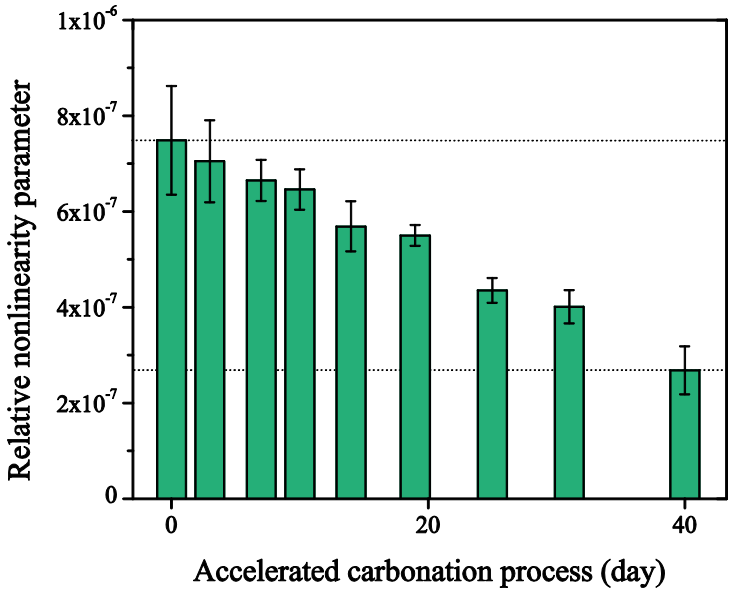

Figure 5.8. Trend of the measured acoustic nonlinearity parameters and the effect of carbonation on material nonlinearity.

Table 5.4 The averaged acoustic nonlinearity parameter.

Exposure time (day)	0	3	7	10	14	19	25	31	40
β ($\times 10^{-7}$)	7.49	7.05	6.65	6.46	5.69	5.50	4.35	4.01	2.68

5.4.3 Observations

Finally, Fig. 5.9 compares the relative changes in both the linear and nonlinear acoustic parameters, and shows that the sensitivity of the nonlinearity parameter is approximately 12 times higher than that of the Rayleigh phase velocity. More importantly, the acoustic nonlinearity parameter exhibits a sensitivity high enough to characterize the changes in microstructure, especially the decrease in porosity including filling of microcracks, induced by carbonation. Overall, this research verifies that the SHG technique using nonlinear Rayleigh surface waves provides a promising indicator capable of quantitatively evaluating carbonation in cement-based materials.

The SHG results highlight that the measured acoustic nonlinearity parameter is significantly reduced by carbonation and show the sensitivity of the measured nonlinearity parameter to the microstructural changes in the carbonated layer. Note that the environmental humidity, CO_2 concentration, and temperature along with the concrete w/c are optimized in this specimen to enhance the carbonation reaction. Based on the nonlinear ultrasonic measurements, it is shown that the carbonation of concrete leads to a reduction in material nonlinearity. Most importantly, it is likely that the decrease in the measured acoustic nonlinearity parameter is mainly attributed to the fact that some pre-existing voids and perhaps some smaller microcracks become filled by $CaCO_3$, as described in [55, 56]. Finally, it is worthwhile to note that the correlation between carbonation profile using

phenolphthalein indicator solution (Fig. 5.4) and acoustic nonlinearity parameter, β (Fig. 5.8) enables to predict the carbonation depth. For instance, as shown in Figure 5.10, the 20% increase in β approximately indicates 14 mm of the carbonation depth.

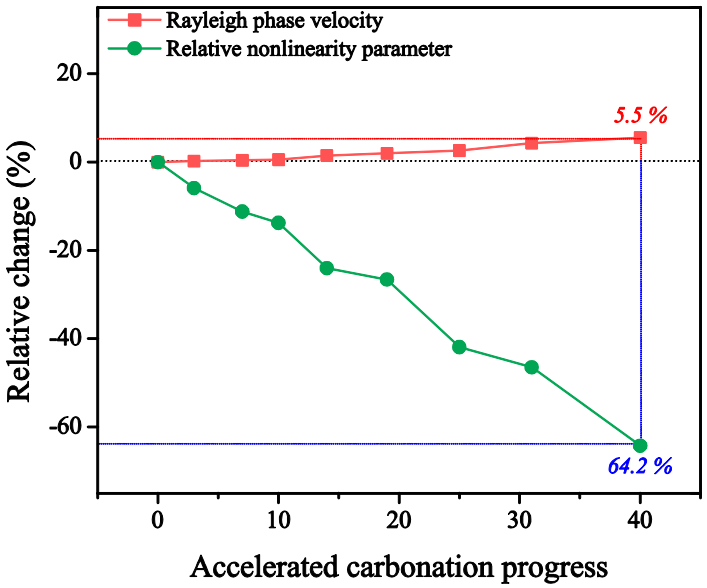

Figure 5.9. Sensitivity of nonlinear vs. linear ultrasonic parameters.

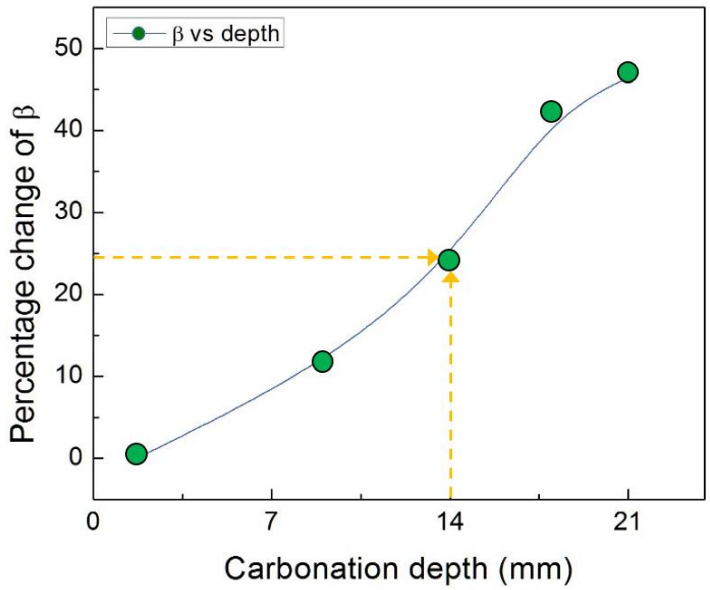

Figure 5.10 Prediction of carbonation depth using acoustic nonlinearity parameter, β.

5.5 Summary and Conclusions

This chapter studies the application of the SHG technique in nonlinear Rayleigh surface waves to concrete, in order to characterize the carbonation-induced microscale behavior of the concrete after exposure to a CO_2-rich environment, designed to rapidly develop a carbonation front in the concrete. In parallel with the nonlinear ultrasonic measurements which showed a decrease in nonlinearity with carbonation, the destructive characterization using a phenolphthalein indicator solution is performed to track the carbonation depth. The following conclusions are drawn from these experimental results:

- NDE of the microstructural behavior in the carbonated concrete is achieved by the proposed SHG technique. The acoustic nonlinearity parameter, β decreases by as much as 64.2% after 40 days of curing in the carbonation chamber, and this decrease is attributed to the formation of carbonation product, $CaCO_3$ which fills pre-existing microcracks, reducing the acoustic nonlinearity parameter, β. This can be also interpreted in such a way that concrete is "healed" itself (self-healing).
- An inverse relationship between the measured carbonation depths and acoustic nonlinearity parameters is observed.
- It is demonstrated that the acoustic nonlinearity parameter, β shows a much higher sensitivity to the carbonation-induced microstructure changes than the measured Rayleigh phase velocity (64.2% versus 5.5%). It is therefore expected that the acoustic nonlinearity parameter can be used as a quantitative index for understanding the effect of carbonation if a model that can relate β to the microstructural changes is available.

Some challenges in the use of NDE to evaluate carbonation still remain to be addressed. These measurements used a relatively low frequency pair (i.e. 50-100 kHz) to reduce the effect of acoustic scattering due to the aggregate. However, more precise characterization could be possible using a range of higher and lower frequency pairs for carbonation penetration.

CHAPTER 6. CHARACTERIZATION OF DYRING SHRINKAGE IN CONCRETE

6.1 Overview

The threefold aim of this chapter includes: (1) quantitative evaluation of drying shrinkage; (2) observation of the effect of environmental conditions in the SHG measurement; (3) quantification of the effect of shrinkage-reducing admixture (SRA) and carbonation on mitigating drying shrinkage.

Drying shrinkage by moisture migration from concrete to its environment causes stress, and microcracking and can lead to larger crack formation, which compromises performance. In an effort to characterize drying shrinkage, the SHG measurement was performed over the period from 28 days to 55 days of age in the controlled environment which is dry relative to concrete.

The process of drying is monitored by tracking mass, and acoustic nonlinearity parameter, β. Then, the nonlinearity parameter is measured as a function of the drying process and environmental interaction. [86–88]. Finally, the measured acoustic nonlinearity parameter is used to compare the microstructure modification in hardened concrete as affected by drying shrinkage, shrinkage mitigation through the use of SRA (Chapter 4), and cracking filling by carbonation (Chapter 5).

6.2 Sample Preparation and Drying Process

Two companion, long cylindrical concrete specimens of 10 × 41 cm (4 × 16 inch) were produced from ASTM C150 Type I/II Portland cement [165,166] at water-to-cement by mass ratio of 0.60, according to the mix design in Table 6.1: one for tracking the change in mass and the other for monitoring microstructural changes with the acoustic nonlinearity parameter. After fogroom curing for 28 days, the fully saturated specimens were promptly moved to a drying environment (24 ± 0.1 °C and 20% RH), where changes in mass and acoustic nonlinearity parameter are assessed as a function of time. The mechanism of drying shrinkage, aggregate restraining effect, and the changes in material's properties are summarized in Chapter 3.3.1. Note that the mass measurement is performed with the scales in the drying environment and repeated 4 times for each day; the standard deviation for the mass measurement indicates that the error of each measurement is negligible (less than 0.006 kg). Moreover, it is believed that the mass change can be used as one reference to link drying shrinkage to the measured acoustic nonlinearity parameter. It should be also noted that the specimens were not subjected to external restraint during the drying process, and exposure of the unrestrained concrete specimens to the drying environment was the driving force for any changes in the microstructure during this period.

Table 6.1 Mixture design of concrete specimen, kg/m^3 (lb/yd^3).

Concrete, m^3 (yd^3)	0.0033 (0.0043)
Water	271 (365)
Cement (ASTM C150 Type I)	361 (608)
Coarse Aggregate	872 (1470)
Fine Aggregate	784 (1322)
Water-to-cement ratio (w/c)	0.60

6.3 Technical Approach and Experimental Setup

6.3.1 SHG Measurement

Time-dependent evolution of microstructure in hardened concrete such as drying shrinkage can be well linked to the acoustic nonlinearity parameter since the drying shrinkage results in the gradual microcracking development, and microcracks are a strong source of acoustic nonlinearity parameter. Figure. 6.1 shows the principle of the SHG setup. It is validated that the SHG measurements are viable in the prepared specimens, since the measured A_2 increases with the propagation distance, properly indicating that the material nonlinearity is accumulated to the propagating ultrasonic waves. The detailed experimental procedure is described in Chapter 4. It was confirmed that the linear fit for the measured A_2/A_1^2 has the coefficient of determination (R^2) higher than 95% for all these SHG measurements, and signal averaging of 256 separate measurements is used to increase signal-to-noise ratio (SNR). Moreover, the employed SHG technique using Rayleigh surface waves has an advantage for evaluating drying shrinkage since moisture loss is occurred from the surface; the wavelengths of the fundamental (~ 5 cm) and second (~ 2.5 cm) harmonic waves are large enough to characterize the region of interest where this evaporation is occurring.

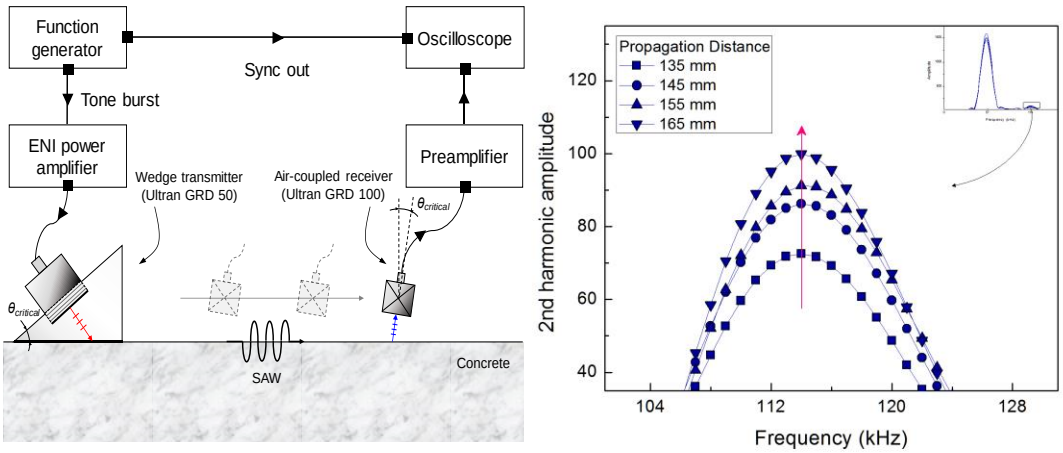

Figure 6.1. SHG measurement setup with Rayleigh surface waves.

6.3.2 Effect of Environmental Condition on Nonlinearity Parameter

During the monitoring the drying shrinkage, the environmental conditions (temperature and relative humidity) can affect both the microstructural development and SHG measurement since the rate of water evaporation in the hydrated concrete, and the attenuation in the air are dependent on the environments. Thus, in order to understand these effects, this research performs the SHG measurement in a comparison with the measured fundamental (A_1) and second (A_2) harmonic amplitudes at different temperatures. Figure 6.2 and 6.3 show the measured A_1, A_2 and A_2/A_1^2, respectively. Note that the SHG measurement is repeated by 10 times with the same condition, and averaged. The experimental results show that the averaged acoustic nonlinearity parameter, β is increased approximately 3% by only 1 °C increase in temperature. Therefore, it can be concluded that the nonlinearity parameter can be substantially changed by the huge variations of the environment parameters [171]. Based upon this observation, precise control of the environmental conditions is ensured by monitoring the temperature of both the room and

the specimen surface. Then, this research performs the monitoring of drying shrinkage in the controlled measurement room at fixed temperature (24 °C ± 0.1 °C) and relative humidity (20% ± 0%) as shown in Fig. 6.4. In addition, to track the minor variation, the two thermometers are equipped; one is for the room condition and the other is for the surface of the specimen. The humidifier and dehumidifier are also equipped in the measurement room to prevent the sudden change of environmental condition.

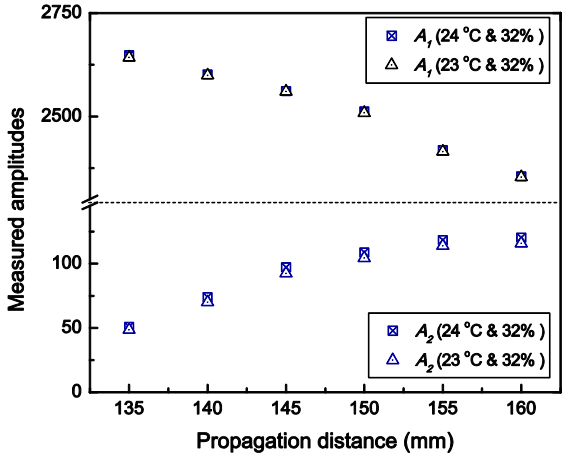

Figure 6.2. Temperature variation versus A_1 and A_2.

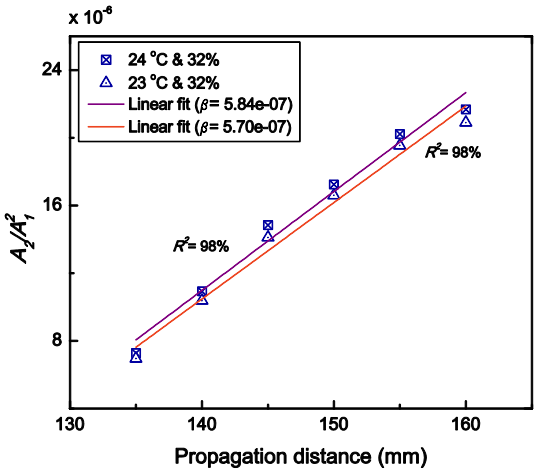

Figure 6.3. Temperature variation versus A_2/A_1^2.

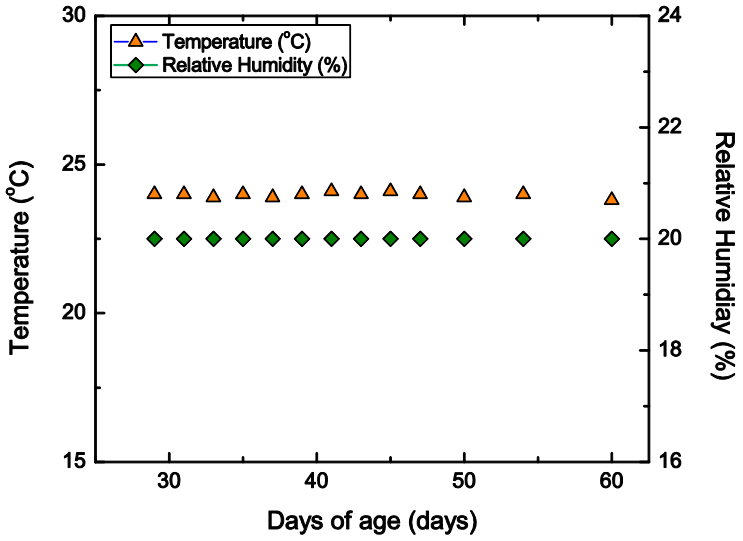

Figure 6.4. Controlled temperature and RH.

6.4 Microcracking Development by Drying Shrinkage

6.4.1 Free Shrinkage and Mass Change

Figure 6.5 shows the mass change (denoted by the red squares) of the specimen during the dying period from 28 to 55 days of age. It is observed that the mass monotonically decreases (from 7.120 kg to 6.942 kg), showing that the mass decreases rapidly up to 35 days of age and then the rate of change is asymptotically decreased [97,98]. This behavior can be attributed to the following sequences: (1) the low external RH (20%) facilitates an imbalanced pore pressure and the initial rate of water absorption [100,101]; (2) the relatively high w/c of 0.60 provides a sufficient interconnectivity among the pores [92]; (3) the loss of water first occurs in larger pores and is successively followed by

smaller pores [100]; and (4) the tensile stresses are developed as the pores become partially emptied of water cause microcracking near the drying face [86,92]. These microcracks will eventually increase the material nonlinearity particularly near the surface, and thus the acoustic nonlinearity parameter should be able to track the formation of these microcracks, and monitor the effect of drying shrinkage.

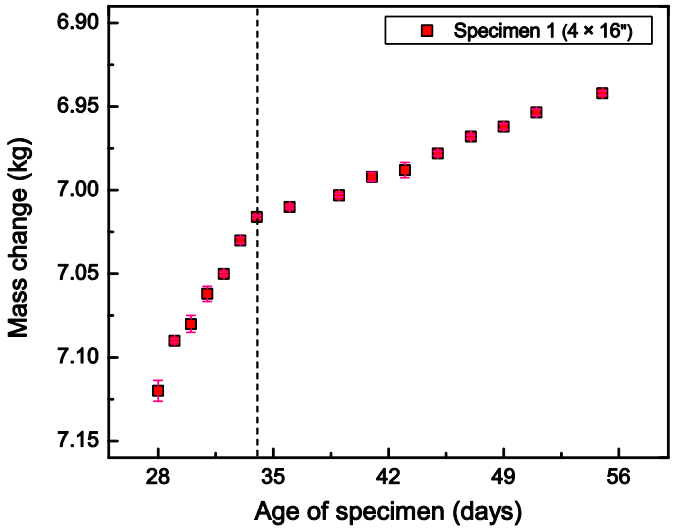

Figure 6.5. Mass losses from cylindrical concrete specimen.

6.4.2 SHG Measurements

The blue circles in the Fig. 6.6 shows the results of the acoustic nonlinearity parameter, β measured with the SHG method as a function of age. The SHG measurement is repeated 2-3 times as the microstructural condition is continuously altered with time. The repeated SHG measurements show that the maximum difference in the measured β is less than 2%. The results show that the acoustic nonlinearity parameter is significantly increased by 218% (from 2.27 $\times 10^{-7}$ to 7.24$\times$ 10^{-7}), while the mass has a maximum

decrease of 2.7%. The 218% increase in β is due to the formation of microcracks as the moisture migrates near the surface, and is evidence of the high sensitivity of β to changes in the microstructure. Note that since both w/c and aggregate (type and volume) affect the rate and extent of the microcracking development during drying shrinkage, these effects on the SHM measurement will only re-scale the y-axes (or the relative extent of shrinkage and material nonlinearity) in Fig. 6.6.

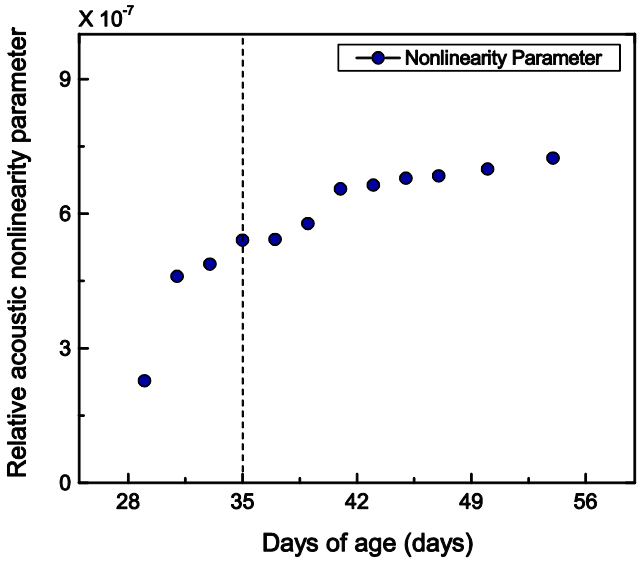

Figure 6.6. Profile of the measured acoustic nonlinearity parameter.

6.4.3 Observations

To track the trend of each parameter, the percentage change of both mass and acoustic nonlinearity parameter is plotted together (Fig. 6.7). As each curve fit indicates, the trends of both the measured mass change and acoustic nonlinearity parameter follow each other. This means that the mechanical phenomena resulting from the mass reduction

are readily detected with the acoustic nonlinearity parameter, β. Moreover, the logarithmically increasing trend of the measured β is in a good agreement with the typical curve of drying shrinkage versus time and thus becomes an evidence of the fact that the dried surface of the specimen reaches equilibrium with the environment, and thus the tensile stresses developed relax over time [92]. Finally, the high sensitivity of the measured acoustic nonlinearity parameter reveals that the effect of drying shrinkage over the period from 28 to 56 days of age on durability of the hardened concrete cannot be ignored.

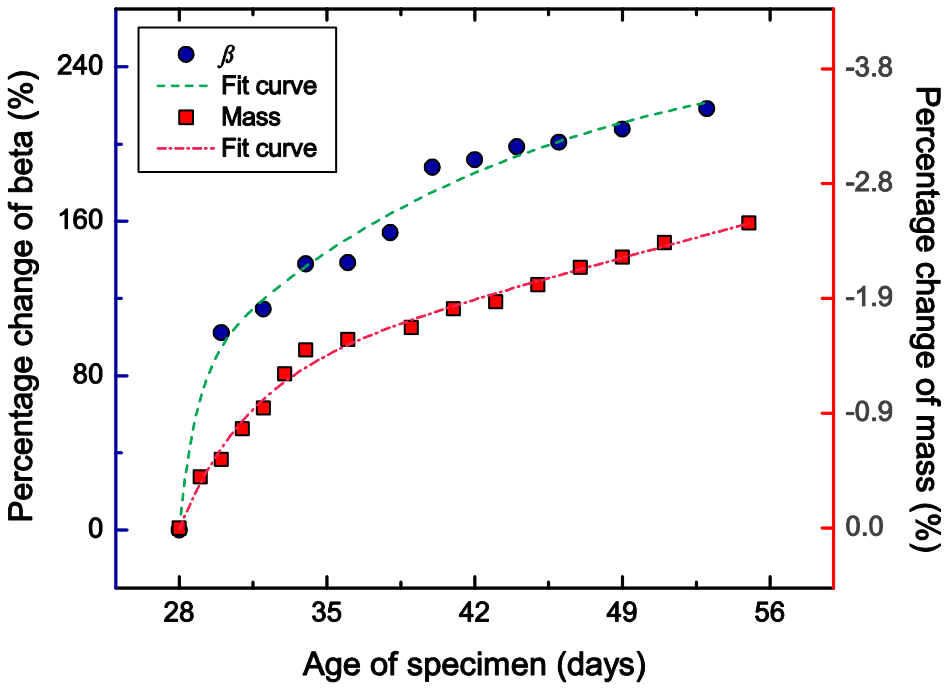

Figure 6.7. Relative changes of the mass and acoustic nonlinearity parameter, β.

6.5 Mitigation of Drying Shrinkage: Role of SRA and Carbonation

To comprehensively understand the microstructural condition in hardened concrete, this research evaluates the effect of both shrinkage-reducing admixture (SRA) and aging by carbonation on concrete subjected to drying. Figure 6.8 shows the current acoustic nonlinearity results obtained through monitoring drying shrinkage together with those for concretes containing SRA (3.4% of the total mass of water) and those exposed to carbonation (26 °C, 55% RH, and 20% CO_2 supply). These provides a comprehensive story of microcrack formation and filling in relationship to the measured β. It is important to note that the mix proportions and curing history for the drying shrinkage, SRA, and carbonation studies are identical and that each set of SHG measurements is performed at a fixed temperature and RH; by minimizing these potential sources of variability, the effects of shrinkage and carbonation can be better isolated. By combining these data, the effects of shrinkage, shrinkage mitigation, and subsequent aging by carbonation can be assessed comparatively.

Figure 4.14 illustrates the changes in the microstructure in concrete, as measured through the acoustic nonlinearity parameter, as the concrete is removed from fogroom curing (A) and placed in a drying environment (A→B) and then subsequently carbonated (B→C). The additional point B′ represents the acoustic nonlinearity parameter measured during drying for concrete cast with SRA. It is interesting to note that the measured acoustic nonlinearity parameter at 55 days of age (7.24×10^{-7}) is quite similar to those for concrete without SRA and for uncarbonated concrete (7.49×10^{-7}). The acoustic nonlinearity parameters in Fig. 4 are normalized by their respective values for the 55-day

old specimen in order to remove any variations due to age, as this figure represents the results from three different specimens.

After 28 days of hydration (A), the microstructure near the surface experiences water evaporation. The effects of this drying shrinkage are mitigated in the specimen containing SRA due to changes in the surface tension in the pore solution by the admixture addition [110]. Therefore, the path from B to B′ shows the effect of SRA in mitigating microcracking during this period of drying shrinkage. By the addition of SRA during casting, the acoustic nonlinearity parameter (β') is decreased by 27% from that of the concrete without the SRA (B). Moreover, a path from the casting (0 days of age) to B′ (55 days of age) indicates that rate of drying shrinkage at early-age is also likely significantly mitigated by the addition of SRA.

Accelerated carbonation is induced in an environmental chamber from 55 to 95 days of age [58]. The effect of carbonation and the formation of new products (e.g., calcium carbonate, $CaCO_3$) on microstructure, as measured through the acoustic nonlinearity parameter, is traced by following the path from B towards C. The 64.2% decrease in the acoustic nonlinearity parameter is due to the fact that the pre-existing voids and microcracks (including those induced by drying shrinkage) in the concrete are at least partially filled by the relatively insoluble carbonation reaction product, $CaCO_3$. These results suggest that some "self-healing" of shrinkage-induced microcracking has occurred and the extent of this effect is measureable by changes in the nonlinearity parameter. These results also show that the effects of aging can be measured independently among concretes of known or similar initial composition and nonlinearity.

Based upon the integrated results from three independent studies, it is quantitatively observed that the expected concrete behavior during drying shrinkage is well reflected in this plot of the acoustic nonlinearity parameter as a function of concrete age. This is due to the fact that the acoustic nonlinearity parameter is extremely sensitive to shrinkage-induced microcracking. Moreover, two different effects (shrinkage mitigation and carbonation) are unambiguously distinguished by the acoustic nonlinearity parameter, demonstrating that the microcracking development due to drying shrinkage is effectively mitigated by the dosage of SRA and the resultant microcracking compensated for by the carbonation process. Most importantly, they demonstrate that the acoustic nonlinearity parameter is a useful tool for monitoring microstructure changes in hardened concrete and that a precise damage state evaluation can be determined with the SHG technique.

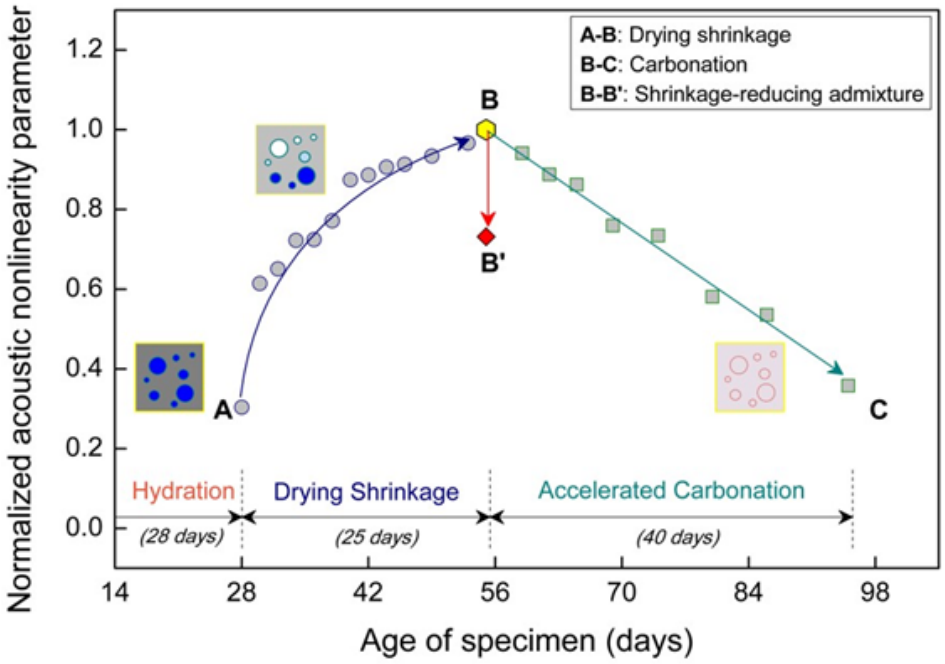

Figure 6.8. Time-dependent microstructural condition in hardened concrete: drying shrinkage (28 to 55 days), effect of SRA on mitigating drying shrinkage (at 55 days), and self-healing with carbonation (55 to 95 days).

6.6 Summary and Conclusion

This research demonstrates that the acoustic nonlinearity parameter obtained from the proposed SHG measurement with Rayleigh surface waves is suitable for monitoring microscale damage evolution in concrete with large sensitivity. The experimental study demonstrates that the sensitivity of the acoustic nonlinearity parameter is approximately 87 times higher than that of the mass change during the drying process from 28 to 55 days of age. The drying shrinkage in this period produces a logarithmically increasing trend in the acoustic nonlinearity parameter, that follows the trend of the mass reduction. Thus the influence of drying shrinkage on the microstructure, including microcracks which are expected to be more prevalent near the drying surface, can be measured through the SHG method with Rayleigh surface waves.

In an effort to understand the long-term performance of concrete, a comprehensive comparison of the nonlinearity in concrete considers the effect of drying shrinkage, shrinkage mitigation by SRA, and carbonation after drying shrinkage. The results clearly show that the increases in the acoustic nonlinearity parameter due to the generated microcracks during drying shrinkage are significantly mitigated by both carbonation (up to 64.2%) and the addition of SRA (up to 27%). This research demonstrates that the SHG method with Rayleigh surface waves has the potential to nondestructively monitor the evolution of microcracks over time in hardened concrete, which can play a crucial role in understanding microstructural changes in concrete from early-age to long-term performance.

CHAPTER 7. MONITORING ASR DAMAGE IN LARGE-SCALE CONCRETE STRUCTURES

7.1 Overview

According to the reported literature, in spite of significant progress in the area of the NLU and NLA techniques, several issues are still open for research. For example, it is not yet validated that nonlinear methods are indeed effective for monitoring large scale concrete structures; damage evaluation of in-service concrete structures cannot be realized until this issue is addressed. Also, there is the need for measurement techniques that can eliminate the inconsistent contact conditions between the transducer and the concrete surface. Due to these reasons, research on the nonlinear NDE of large-scale concrete structures has rarely been reported in the literature.

This chapter exploits the second harmonic generation (SHG) in nonlinear Rayleigh surface waves to assess alkali-silica reaction (ASR) damage in large-scale concrete slabs. The major objective of this chapter is to investigate the feasibility of using SHG of nonlinear Rayleigh waves to assess the level of microscale damage induced by ASR in large-scale concrete slabs. The viability of the proposed SHG method is demonstrated by measuring the acoustic nonlinearity parameter, β in a non-reactive control slab and three reactive slabs at two different damage states. Of critical importance for the impact of this research is that the wavelength of these ultrasonic waves is much larger than the microscale damage being monitored. They have the potential to increase sensitivity with less scattering

from the coarse aggregate, and thus monitor microcrack development in these large-scale structures. This is in contrast to linear ultrasonic techniques where such sensitivity to microscale damage requires the use of high frequency pulses, and the associated significant distortion and attenuation from scattering. Conclusions about the potential applicability of the SHG technique to the large-scale concrete structures are drawn as well as the assessment of ASR damage.

7.2 Sample Preparation

Two plain concrete slabs were constructed simultaneously. One was designed and conditioned to expand as from ASR; the other was constructed to serve as a non-expansive control specimen. Each slab had three small-scale accompanying prisms to track the compressive strength. As shown in Fig. 7.1, the slab dimensions were 1,219 × 914 × 203 mm (48 × 36 × 8 in.) and the prism dimensions were 102 × 76 × 406 mm (4 × 3 × 16 in.). The materials for the reactive slab include a non-reactive coarse aggregate (NCA) from central Alabama (USA), a highly reactive fine aggregate (RFA) from El Paso, Texas (USA), and ASTM C150 Type I/II Portland cement [166]. Sodium hydroxide was used in the reactive slab to increase their equivalent alkali content to 1.25% by mass of cement. The materials for the non-reactive control slab include a non-reactive coarse aggregate (NCA) and a non-reactive fine aggregate (NFA) from the same quarry in central Alabama (USA) and ASTM C150 Type I/II Portland cement. The w/cm ratio for both mixes was 0.50. Table 7.1 presents the material properties of the cement and aggregates used in

mixture proportioning. Table 7.2 gives the mixture proportions for the reactive and non-reactive mixes.

The formwork for the slabs was constructed with pressure-treated lumber and cabinet-grade plywood. The four slabs were cast at a time. Each slab was cast using three batches of concrete; three slabs were designed and conditioned to expand from ASR and the fourth served as a non-expansive control specimen. The batches were mixed and placed rapidly to avoid cold joints. To ensure consolidation, the slabs were vibrated in three layers and forms were struck on the sides with a rubber mallet. Slump, unit weight, and air content were measured for each batch in accordance with ASTM C143 [172], ASTM C138 [173], and ASTM C231 [174]. The fresh concrete temperature was also recorded for each batch. Compressive strength of 100 × 200 mm (4 x 8 inch) cylinders at 7 and 28 days was also measured in accordance with ASTM C39 [175]. The average 28-day compressive strength was 30.5 MPa (4430 psi) for the three reactive slabs and 35.9 MPa (5200 psi) for the non-reactive control slab. This strength disparity results from the use of added alkalis and has been documented in prior research [176].

Table 7.1 Material properties of the cement and aggregates.

Material	w/c	Absorption Capacity (%)	Bulk Specific Gravity (Oven Dry)
Cement	0.60	-	3.15
NCA	-	0.7	2.74
RFA	-	1.2	2.59
NFA	-	1.0	2.70

Table 7.2 Mixture proportions for the reactive and control slabs.

Material	Quantity, kg/m^3 (lb/yd^3)	
	ASR Reactive	ASR Control
Cement	420 (708)	420 (708)
Water	210 (354)	210 (354)
NCA (oven dry)	1095 (1845)	1095 (1845)
RFA (oven dry)	608 (1025)	-
NFA (oven dry)	-	639 (1077)
NaOH	7.0 (11.8)	-

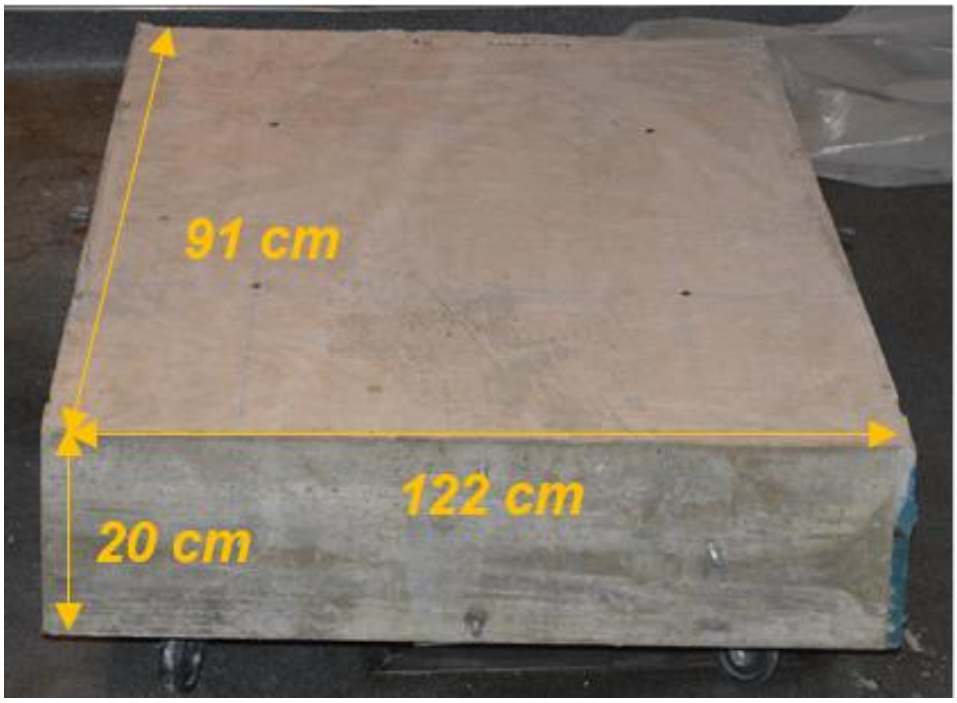

Figure 7.1. Prepared concrete slab (Reactive).

7.3 Experimental Procedure

7.3.1 Alkali-Silica Reaction Process

The concrete slabs were moist-cured at 23 °C ± 2 °C (73.4 °F ± 3.6 °F) for seven days after casting. The reactive specimens were then conditioned at 38 °C ± 2 °C (100 °F ± 3.6 °F) and 98% RH ± 2% for the next four weeks to encourage the development of ASR (Fig. 7.2), and the control specimen was maintained at 23 °C ± 2 °C (73.4 °F ± 3.6 °F) and 50% RH ± 4%. The reactive specimens were cooled to 23 °C (73.4 °F) for no more than 24 hours on the days of expansion and ultrasonic measurements to match the temperature at the time of the initial expansion measurements. Following the high-temperature, high-humidity conditioning period and the initiation of expansion from ASR, the specimens were transferred to the Electric Power Research Institute's (EPRI) NDE laboratory in Charlotte, North Carolina (USA), where the second round of ultrasonic measurements were conducted in a 23 °C (73.4 °F) room.

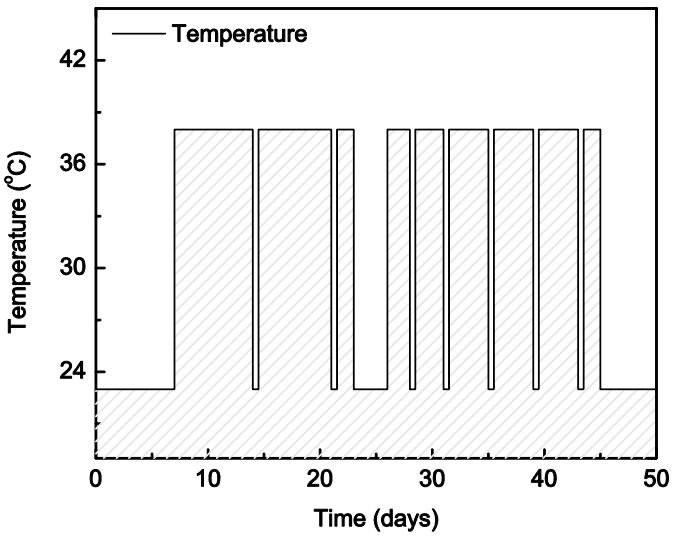

Figure 7.2. Temperature control (38℃ to 23℃).

7.3.2 Expansion Testing Methods

To track the length change, hex bolts with conical targets drilled into their ends for DEMEC gauge measurements (manufactured by Mayes Instruments) were threaded into the formwork and embedded into the concrete. Four hex bolts were embedded in each side of the slabs. Two bolts were spaced 500 mm (19.7 in.) apart for horizontal expansion measurements and two bolts were spaced 150 mm (5.9 in.) apart for vertical expansion measurements. The bolts were centered both vertically and horizontally on the slab face. Figure 7.3 shows an example of the horizontal expansion measurements.

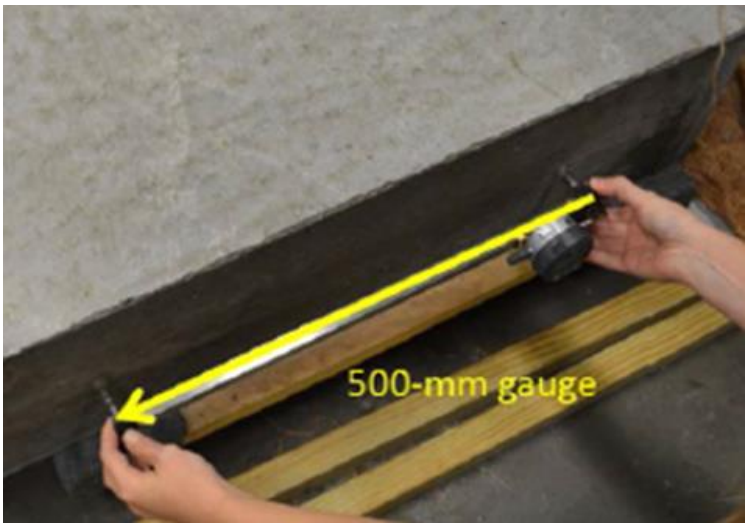

Figure 7.3. Expansion measurement.

7.3.3 Ultrasonic Measurements

A schematic of the setup used to measure the nonlinear Rayleigh surface waves is shown in Figure 7.4. A tone-burst signal of 12 cycles at 48 kHz is generated by a function generator (AGILENT 33250A) with a peak to peak voltage of 260 mV. A power amplifier (ENI Power Amplifier) amplifies the signal by 50 dB and the amplified signal is fed to the

50 kHz transmitting transducer (Ultran GRD 50). The measurement principle is identical to the one in chapter 3 and 4. However, it is important to note that the excitation frequency should be carefully determined by consideration of the ratio of a wavelength-to- maximum particle size, and the effective frequency range of the transducers; 48 kHz for the fundamental harmonic and 96 kHz for the second harmonic is determined as an optimized pair for the inspection of large-scale concrete slab where the MSA is around 2 cm. For the generation of Rayleigh surface waves, the transmitting longitudinal wave transducer is coupled to a Teflon wedge by vacuum grease. The wedge angle is set at 36.3˚ according to Snell's law to ensure the generation of Rayleigh surface waves in the concrete slabs. A 100 kHz air-coupled transducer (Ultran GRD 100) with a tilt angle of 8˚ detects the Rayleigh surface waves leaked into the air. A broadband preamplifier (Digital Wave Inc.) amplifies the detected signals by 55 dB. The electrical output signal is digitized with an oscilloscope (Tektronix TDS 5034B Digital) and averaged 256 times to increase the signal-to-noise ratio. The entire SHG measurement system is triggered by the sync signal from the function generator. Finally, a Hann widow and fast Fourier Transform (FFT) are applied to the steady state part (8 cycles) of the averaged time domain signal to calculate the frequency spectrum. The fundamental (A_1) and second harmonic (A_2) amplitudes are obtained at multiple locations along the propagation distance, and accordingly the acoustic nonlinearity parameter, β is obtained.

The phase velocity of Rayleigh waves at the fundamental frequency (48 kHz) is calculated using the time-domain signals at different positions acquired in the SHG measurements (Fig. 7.6), and the reliability of the measured velocity is validated by [50].

The measured Rayleigh wave velocity using the time-domain signals is in good agreement with that by the method in [50].

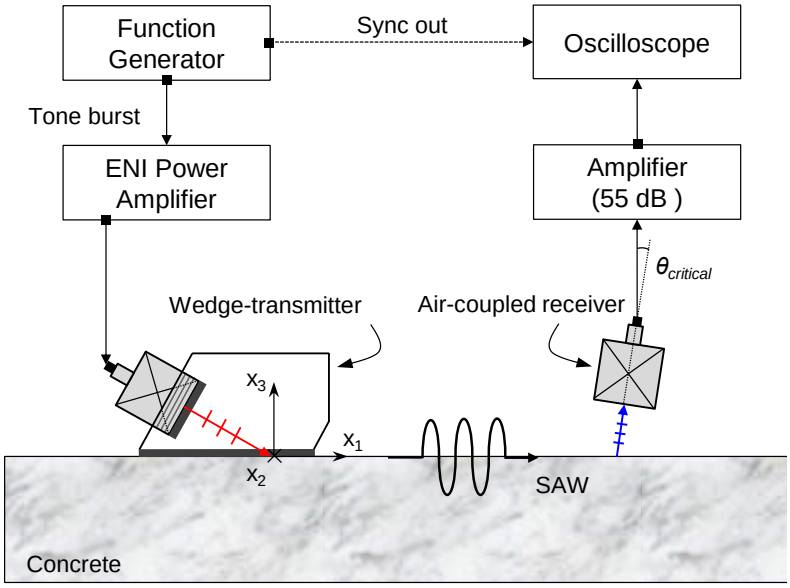

Figure 7.4. Schematic of the NLU setup.

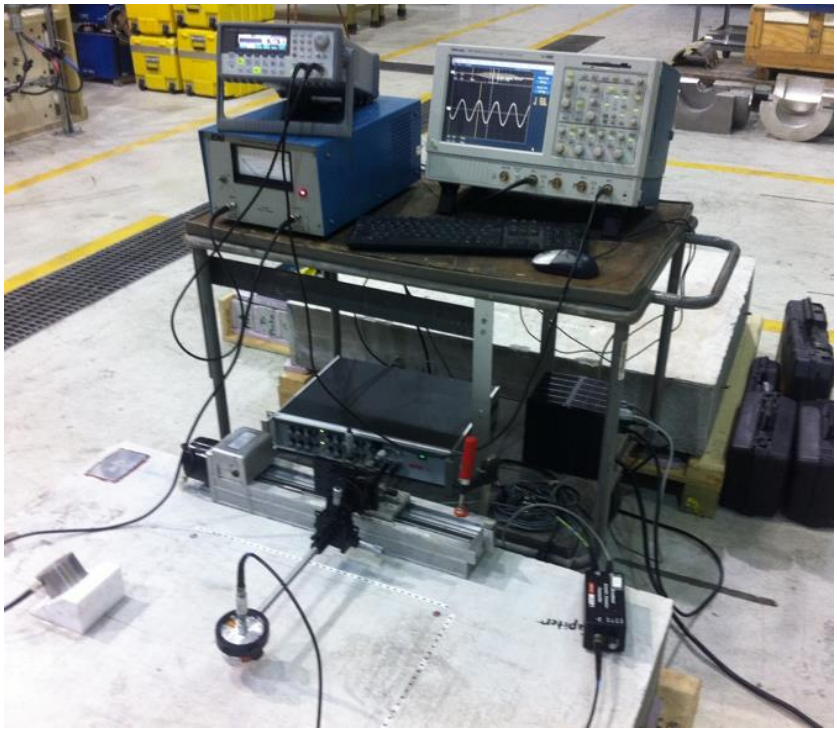

Figure 7.5. The SHG setup for large-scale concrete.

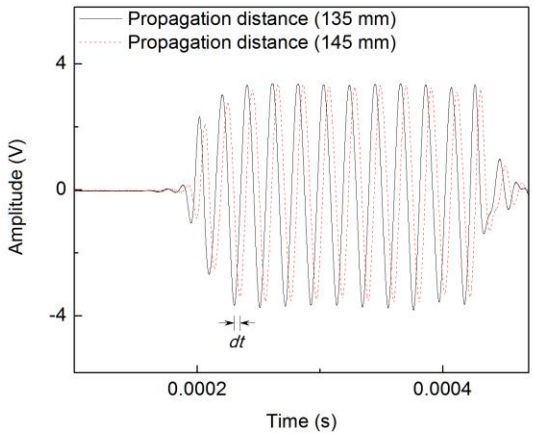

Figure 7.6. Received time domain signals at different propagation distances.

7.4 Application to Large-Scale Concrete Slabs

7.4.1 Surface Expansions

Figure 7.7 shows the average measured surface expansion versus age for the three reactive and one non-reactive control slabs. The arrows indicate the timing of the ultrasonic measurements, noting that continuous monitoring with these ultrasonic techniques was not possible due to the geographic location of the slabs, which was different from the location of the ultrasonic equipment. However, Fig. 7.7 (b) clearly shows that the timing of the ultrasonic measurements captured two different damage states in the reactive slabs, before and after extensive ASR reactions, when the expansion starts to increase at the first day of the SHG measurement, and one when it reaches near peak values at the second day of the SHG measurement. Figure 7.7 (a) shows no expansion for the non-reactive control slab throughout its entire history. Except for limited macrocracking at the slab edges, far away

from the location of the ultrasonic measurements, no damage was visible during the SHG measurements.

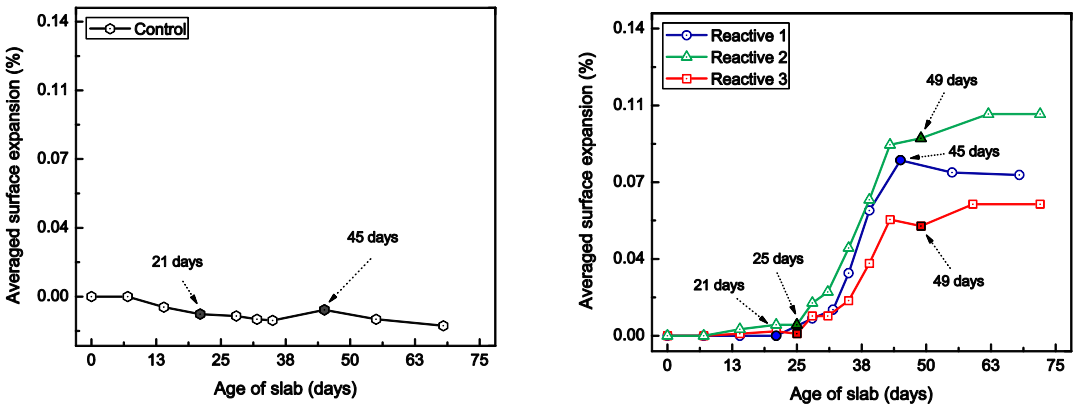

(a) Surface expansion for non-reactive slab. (b) Surface expansion for reactive slab.

Figure 7.7. Results of expansion measurements.

7.4.2 Phase Velocity of Rayleigh Surface Waves

Figure 7.8 and Table 7.3 show the averaged Rayleigh wave velocities for the non-reactive control and reactive slabs at the two different measurement days; the Rayleigh wave velocity decreases by approximately 1% for the non-reactive control slab and 21% (Reactive 1), 27% (Reactive 2) and 34% (Reactive 3) for the three reactive slabs. The decrease in the wave velocity for the reactive slabs is most likely related to the reduction in the elastic moduli due to the presence of ASR-induced damage. For the non-reactive slab, in contrast to the 12% increase in β, the expansion and Rayleigh wave velocity results show almost no changes, -0.002% and 1%, respectively. The ability to track subtle (early-age) damage progression such as drying shrinkage in the non-reactive slab is an indication of the sensitivity of β to microscale damage in these large-scale slabs. Previous work comparing linear and nonlinear Rayleigh waves for microcrack detection in laboratory-

scale specimens [37,58] showed that velocity measurements in this frequency range are relatively insensitive to the formation of microcracks.

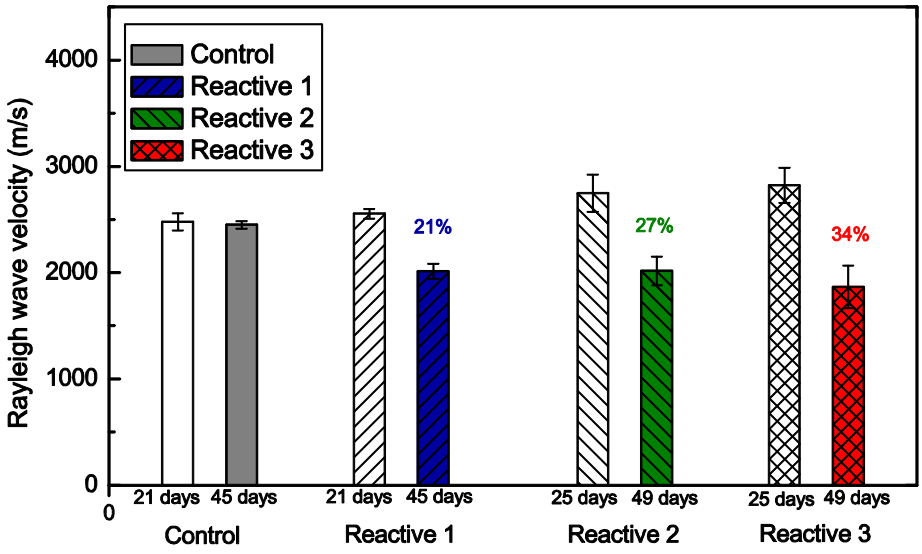

Figure 7.8. Measured Rayleigh wave velocity (m/s).

7.4.3 SHG Measurements

The SHG measurement is repeated four to five times by removing and reattaching the wedge/transducer transmitter and the air-coupled receiver. Figure 7.9 shows an example of the measured time domain signal with Hann-windowed signal, and its frequency spectrum. The excitation frequency is determined based on the wavelength-to-maximum aggregate size ratio, i.e., to minimize the unwanted scattering effects and the effective frequency range of the transducers such that the shortest wavelength is greater than the largest sized aggregate. The trend of A_1, A_2, and the ratio for the large-scale concrete slabs are shown in Figure 7.10. The slope of the linear fit represents the value of

the acoustic nonlinearity parameter; the coefficient of determination (R^2) is 99% for this case. Importantly, these results are corresponding to the SHG measurement described in previous chapter. Moreover, trends of A_1, A_2, and the linear relationship of A_2/A_1^2 versus the propagation distance are well evidenced by the theory of second harmonic generation. Therefore, it is clearly demonstrated that the proposed SHG setup within the 40 to 120 kHz frequency range is capable of measuring the acoustic nonlinearity parameter, β in concrete.

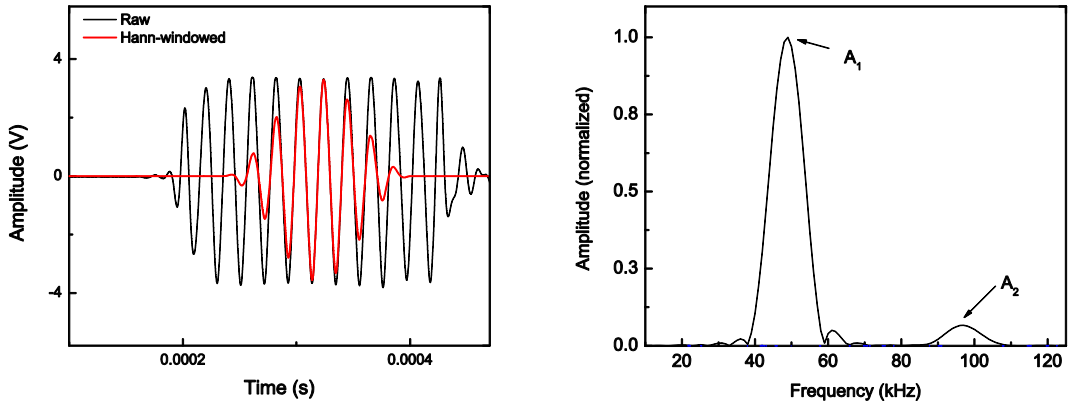

(a) The received time domain signal with a Hann window width.

(b) Normalized frequency spectrum.

Figure 7.9. Time signal and Fourier spectrum for NLU measurement (45kHz and 90 kHz).

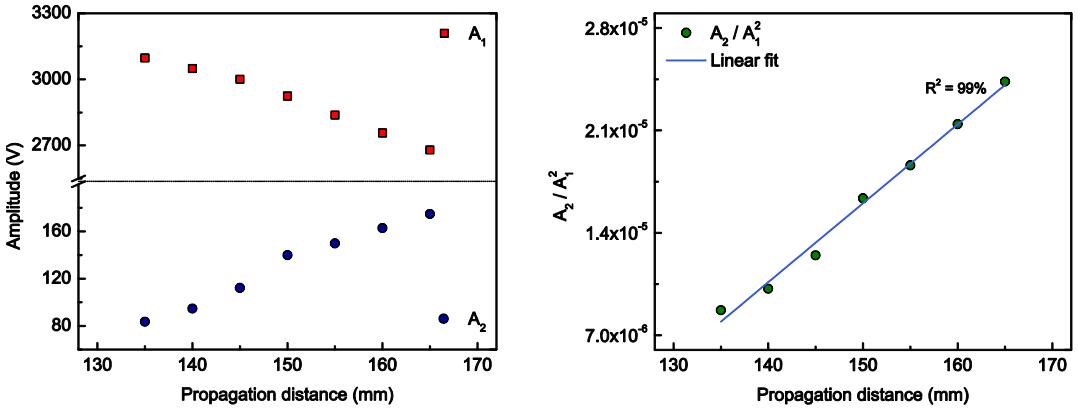

(a) Measured A_1 and A_2 over propagation di stance.

(b) A_2/A_1^2 versus propagation distance.

Figure 7.10. The SHG measurements from large-scale concrete slabs.

It is experimentally confirmed that second harmonic amplitude no longer increases beyond 17 cm due to the effect of the attenuation, indicating that there is a limited propagation distances (approximately 3 to 4 cm for concrete), where the material nonlinearity is dominantly accumulated into the propagating waves and thus the measured A_2 shows monotonically increasing trend. It is also important to note that the propagating Rayleigh wave is relatively free from the distortion by the boundary reflected waves within the propagation distances since the geometry of the large-scale concrete slabs guarantee that there is no distortion by the boundary-reflected waves.

As shown in Figure 7.11, a logical consequence of this overall behavior is the linear increase of A_2 / A_1^2 with propagation distance. The linear trend for 45 days (Reactive 1) shown in Figure 5.9 illustrates that the second harmonic waves are reliably detected, even with the existence of the developed microcracks and damage around the aggregate.

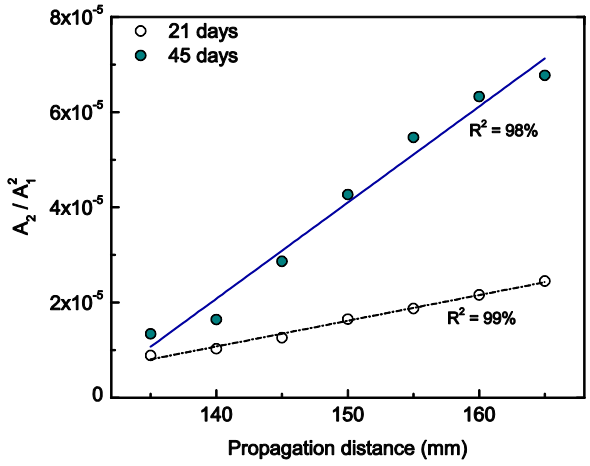

Figure 7.11. Reference vs ASR Damage (Reactive 1).

The measured acoustic nonlinearity parameter, β for four slabs at the two damage states are shown in Fig. 7.12 and Table 7.3. The error bars are from four to five repeated measurements at the same location, by removing and reattaching the wedge transmitter and the air-coupled receiver. An R^2 greater than 96% for the measured acoustic nonlinearity parameter, β for all 4 slabs indicates the high accuracy of these measurements. The results from the non-reactive control slab show that β increases by approximately 12%, which can be attributed to microcracking induced by drying shrinkage as described in Chapter 6, and any thermal cycles on the slabs, including those that could have occurred during transit to EPRI. In contrast, β for the three reactive slabs increases by 274% (Reactive 1), 496% (Reactive 2), and 675% (Reactive 3) between the measurement periods. These large increases in β in all three reactive slabs indicate that β is very sensitive to the microscale damage occurring in these large-scale slabs due to the presence of ASR, including gel formation, gel swelling, and microcracking. A direct comparison of the β results for these three different reactive slabs is impossible, since each slab has different starting microstructures, ASR-induced damage rates and distributions, which were not independently quantified by destructive techniques. However, these measured β results clearly show the SHG measurement is capable of monitoring the evolution of microcracking development and microstructure modification in large-scale concrete components with high accuracy.

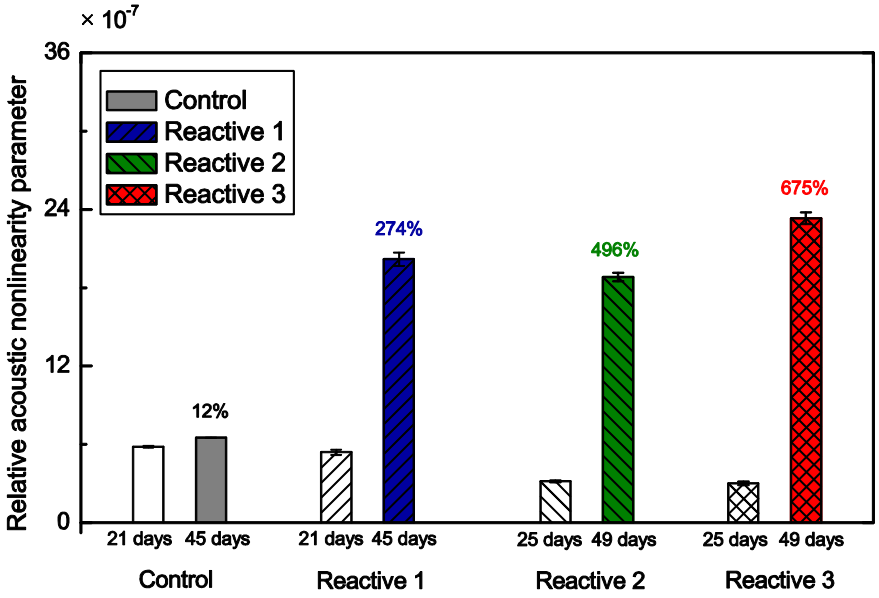

Figure. 7.12. Measured acoustic nonlinearity parameter, β.

Table 7.3 Summary of the measured linear and nonlinear acoustic parameters.

Sample	Age (days)	β	Change (%)	R^2	Rayleigh wave velocity (m/s)	Change (%)	Expansion (%)
Control	21	5.83×10^{-7} ($\pm$ 6.58×10^{-9})	12	98	2,479 ($\pm$ 80)	1	-0.009
	45	6.51×10^{-7} ($\pm$ 1.28×10^{-9})		99	2,452 ($\pm$ 35)		-0.007
Reactive 1	21	5.40×10^{-7} ($\pm$ 2.02×10^{-8})	274	99	2,555 ($\pm$ 45)	21	0.000
	45	20.19×10^{-7} ($\pm$ 5.13×10^{-8})		98	2,014 ($\pm$ 70)		0.080
Reactive 2	25	3.16×10^{-7} ($\pm$ 7.07×10^{-9})	496	98	2,748 ($\pm$ 175)	27	0.005
	49	18.83×10^{-7} ($\pm$ 3.19×10^{-8})		99	2,017 ($\pm$ 135)		0.090
Reactive 3	25	3.01×10^{-7} ($\pm$ 1.27×10^{-8})	675	99	2,822 ($\pm$ 165)	34	0.001
	49	23.33×10^{-7} ($\pm$ 4.40×10^{-8})		96	1,866 ($\pm$ 200)		0.050

7.4.4 Evaluation of ASR Damage

With the objective of material characterization, the effect Alkali-Silica Reaction (ASR) damage on the microstructures is studied as a target of evaluation. Consequently, the significant increase in the acoustic nonlinearity parameter is observed due to the ASR-induced microstructural behavior. Most importantly, the sensitivity of the nonlinearity parameter to the ASR-induced damage is far greater than that of any conventional parameters used for ASR characterization. Some suggestions are made concerning the ASR characterization: (1) it can be expected that there are some effects of drying shrinkage or aging on the microstructure during the ASR damage process (as concrete age) thus, more precise characterization can be possible if the characterization of those effects is compensated, and (2) in contrast to the previous works (Chapter 4,5, and 6), there might be the effect of attenuation due to the measurement variation from different locations (the university of Alabama and EPRI), so the attenuation corrections will give more reliable information on the ASR damage.

7.5 Summary and Conclusions

This chapter demonstrates the feasibility of using the SHG of nonlinear Rayleigh surface waves to assess the damage state in large-scale concrete slabs experiencing ASR. The experimental results show that the approach using a wedge transducer (48 kHz) for generation and a non-contact, air-coupled ultrasonic receiver (96 kHz) is capable of accurately measuring the acoustic nonlinearity parameter, β in large-scale concrete slabs, demonstrating that the proposed SHG technique is equally effective in monitoring

microscale damage in both laboratory- and large-scale specimens. The measured β increases significantly in the reactive concrete slabs before and after the initiation of ASR-induced damage, where the sensitivity of β to this damage is an order of magnitude greater than the expansion and Rayleigh wave velocity.

These proof-of-principle SHG measurements in large-scale slabs demonstrate the potential for the in situ, localized microscale damage characterization in full-scale concrete structures. This is a local measurement that requires access to a relatively small area on the specimen surface (about 20 cm), so it can potentially evaluate damage at localized spots even in concrete under constrained conditions. Furthermore, by lowering the fundamental frequency of the Rayleigh waves, the SHG technique is capable of increasing the penetration depth of the waves; this would permit interrogation of the condition of concrete structures to a greater depth.

CHAPTER 8. DEVELOPMENT OF IN SITU NONLINEAR NDE TECHNIQUE

8.1 Overview

Conventional NDE methods such as acoustic emission [177,178], acoustoelasticity [179,180], coda wave interferometry [181,182] have been implemented to assess the damage state in concrete under compression, and provided the quantitative information on the structural health condition in concrete. Nevertheless, in spite of those results, application of NDE technique to in situ interrogation is still considered as extremely challenging topic. In addition, most of application to load-carrying specimen is based on linear ultrasound [180,183]. This is mainly due to the difficulty in implementing the NLU or NLA measurements while the concrete specimen undergoes compression. Furthermore, the fact that cylindrical concrete specimen has been mostly used for compression test substantially limits the feasibility of existing nonlinear techniques – it is essential to design new experimental setup capable of detecting damage in cylindrical concrete.

With an aim of in situ interrogation of creep, this research designs new experimental approach based on the SHG techniques. The feasibility of the proposed setup for concrete cylinder is first validated by measure of the acoustic nonlinearity parameter, β, then implemented to characterize the progressive damage by creep and cyclic loading respectively.

8.2 Sample Preparation and Standard Strength Test

Sample preparation

Six concrete cylinders with dimensions, 100 × 400 mm (4 × 16 inch), were prepared according to ASTM C150 and ACI 211.1 [165,166]; each specimen is used for compressive testing, the feasibility of the proposed SHG technique, creep with two different loading level, recovering effect in the elastic regime, and cyclic loading. After casting, the specimens were cured at environmental temperature for 1 day and moved to a fog room (100% of relative humidity (RH) and 23℃) for 28 days to promote the hydration process. Then, the hydrated specimens were located in the environmental chamber (80 ± 2% RH and 28℃) until the mass of each specimen became consistent. At this stage, specimens age was higher than 50 days. It was therefore expected that the substantial amount of the moisture contents in the pores around the surface had already dried out and thus that microcracking by drying shrinkage was occurred. Table 8.1 shows the mixture proportions of the concrete specimens.

Table 8.1 Mixture design of concrete specimen, kg/m^3 (lb/yd^3).

	Concrete
Water	271 (365)
Cement (ASTM C150 Type I)	361 (608)
Water-to-cement ratio (w/c)	0.60
Coarse Aggregate	872 (1,470)
Fine Aggregate	784 (1,322)

Standard strength test

To understand the load-carry capacity of the prepared specimens, a uniaxial compression test was performed using one of the prepared specimens. A monotonically increasing compressive loading was applied along the longitudinal direction of the specimen by following ASTM C39/C39 M5 [175]. The 28-day hydrated concrete was placed in a compression frame and loaded up to the failure of the specimen. A dial gauge (Chicago Dial Indicator) and a linear variable differential transformer (LVDT) were attached on the surface to measure simultaneously the deformations due to the compression load (shortening). Both devices resulted in similar stress-strain curves when their values where plotted against the applied load (Figure 8.1). Specimen failure occurred at approximately 33.8 MPa (4,900 psi) with a break in the linear relationship between stress and strain when strain values were around 0.0007. It can be further interpreted that the microcracks initiated to coalesce from the strain beyond 0.007 while load-carry capacity of concrete is significantly reduced [161]. Therefore, it was expected that the microcracking would be substantially developed in the prepared specimens from the strain of 0.001. Based on the results of the single static compression test, this research determined that load would be applied until the strain is reached to around 0.001. The tracked stress level was 65 to 70% of the ultimate compressive strength. Table 8.2 shows the mechanical properties by the compression test.

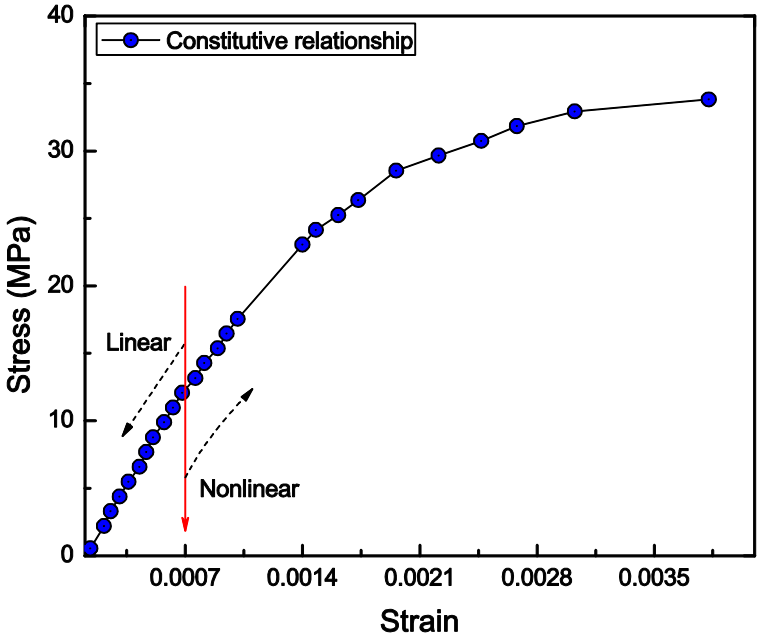

Figure 8.1. Stress-strain behavior for the prepared specimen.

Table 8.2 Data on uniaxial compression.

Cylinder geometry (diameter x height)	100 × 400 mm (4 × 16 inch)
Maximum load (F_{max})	27,941 kg (61,600 lb)
Compressive strength (f'_c)	33.8 MPa (4,900 psi)
Creep stress (68% of f'_c)	22.8 MPa (3,310 psi)
Cyclic stress (77% of f'_c)	26 MPa (3,780 psi)
Standards	ASTM C512, ACI 209, ASTM C39

Regarding the dimension of the specimen, it is important to note that the standard size (length-to-diameter ratio of 2) cannot provide a reliable SHG measurement due to the problem of the boundary-reflected waves. Therefore, it was required to determine new length-to-diameter ratio that enables the SHG measurements. First, based on the study by Jansen and Shah [184], it was confirmed that the fracture energy that affects the failure of

the concrete cylinder was not changed by the ratio (within the 2.0 and 5.5). Second, the calculation of the arrival time of the reflected waves from the back side has shown that the ratio of 4.0 allowed the propagation distance to be approximately 3.5 cm where there is no distortion of the propagated wave by the reflected waves. Based on them, the dimension of the concrete cylinder was determined to 100 × 400 mm (4 × 16 inch) in which both length effect (or buckling) and reflection effects could be ignorable.

8.3 Technical Approach and Experimental Setup

As shown in Figure 8.2, the feasibility of the designed in situ NLU setup for the prepared concrete cylinder is validated through the SHG measurement. Then, with the designed loading frame, monitoring of creep and cyclic loading is carried out in the isothermal environment by following the procedure of ASTM C512/C512M [185].

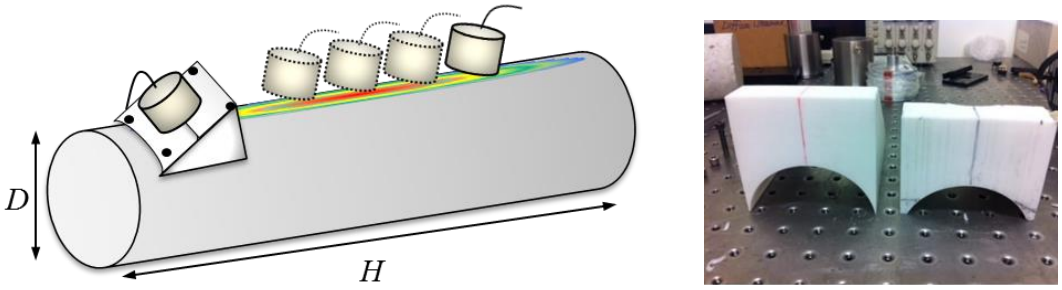

Figure 8.2. Design of a new wedge for cylindrical specimen.

8.3.1 Feasibility of SHG Technique for Application to Cylindrical Specimen

The procedure of the SHG measurement for the concrete cylinder is similar to that of previous research, with the exception that a new wedge design is required for the

concrete cylindrical specimens. Figure 8.3 shows the designed wedge and transmitter-wedge assembly. As shown in Fig. 8.3, the curvature of the wedge is identical to that of the specimen, and thus the new transmitter-wedge assembly can be tightly contacted with the concrete cylinder by acoustic couplant and elastic strings.

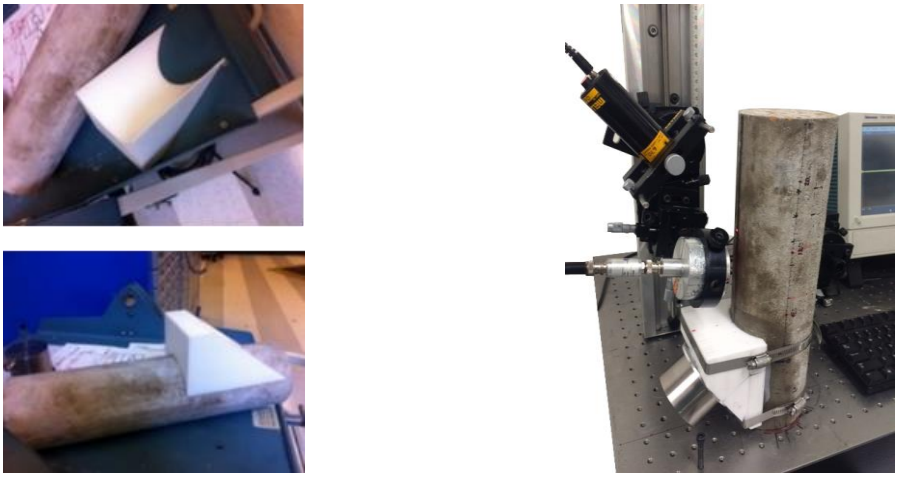

(a) New wedge for cylindrical specimen (b) Transmitter-wedge assembly

Figure 8.3. The SHG setup for cylindrical specimen.

As described in Chapter 4, the principle of the SHG measurements is based on Eq. (3.1). A narrow band piezoelectric transducer (approximately 40-60 kHz, Ultran GRD 50) is mounted to the designed Teflon wedge with acoustic couplant. The transmitter-wedge assembly is then attached to the specimen using acoustic couplant. A tone-burst signal of 10 cycles at 57 kHz is generated by a function generator (AGILENT 33250A) with a peak-to-peak voltage of 220 mV and is amplified up to 50 dB by a power amplifier (ENI Power Amplifier). A Rayleigh surface wave is generated and propagates along the surface of the concrete cylinder. A 100 kHz air-coupled transducer (Ultran GRD 100) is used to receive the propagating Rayleigh waves − the angle between the transducer and air is determined

to approximately 8˚. The detected signal is amplified up to 55 dB by a broadband preamplifier (Digital Wave Inc.) with the 256 times average and digitized with an oscilloscope (Tektronix TDS 5034B Digital). The entire system is synchronized by a trigger signal, and the recorded signal is transferred to a computer for signal processing.

The SHG measurement is first conducted in the context of the feasibility of the proposed setup. Figure 8.4 (a) and (b) show the results of the SHG measurements from the cylindrical specimens. Both the fundamental harmonic amplitude (A_1) and the second harmonic amplitude (A_2) are clearly seen in the frequency spectrum. Moreover, as shown in Fig. 8.4 (c), trends of A_1 and A_2 are well in accordance with the SHG theory; A_2 is monotonically increasing with the increasing propagation distance, while A_1 is decreasing. Thus, the ratio of A_2 to A_1^2 shows a linearly increasing trend with increasing propagation distance (Fig. 8.4 (d)). The coefficient of determination for the linear fit is higher than 99% for the repeated SHG measurements. Most importantly, these observations are not only good agreement with the results in Chapter 4 to 7 and but also enough to demonstrate the applicability of the proposed approach to concrete cylinder.

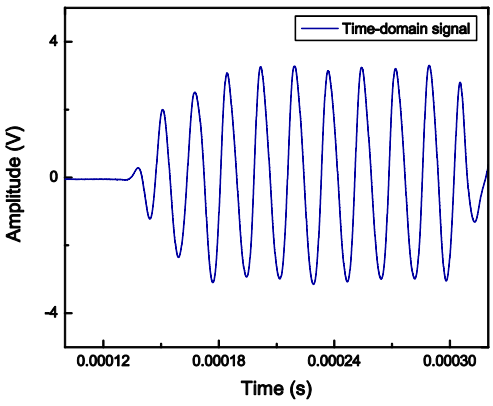

(a) Measured time-domain signal.

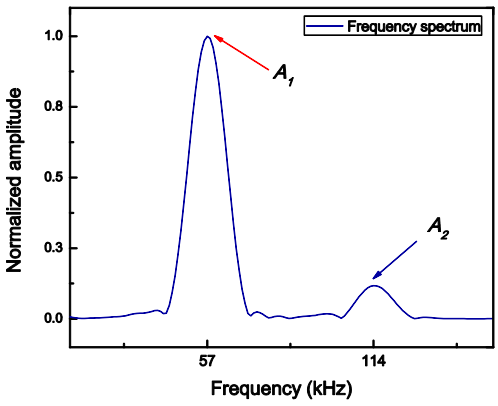

(b) Frequency spectrum using FFT.

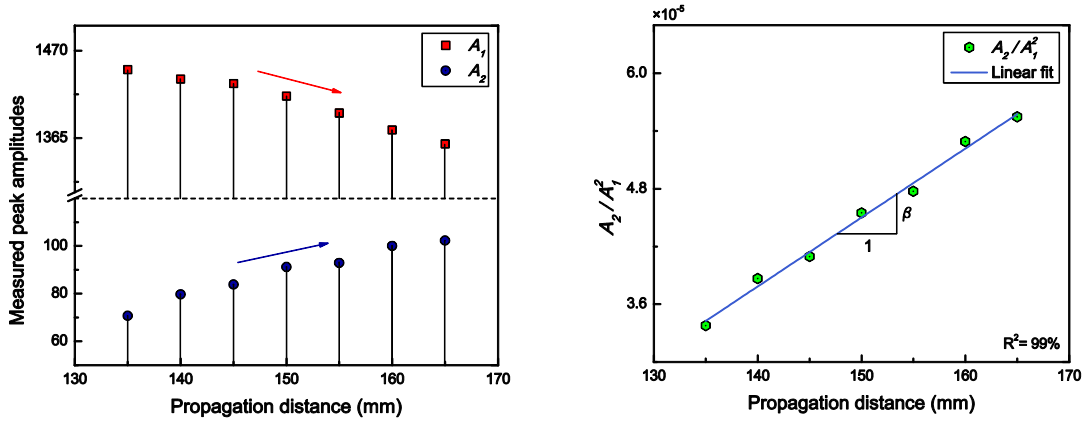

(c) Trend of A_1 and A_2 with the distance. (d) Acoustic nonlinearity parameter.

Figure 8.4. Procedure of the proposed SHG measurements for concrete cylinder.

Figure 8.5 shows the entire SHG setup for a concrete cylinder. For the evaluation of creep and cyclic loading, the specimen-wedge assembly is located vertically. A single linear stage is placed on a table to vary the propagation distance; the linear stage and the table are perpendicular each other. Also, an angular stage with the air coupled transducer is vertically attached to the linear stage. In this way, the surface area of the specimen becomes parallel to the bottom area of the air-coupled receiver when the angular stage indicates 0 degree. For the reliable interrogation of creep or cyclic loading, the alignment between the center of the receiver and the specimen-transmitter assembly is of importance. To do so, a laser device fixed to the linear stage is used to tack the alignment; the emitted beam from the laser indicates the centers of the loading frame, the transmitter-specimen assembly, and the receiver in sequence. The detailed procedure of the alignment is described in Figure 8.6.

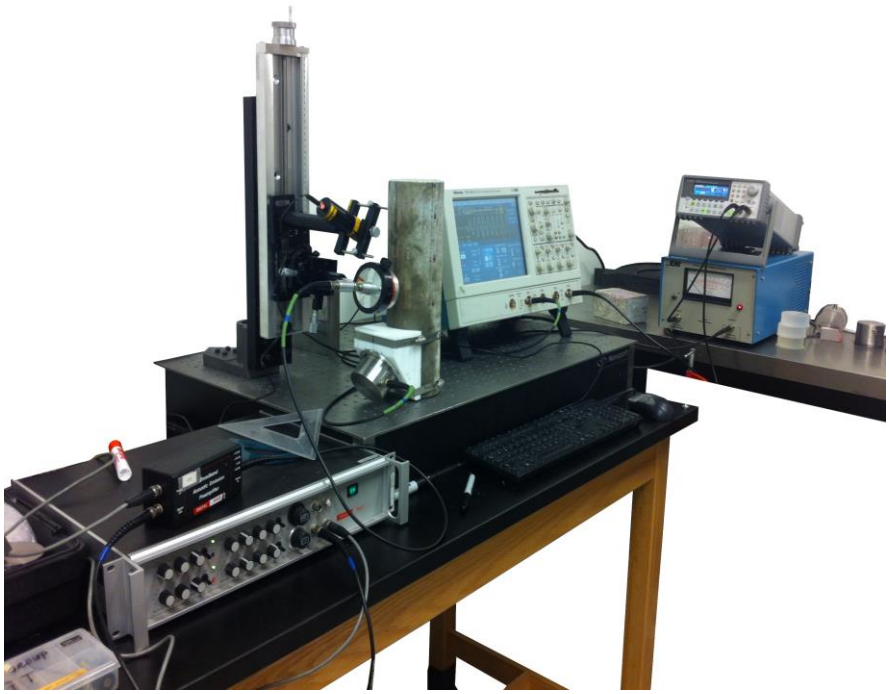

Figure 8.5. The entire SHG setup for concrete cylinder.

(a) Center of the frame. (b) Center of the specimen-transmitter assembly. (c) Center of the receiver.

Figure 8.6. Alignment of the transducers with the loading frame.

8.3.2 Design of Loading Frame

The loading frame is designed based on ASTM C512/C512M [185]. The loading frame consists of two header plates (top and bottom), two base plates (upper and lower), springs, and four threaded rods. Figure 8.7 (a) illustrates the test frame and the specimen equipped with the proposed SHG setup. As a hydraulic actuator located in the center of the base plate (lower) is operated, the uniaxial compression is transferred from the plates, to the springs, up to the specimen through the bearing plates. Once the applied load approaches its target value, the upper bearing plate gets in a contact with the top header plate through an elastic steel ball. The upper part of the header and the base plates become tightly fixed to the threaded rods by four-piece nuts. In this configuration, the entire loading frame can hold a constant load while testing and thus the specimens is subjected to creep damage. The hydraulic actuator is controlled by means of a hand pump (Enerpac and a load cell helps to monitor the load during test.). A portable strain indicator (P-3500, Vishay Instruments) connected to the load cell converts the measured voltage into force magnitude. As shown in Fig. 8.8, calibration tests were performed to ensure that the calibration curve of voltage versus load was on a perfect linear fashion. Induced strain on the specimens was also monitored using a dial gauge with a tolerance of 0.002 mm. Two set points on the specimen surface (approximately 255 mm apart) is prepared to read the changes in length and to obtain the experimental stress-strain curve.

To align the entire in situ monitoring system, every part of the frame is set to be parallel to the ground and the longitudinal direction of the specimen is aligned to be perpendicular to those pieces. This procedure prevents the possibility of eccentric load or buckling effect due to the misalignment. Note that the direction of the wave propagation

coincides with the loading direction. Figure 8.7 (b) shows a photo of the SHG setup placed in the measurement.

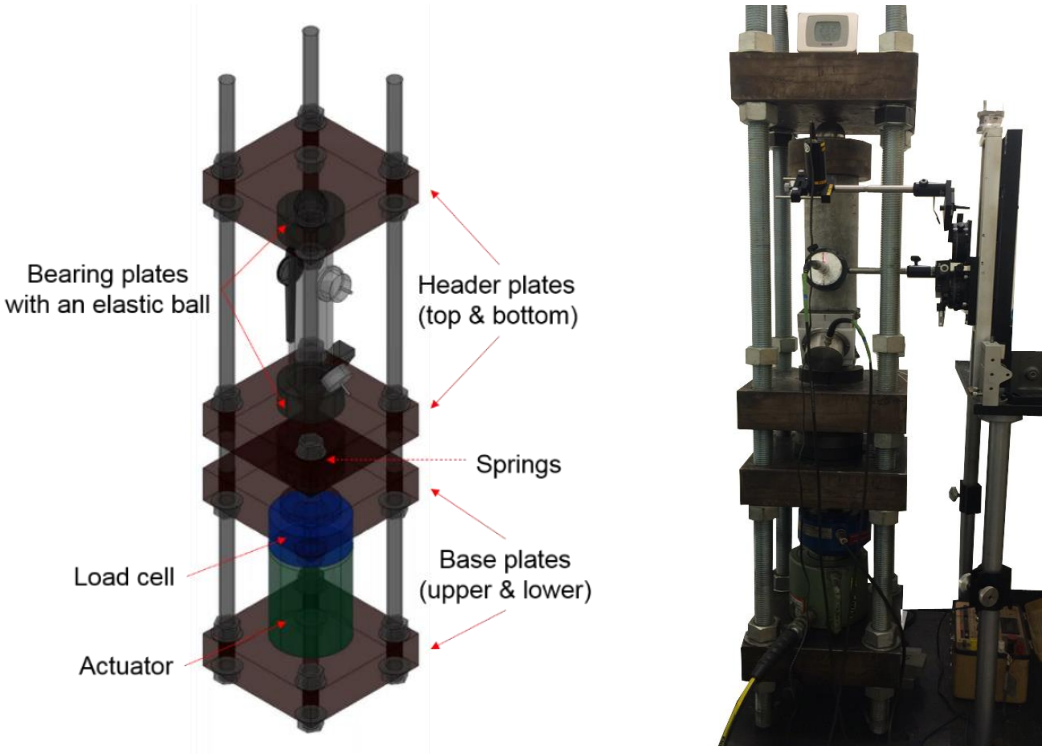

(a) designed loading frame. (b) Photo of the in-situ SHG setup.

Figure 8.7. In situ SHG setup with the loading frame.

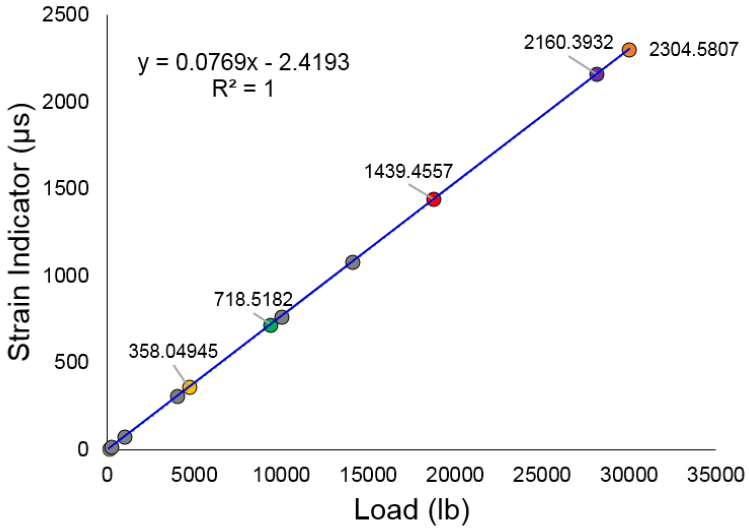

Figure 8.8. Calibration curve (load vs voltage).

8.4 NDE of Concrete Cylinder Subjected to Creep and Cyclic Loading

Monitoring of microcracking development by creep and cyclic loading is performed in the controlled room. Temperature and RH were constantly monitored during test and their values kept constant to be approximately 24 °C and 20%, respectively.

8.4.1 Creep

In situ monitoring of creep is performed for 603 hours (25 days) using the concrete cylinder subjected to the uniaxial compressive stress of 68% of the ultimate strength. As described earlier, it is anticipated that the internal microcrack development will be well distributed in the monitoring area since the applied load is enough to raise the strain more than 0.001. Figure 8.9 presents the planned loading and unloading protocol. Once the strain reaches to the target value (≈ 0.001 at 68%), the position of the specimen is fixed to keep the consistent load and to initiate the creep process. Note that up to 68%, the load is applied with a consistent rate.

Strain

Figure 8.10 shows the monitored strain during the loading process. At the beginning, the strain increases instantaneously. Once the creep process has initiated, the strain keeps increasing continuously (primary stage) however, after 4 hours (beyond the primary stage), the increasing rate significantly reduces (secondary stage). The results show a maximum change of 8% during the secondary stage. Figure 8.11 shows the recorded strain versus time for 603 hours of creep. The obtained creep curve is well

corresponding to the typical creep curve for concrete [92]. Moreover, once the load is unloaded, the value of the strain immediately drops and the result shows the distinguishable recovery trend: a considerable portion (65%) of the strain is irrecoverable (irreversible creep) and the creep recovery (~ 1%) is also observed. Although the result of the strain is reasonable for describing the creep behavior however, the magnitudes of the developed strain between the primary and secondary stages are still too ambiguous to explain the internal microstructural development during this measurement period − this is probably due to the low sensitivity of the strain to microcracking development by creep.

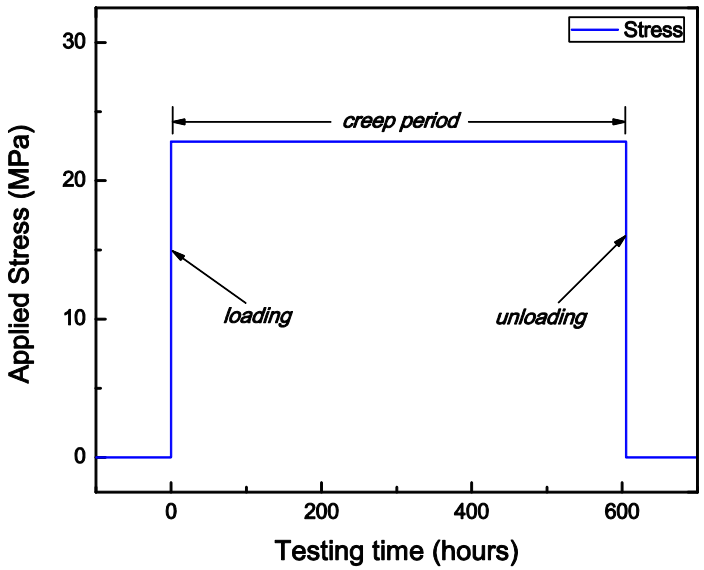

Figure 8.9. Loading protocol.

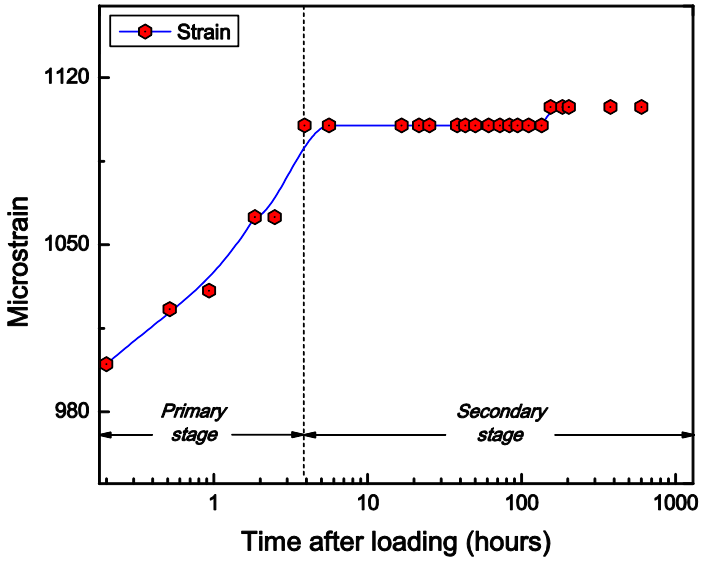

Figure 8.10. Strain-time curve (Primary vs Secondary).

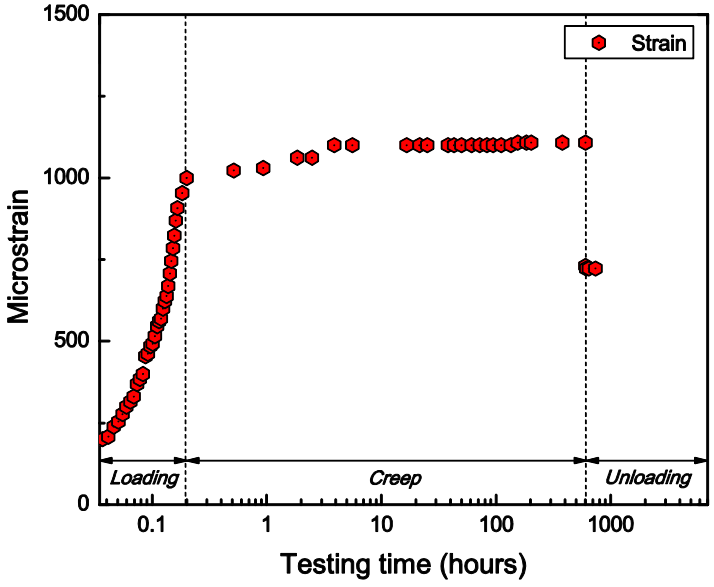

Figure 8.11. Creep curve (strain).

Acoustic nonlinearity parameter, β

The SHG measurement is performed in a quantitative fashion during the same monitoring period. Note that the both measured A_1, and A_2 show decreasing and increasing trends, respectively, with increasing propagation distance with a R^2 for the linear fit higher than 96% for all SHG measurements. Also, the SHG measurement is repeated only twice for each time period in order to avoid the creep effect during averaging time of the SHG measurements. Figure 8.12 shows the measured acoustic nonlinearity parameter, β for 603 hours of creep process. Unlike the strain measurement, the acoustic nonlinearity parameter exponentially increases up to approximately 60 hours (from 7.58×10^{-7} to 1.90×10^{-6}) and shows a consistent trend, meaning that the secondary stage is appeared after 60 hours. This high increase can be attributed to the manifestation of the crack growth due to the C-S-H break, plasticity, and crack initiation/propagation around ITZ. Furthermore, since the acoustic nonlinearity parameter includes those microscopic damage features, the result shows the delay of the secondary stage (approximately 60 hours) as compared to the strain measurement (approximately 4 hours). Note that the maximum value of the acoustic nonlinearity parameter is 2.11×10^{-6} at 184 hours.

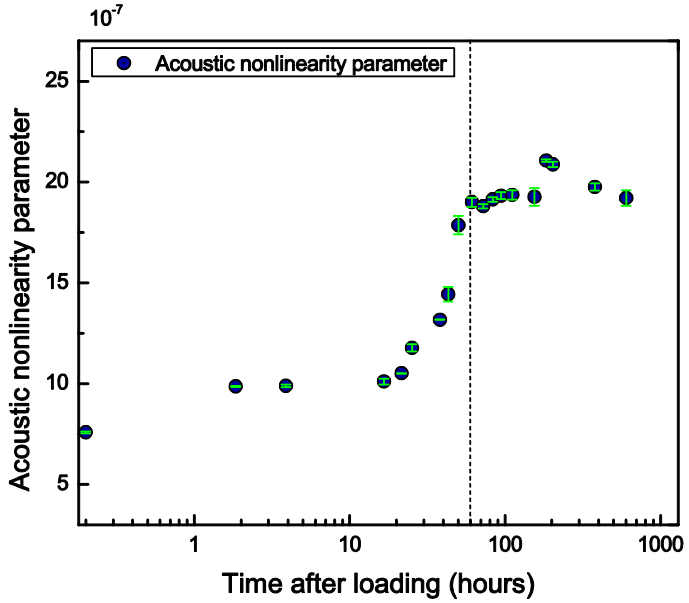

Figure 8.12. Damage by creep (acoustic nonlinearity parameter, β).

Compaction vs Creep

Complementary SHG measurements track the microcracking development by using 30% of the ultimate strength. Figure 8.13 clearly shows the microstructural distribution associated with the loading level. At 30% of the ultimate strength as green triangle indicated, the SHG result shows that the trend of the acoustic nonlinearity parameter is not increased by the sustained loading, while β is monotonically developed at 68% of the ultimate strength. This result can be explained by the fact that the compaction effect (or acoustoelastic effect) on the distribution of the microstructure is more dominant than creep; the intrinsic material nonlinearity including pre-existing microcracks can be closed due to a low level compression (30%). From those observations, it is confirmed that the applied

load should be enough to exceed the threshold (0.001 of strain) of the compression-induced crack closing.

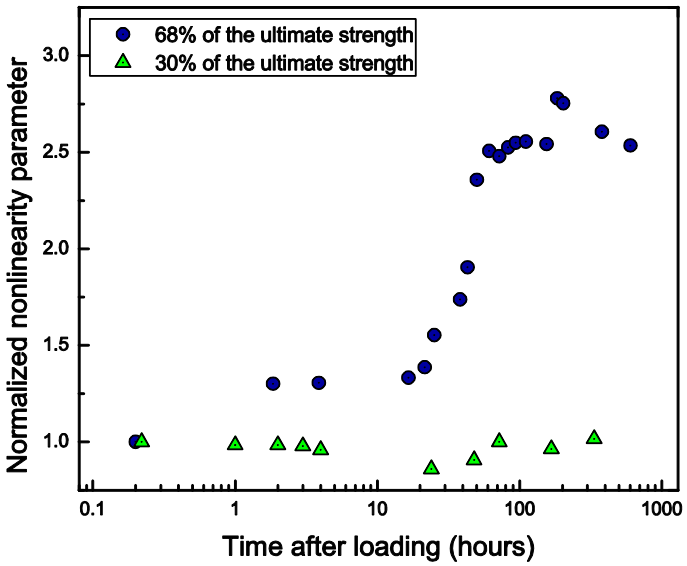

Figure 8.13. Compaction effect vs creep effect.

Sensitivity study

In the context of the sensitivity to the microcracking development under creep, both measured acoustic nonlinearity parameter, β and strain are normalized and plotted together. As shown in Figure 8.14, while the strain increases by 11%, the acoustic nonlinearity parameter shows a maximum of 178% increase, meaning that the sensitivity of the acoustic nonlinearity parameter is much higher than that of the strain by a factor of 18.

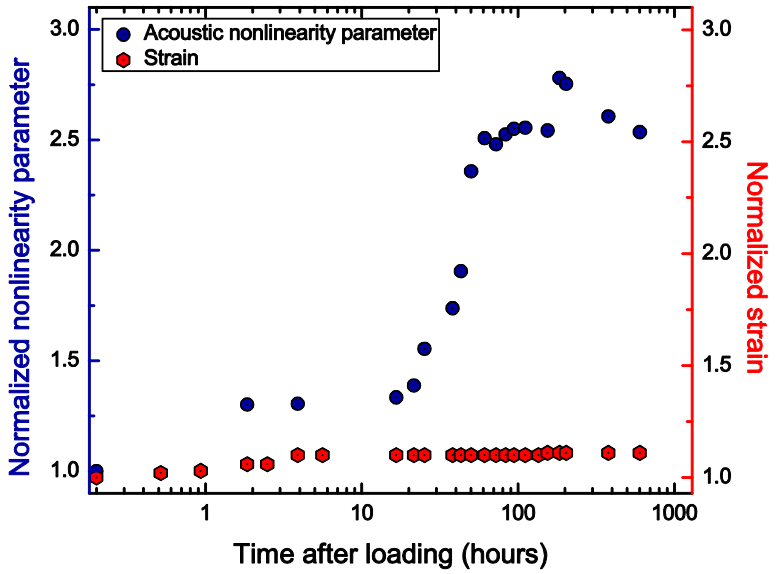

Figure 8.14. Sensitivity to creep damage (β vs strain).

8.4.2 Cyclic Loading

Another goal of this paper is to understand the microcracking development under cyclic loading. Specifically, this paper aims to investigate an evidence of how many cycle is required to develop the same degree of the microcracking growth by creep in the same monitoring zone. To investigate this, the uniaxial compressive cyclic loading test is performed using another specimen. Note that this test is referred to a quasi-static compression test. Figure 8.15 describes the procedure of the cyclic loading test. The prepared specimen is subjected to the cycle loading with the 77% of the ultimate strength. Note that the average time for loading and unloading is approximately 13, and 7 minutes respectively and the attached dial gauge reads the longitudinal deformation. Figure 8.16 shows an example of the obtained stress-strain curve for 3rd, 6th, and 10th cycle.

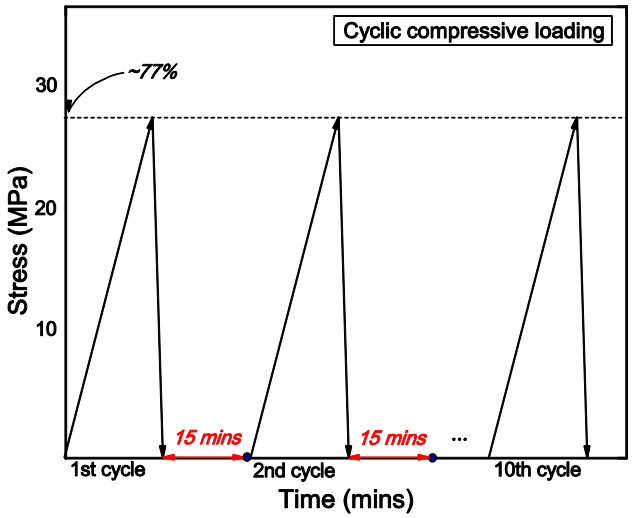

Figure 8.15. Loading protocol.

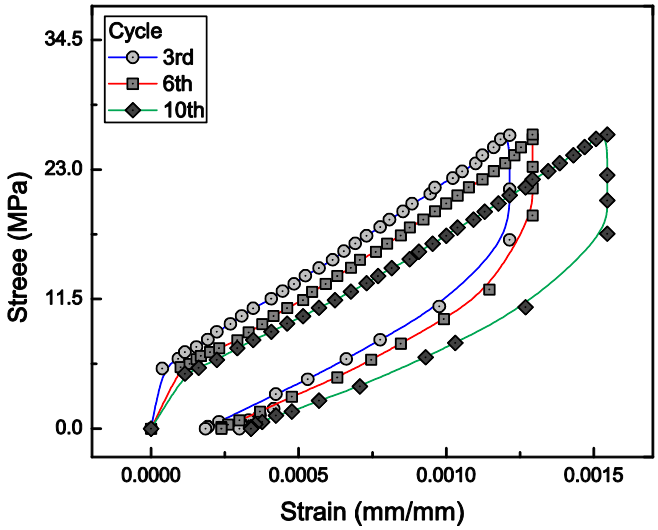

Figure 8.16. Stress-strain curve.

Elastic recovery

When the applied stress is removed, the microstructures in a brittle material like concrete will not be immediately stable; the rate of the stabilization takes some times to be

recovered, depending on both the magnitude of the applied load and the nature of the intrinsic microstructure. This mechanical phenomenon can be referred to "elastic recovery". Note that the mechanism of elastic recovery (quasi-static) is not the same as slow dynamics (dynamic), although their effect on the microstructure is fairly analogous. Therefore, to isolate this recovering effect during the assessment of cyclic loading, this research monitors the transient (time-dependent) microstructural behavior after unloading by tracking the trend of the fundamental harmonic amplitude, A_1 with time. As shown in Fig. 8.17, the experimental results clearly show that the measured A_1 is monotonically increasing for approximately 15 minutes after unloading. This increasing A_1 indicates that the changed microstructures continue to recover until they become stabilized. After that, A_1 tends to be consistent. Based on this, it can be stated that the recovering effect in the elastic regime will be substantially eliminated after 15 minutes for 77% of the ultimate strength. In addition, it can be further interpreted that the material properties like Young's modulus of load-carrying concrete can be healed within this period.

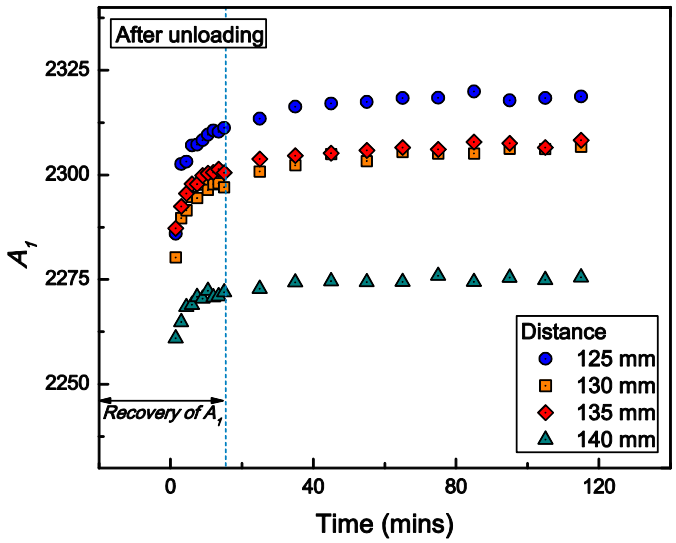

Figure 8.17. Monitoring of microstructural recovery using A_1.

Cyclic loading

Based on Fig. 8.15 and 8.17, the cyclic loading is applied to the concrete cylinder. The SHG measurement is only performed after 15 minutes. Figure 8.18 shows the measured acoustic nonlinearity parameter. With increasing number of cycles, the acoustic nonlinearity parameter increases monotonically.

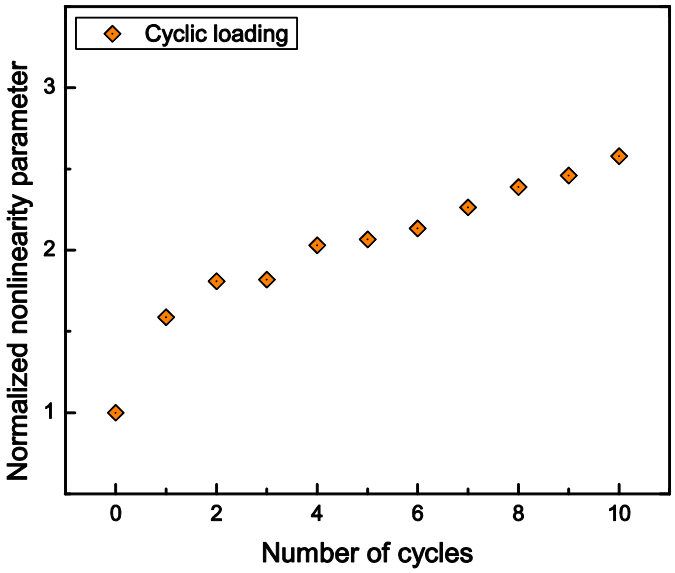

Figure 8.18. Damage by cyclic loading (acoustic nonlinearity parameter, β).

Creep vs Cyclic loading

And after 10 cycles, the results show that the increase in the acoustic nonlinearity parameter is reached to 158% − this increase is corresponding to the 154 % increase after 603 hours in the creep test. That is, both the sustained loading for 603 hours and the cyclic loading for the number of 10 cycles eventually result in the same amount of microcracking

development. Figure 8.19 shows the overall comparison of creep test (68%, 603) hours with cyclic loading test (77%, 10 cycles).

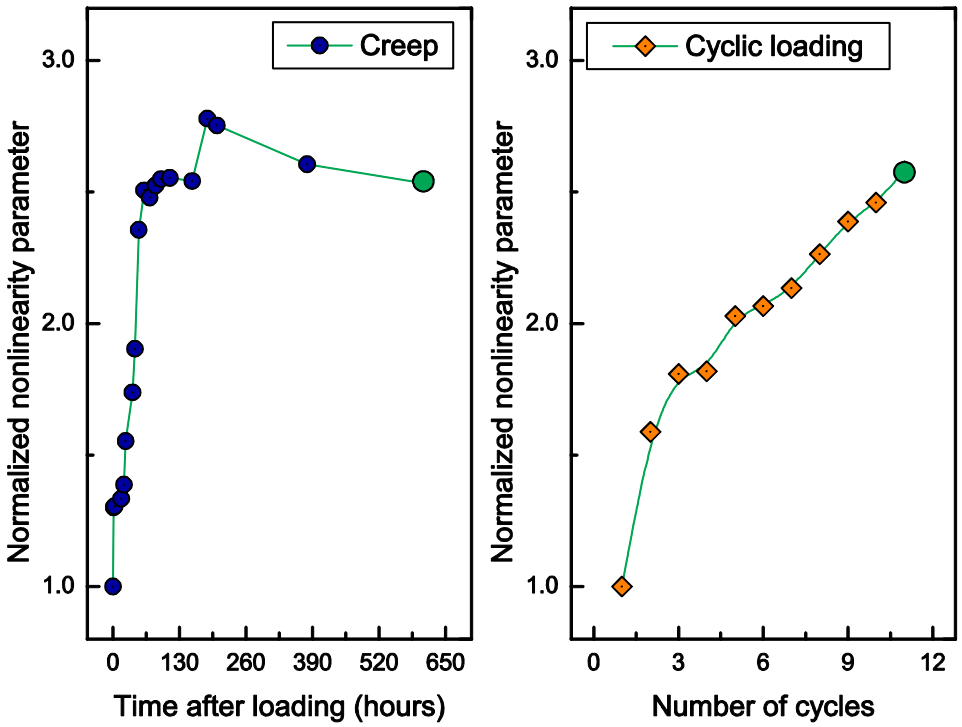

Figure 8.19. Microcracking development: creep (68%, 603 hours) vs cyclic loading (77%, 10 cycles).

8.5 Summary and Conclusions

Chapter 8 demonstrates the feasibility of the designed in-situ SHG technique using the Rayleigh surface waves for the assessment of the condition of concrete. Two experimental investigations concerning the effect of the creep and cyclic loading on

internal microcrack propagation are carried out independently. The following conclusions are drawn from these experimental results:

- The designed new wedge-type, and SHG setup enable the measurement of the acoustic nonlinearity parameter, β from the concrete cylinder − trends of the measured fundamental and second harmonic amplitudes are in good agreement with the theory of SHG.
- The ratio of length to diameter (= 4.0) resolves two issues; (1) distortion by the finite size of the specimen, and (2) buckling effects. The SHG setup for concrete cylinder has great potential for NDE application since it can effectively resolve the size limitation of the rectangular concrete specimen. For instance, the rectangular specimen is fairly limited to fit in the environmental chamber while the concrete cylinder with a geometry (4 × 16) can be easily fitted in any chambers.
- For the stress development, it is monitored that the stress-strain curve shows a distinguishable nonlinear fashion when the strain indicates the value over 0.001.
- It is important to note that the acoustic nonlinearity parameter, β is monotonically increased by creep (68%) while it shows no changes for 30% of the ultimate strength.
- For the evaluation of creep, although the strain is almost consistent in the secondary stage, however, β shows a remarkably increasing trend during the same period. This clearly reveals that the microcracking is still developing in the secondary stage.
- For the sensitivity to the microcracking, it is confirmed that the acoustic nonlinearity parameter is increases by 154% while the strain shows only 11% increase during the monitoring period. This demonstrates that the acoustic

nonlinearity parameter is suitable damage parameter to monitor the early-stage microcracking development due to creep.

- Under cyclic load, the measured acoustic nonlinearity parameter is increased by 158%. Microcracking development by both creep (68%, 603 hours) and cyclic loading (77%, 11 cycles) has same degree of magnitude.

The major contribution of this research is attributed to the fact that the proposed SHG setup is capable of monitoring initial micro-scale damage development in the cylindrical specimen under uniaxial compression, which, in turn, can lead to an “in situ” NDE.

CHAPTER 9. CONCLUSIONS AND FUTURE OUTLOOK

This thesis developed a new technique for the application of second harmonic generation (SHG) in Rayleigh surface waves to nondestructively evaluate the early-stage damage in cement-based materials. After validation of the accuracy of the proposed SHG setup, the acoustic nonlinearity parameter, β is used to quantify a number of damage mechanisms including drying shrinkage, alkali-silica reaction (ASR), creep, and cyclic loading in small-scale specimens, large-scale slabs, and cylinders. In addition, the role of shrinkage-reducing admixture (SRA), and carbonation in healing existing microcracks is assessed. This chapter discusses the advantages of the SHG measurement with Rayleigh surface waves, with an overall understanding of early-stage material state, and future research.

9.1 Second Harmonic Generation in Rayleigh Surface Waves in Concrete

A SHG setup using 50 kHz wedge transmitter and a 100 kHz air-coupled receiver is developed for the generation and detection of nonlinear Rayleigh waves in concrete. Both transducers are assembled by a function generator, power amplifier, broadband preamplifier; the calculated SNR is higher than 50 dB. Extensive evidences from the experiments have shown that the proposed SHG setup is capable of sensing both the fundamental harmonic (ω_1) and second harmonic (ω_2) components of a propagating Rayleigh wave, thereby providing a reliable measure of the acoustic nonlinearity parameter, β in the frequency range from 40 to 120 kHz. Therefore, it has been validated

that the SHG setup is suitable to nondestructively quantify the damage state in concrete. The following is a summary of the experimental results.

9.1.1 Air-Coupled Detection of Nonlinear Rayleigh Surface Waves in Concrete

The experimental results obtained by a non-contact, air-coupled receiver has shown that the acoustic nonlinearity parameter, β is repeatable and consistent, compared to the results of the conventional wedge receiver. It has been demonstrated that the air-coupled receiver has the advantages of eliminating the inconsistencies associated with coupling, reducing the measurement time, and increasing the repeatability of the SHG measurements. In addition, the inconsistency from the surface roughness of the specimen is also less important in this air-coupled detection method. These features make possible both less human-intervention in inspections, plus the inspection of concrete structures with complex geometries. It is also validated that implementing Rayleigh surface waves facilitates the evaluation of damages in full-scale concrete structures: (1) Rayleigh waves only require access to one side of the specimen, (2) the energy of Rayleigh waves is concentrated near the surface, and (3) the unwanted system nonlinearity from the instrumentation is decreased or constant, while the material nonlinearity continuously increase with propagation distance.

9.1.2 Application to Large-Scale Concrete Slab

This thesis develops the SHG in nonlinear Rayleigh surface waves to assess the damage state in large-scale concrete slabs. The experimental results clearly show that the approach using a wedge transducer (50 kHz) for generation and a non-contact, air-coupled ultrasonic

receiver (100 kHz) is capable of measuring the acoustic nonlinearity parameter, β in the large-scale concrete slab, meaning that the SHG technique is equally effective for both the laboratory-scale and large-scale nondestructive evaluation. Therefore, it can be stated that the SHG setup using the Rayleigh surface waves can open up the assessment of in-service concrete structures, once the automatic (robot) positioning system is assembled.

9.1.3 In-Situ Interrogation of Concrete Subjected to Uniaxial Compression

In-Situ SHG setup is developed by using the designed wedge/air-coupled receiver system for cylinders. It has been shown that the designed setup allows for the in situ monitoring of load-induced damage in concrete. Moreover, this SHG setup enables the characterization of microcracking development in concrete cylinders due to creep and cyclic loading.

9.2 Implication of β on Damage State in Concrete

The acoustic nonlinearity parameter, β from the developed SHG setup is used to characterize the microstructure changes and crack development by physical and chemical phenomena in concrete.

9.2.1 Drying Shrinkage

In hardened concrete, the time-dependent microstructural changes due to drying shrinkage are monitored with the acoustic nonlinearity parameter, β. In a period from 28 to 55 days of age, it is shown that β increases by 218%, while the mass shows a maximum

decrease of 2.5%. From the view of sensitivity to microcracking, the 218 % increase in β supports that moisture loss results in the significant microcracking during this period, particularly near the surface.

9.2.2 Mitigation of Drying Shrinkage by Shrinkage-Reducing Admixture (SRA)

As a solution of mitigating drying shrinkage, the effect of shrinkage-reducing admixture (SRA) is quantified by the measure of β. It is of particular interest to point out that a 3.4% dosage of SRA results in the decrease in β by 27% for concrete, and 36% for mortar. The aggregate restraining effect [89] supports the high decrease of β in mortar. It is worthwhile to note that the SRA plays a crucial role in reducing microcracks by moisture loss and thus enhancing the material state in concrete. It is likely that the 218% increase in β due to drying shrinkage in concrete at 55 days of age can be reduced 191% by the addition of SRA.

9.2.3 Carbonation

The investigation of the accelerated carbonation process with a set of the carbonation depth measurements is accompanied by the SHG measurements. The experimental results over the 40-day period provide valuable insights into the role of carbonation. First, the tracked β shows 64.2% decrease. On the contrary, the measured Rayleigh wave velocity exhibits only 5.5% increase; the amount of decrease is even comparable to the measurement errors due to the lack of sensitivity. Nonetheless, both results well support that carbonation product, $CaCO_3$ enhances the stiffness of concrete.

Nevertheless, the 64.2% increase in β is attributed not only to the enhanced stiffness, but also to the formation of $CaCO_3$ which fills pre-existing microcracks. This can be directly linked to the fact that that concrete undergoes healing by carbonation. The increasing trend of β in terms of time is in good agreement with the numerical prediction model [112].

9.2.4 Alkali-Silica Reaction (ASR)

Although the quantitative evaluation of ASR damage was not in the scope of this research, the SHG measurements clearly show that the sensitivity of the acoustic nonlinearity parameter, β to the ASR-induced microcracking is far greater than those of the conventionally-used damage parameters such as expansion, and Rayleigh wave velocity. The maximum change in β (675%) explicitly shows that ASR is the most deleterious damage mechanisms among the mechanisms studied in this research.

9.2.5 Creep and Cyclic Loading

Microcracking development by creep and cyclic loading is quantitatively evaluated with in situ SHG setup in the isothermal environment. It has been experimentally validated that the measured β shows the monotonically increasing trends in both creep and cyclic loading test. This observation is mainly due to the rapidly developed microcracking. The main implication of the creep and cyclic loading test is that the developed β by the creep test for four weeks (with 68% of the ultimate strength) is almost similar to that by the cyclic loading test with 10 cycles (with 77% of the ultimate strength). This can be further

interpreted that both sustained loading (68% of the ultimate strength, four weeks) and cyclic loading (77% of the ultimate strength, 10 cycles) result in same magnitude of the microcracking development in concrete. Finally, it is worthwhile to point out that the increasing β with time by creep shows very similar trend with that by drying shrinkage [86,92].

9.2.6 Effect of Temperature and Relative Humidity (RH)

During the evaluation of drying shrinkage (Chapter 6), and creep (Chapter 8), it is found out that β could be affected by temperature and relative humidity (RH). Particularly, it is easily expected that such environmental effects on the porous medium like concrete would be much greater than metallic and composite materials. Therefore, this research has tried to characterize the environmental effect with the SHG setup, and it has been turned out that β is increased up to 3% by 1 °C increase in temperature. This points out that the fluctuation of microstructure in concrete by the temperature cannot be ignored. Further studies are needed to fully understand the environmental effect on microstructure, and β.

9.2.7 Summary of Nondestructive Evaluation of Material State in Concrete

With the reported literature [86,115,159,186,187], a comprehensive understanding of early-stage material state in hardened concrete is conducted by monitoring the acoustic nonlinearity parameter, β. This comparison is enable by the fact that the same mix design including the w/c of 0.60 is consistently used in each tasks [37,53,55,58]. Note that

unfortunately, the mix design for ASR monitoring is slightly different as compared to others. As shown in Fig. 9.1, it can be stated that the hydrated concrete (28 days of age) undergoes the significant moisture loss until 55 days of age (218% ↑ in β). However, this deterioration by drying shrinkage can be mitigated by both the dosage of 3.4% dosage of SRA (27% ↓ in β) and through the 40 days of carbonation process (64% ↓ in β). Note that the decreased β by carbonation is comparable to the β at 28 days of age. This is an obvious evidence that carbonation is the "self-healing" mechanism. When expansion reached to almost maximum level, the reactive slabs show the 274% (slab 1), 496% (slab 2), and 675% (slab 3) increases in β. Furthermore, the rapid and monotonic micracking development is observed by sustained (154% ↑ in β) and cyclic loading (158% ↑ in β) − same degree of microstructure modification is occurred by different loading mechanisms. It should be note that the classification of the damage state using β is insufficient to represent the exact damage state. Nonetheless, with a reliable predict model, the acoustic nonlinearity parameter, β can be used as a quantitative index for the current damage state, and for the remaining life prediction.

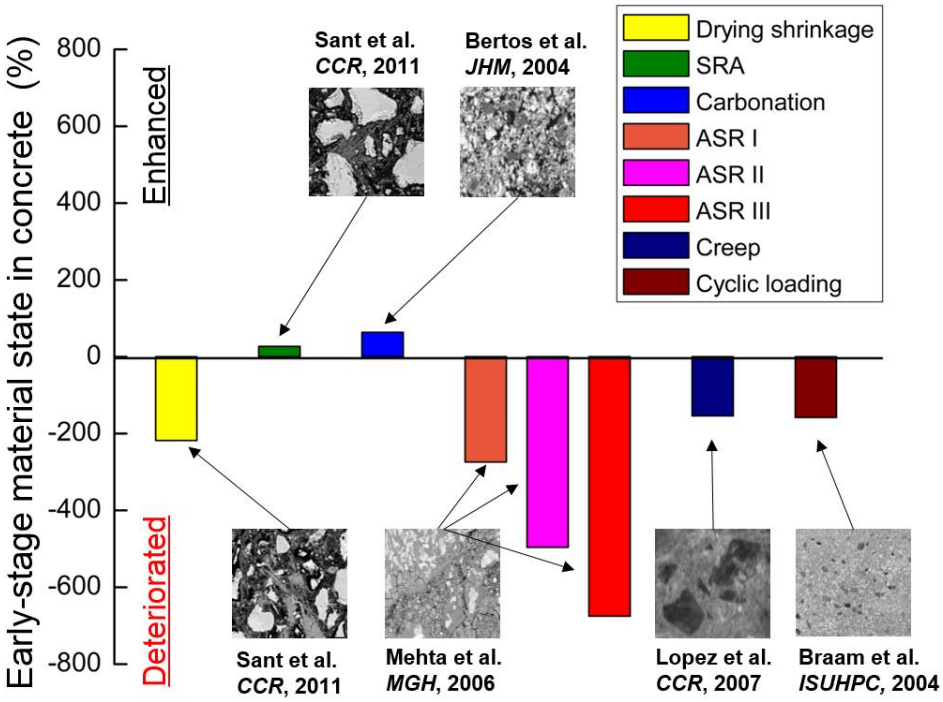

Figure 9.1. Classification of early-stage material state in concrete using the acoustic nonlinearity parameter, β.

9.3 Significance and Impact

This paper investigates the feasibility and reliability of second harmonic generation (SHG) technique to monitor the damage state in cement-based materials. Extensive evidence from the SHG measurements clearly demonstrates that the acoustic nonlinearity parameter, β is obtained in concrete by following the theory of SHG and successfully employed to quantify the early-stage damage level. Moreover, it has been shown that the sensitivity of β is one or two order of magnitude higher than those of any conventional

NDE parameters or material properties. Most importantly, further development of the SHG setup has facilitated *in situ* interrogation of concrete cylinder subjected to uniaxial compression, and inspection of large-scale concrete slab. Finally, as a candidate for new ultrasonic parameter, it has been well demonstrated that the proposed SHG setup is capable of providing the comprehensive information on the early-stage microcracking development in hardened concrete by tracking acoustic nonlinearity parameter, β.

9.4 Future Work

It is expected that the experimental evidence, and findings in this thesis can lead to field inspection and new strategy for a sustainable and resilient civil infrastructure. The following topics should be addressed in order to achieve these goals.

- *Robot-based scanning system for assessment of in-service concrete structures*: The key to achieving this objective is to incorporate Rayleigh surface waves in the scanning system. Once an autonomous, integrated scanning system is designed, then the SHG technique with the Rayleigh surface waves can be directly implemented to in-service concrete structures. Herein, the reliable condition assessment of in-service concrete structures will be realized.
- *Monitoring of early-age behaviors in concrete*: Precise understanding of early-stage microstructural condition should be followed with development of measurement technique. Based on the SHG results in this thesis, the acoustic nonlinearity parameter, β has great potential to quantify hydration process, and hardening process in concrete. By developing testing prototype, it is expected that

β can reveal a clear relationship between the development of material properties and microstructure formation in concrete at this age.

- *Absolute nonlinearity parameter*: Although the system nonlinearity is effectively isolated by using the Rayleigh surface waves, the sequestration of those effect is need to be characterized so that the acoustic nonlinearity parameter, β can be exploited as a real material property.
- *Modeling for prediction of remaining life of concrete*: Combining the SHG measurement with finite element method (FEM) analysis will provide a more reliable description of microstructure in concrete and enable the estimation of remaining life of concrete by the use of acoustic nonlinearity parameter, β.

APPENDIX A. DIFFRACTION AND ATTENUATION CORRECTIONS

For a highly damaged specimen, e.g., concrete undergoing the long-term process of ASR, it is recommended that the attenuation should be taken into consideration and compensated in the harmonic amplitudes. Also, both in the attenuation and second harmonic generation measurements, the diffraction effect (i.e. beam spreading effect) cannot be ignored. A diffraction model for the wedge transmitter and a line receiver is suggested by [50] and the model is modified for the wedge transmitter and an air-coupled receiver as follows:

$$D_R(\zeta)=\sqrt{\frac{s}{2\pi i}}\,\frac{1}{2}\int_{-1}^{1}\cos\left(\xi\frac{\pi}{2}\right)d\xi\int_{-1}^{1}\cos\left(\xi'\frac{\pi}{2}\right)\times\frac{e^{is\left(\sqrt{(\xi-\xi')^2+\zeta^2}-\zeta\right)}}{\sqrt[4]{(\xi-\xi')^2+\zeta^2}}\,d\xi'. \tag{A.1}$$

where, D_R is the diffraction function, α the radius of the transmitter, k the wave number, s (= αk) the normalized frequency, $\zeta = z/a$, $\xi = x/a$, and $\xi' = x'/a$. The obtained diffraction function is applied to Eq. (3.1) so that the attenuation coefficient (dB/m) can be calculated. The measured attenuation coefficients at 100 kHz for hardened concrete and mortar are given in Figure 4.13 and Table 4.2. Then, both fundamental and second harmonic amplitudes reflecting the attenuation and diffraction corrections are used to determine the acoustic nonlinearity parameter, β with the procedure of Shull et al. [188]. An example of the measured β accounting for attenuation corrections is described in Figure A.1. The corrected value of β shows approximately 10% increase for all cases. Nevertheless, as shown in Figure 7.11, the change in β by attenuation correction is much smaller than that by ASR damage (274%).

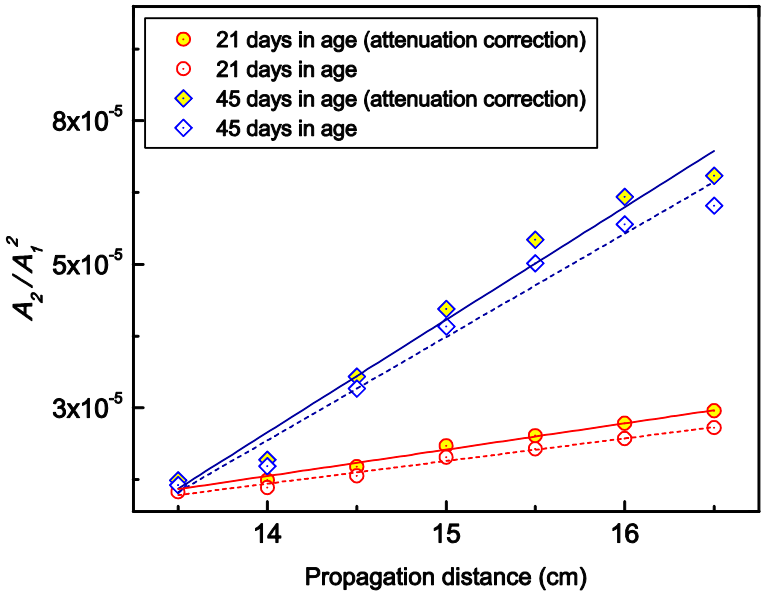

Figure A.1. The acoustic nonlinearity parameter with and without attenuation correction.

APPENDIX B. VISUALIZATION OF GENERATED HARMONICS (MATLAB)

```
%% VISUALIZATION OF GENERATED HARMONICS IN A SINUSOIDAL WAVE%%

%% 1. BASIC INFORMATION %%
kHz = 1e3;
MHz = 1e6;
ms = 1e-6;
f1=50*kHz;
f2=100*kHz;
T1=1/f1;
T2=1/f2;
f_s=3*MHz;
sample_dur=1000*ms;
time=[0:1/f_s:sample_dur];
time_length=length(time);

%% 2. TIME AND FREQUENCY %%
timevec=0:1/f_s:sample_dur;
time_real=0:1/f_s:3*sample_dur;
N  =length(time_real)
Nf = N/2;
dt = timevec(2) - timevec(1);
df = (1/(dt*N));
freqs = df*(0:N-1);
compoment=f1-f2

%% 3. FUNCTION INPUT %%
a1=zeros(1,length(time_real));
a2=zeros(1,length(time_real));
a1(1:length(timevec))=1*sin(2*pi*f1*timevec);
a2(1:length(timevec))=1*sin(2*pi*f2*timevec);

%% 4. THE SUM OF FUNDAMENTAL AND SECOND HARMONIC AMPLITUDE
%%
x_t=a1+a2;

%% 5. THE SQUARE OF THE SUM
n=2;
A2=(a1+a2).^n;
```

```
%% 6. FFT
FFT_a1=abs(fft(a1,N));              % FFT of function 1
FFT_a2=abs(fft(a2,N));              % FFT of function 2
FFT_x_t=abs(fft(x_t,N));            % FFT of linear sum
FFT_A2=abs(fft(A2,N));              % FFT of changed x_t

%% 7. PLOTS OF RESULTING FUNCTIONS %%
%
figure(1)
plot(time_real,a1,'r')
grid on
hold all
plot(time_real,a2,'b')
xlabel ('time')
ylabel ('amplitude')
title(['A1 and A2'])

figure(2)
subplot(311); plot(time_real,x_t);
xlabel('t (sec)')
ylabel('amplitude [%]');
title(['Time Signal'])

subplot(312)
plot(freqs./(1e3),FFT_x_t/max(FFT_x_t),'r')
axis([0 90 0 1.2])
xlabel ('frequency (kHz)')
ylabel ('amplitude [%]')
grid on
title(['FFT (Fundamental Hparmonic)'])

subplot(313)
plot(freqs./(1e3),FFT_A2/max(FFT_A2),'b')
axis([75 120 0 1.2])
xlabel ('frequency (kHz)')
ylabel ('amplitude [%]')
grid on
title(['FFT (Second Harmonic)'])
```

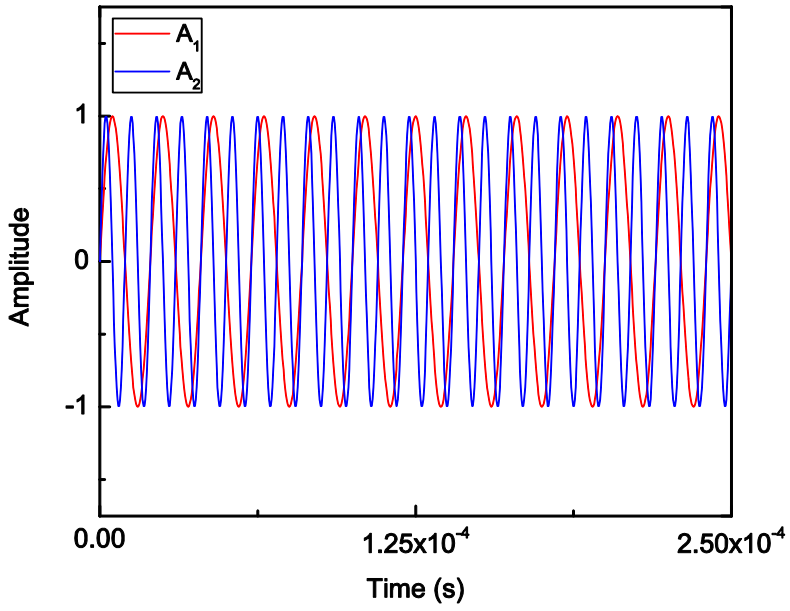

Figure B.1. Generated sinusoidal signals: fundamental (A_1), and second (A_2) harmonics.

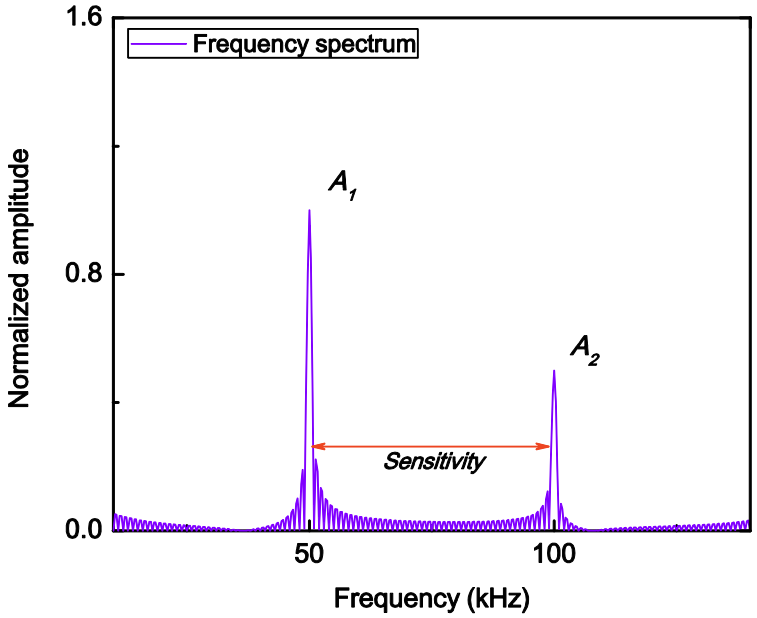

Figure B.2. Second harmonic generation (A_1 = 50 kHz, and A_2 = 100 kHz).

APPENDIX C. RAYLEIGH WAVE PROPERTIES FOR CONCRETE (MATLAB)

```
%% Rayleigh wave properties

format long

%% 1. User input
% frequency
    % concrete   5*10^4
f = 5.*10^4;
% Poison's ratio
    % concrete 0.2 - 0.21 => 0.21
nu = 0.21;
% Young's modulus (E)
    % concrete 30*10^9 N/m^2
E = 30*10^9;
% density
    % concrete          2200 kg/m^3
rho = 2200;

%% 2. Caluclation of parameters
lambda_lame = (E*nu)/((1+nu)*(1-2*nu)); %[N/m^2]
mu = E/(2*(1+nu));
% Longitudinal wave velocity
c_L = sqrt((lambda_lame+2*mu)/rho);     %[m/s]
% Transversal wave velocity
c_T = sqrt(mu/rho);                     %[m/s]
% Rayleigh wave velocity
c_R = ((0.862 + 1.14*nu)/(1 + nu))*c_T; %[m/s]
% angular frequency
omega_R = 2*pi*f;                       %[1/s]
% wavenumber
k_R = omega_R/c_R;                      %[1/m]
% wavelength
lambda_R = (2*pi)/k_R;                  %[m]
b_1 = k_R*sqrt(1-(c_R^2/c_L^2));
b_2 = k_R*sqrt(1-(c_R^2/c_T^2));
% displacements in propagation direction x_1 and normal to
surface of half space x_2
syms x_2
u_1 = exp(-b_1*x_2)-((2*b_1*b_2)/(k_R^2+b_2^2))*exp(-
b_2*x_2);
```

```
u_2 = abs(1i*(b_1/k_R)*(exp(-b_1*x_2)-
((2*k_R^2)/(k_R^2+b_2^2))*exp(-b_2*x_2)));
% displacements at x_2 = 0
u_10 = subs(u_1,'x_2',0);
u_20 = subs(u_2,'x_2',0);

%% 3. Output
disp('lambda_R [m] =');
disp(lambda_R);
disp('c_R [m/s] =');
disp(c_R);

figure(1);
set(gca,'FontName','Times','FontSize',16);
box on
hold on
a = ezplot(u_1/u_20,[0,4*lambda_R]);
set(a,'Color','r');
b = ezplot(u_2/u_20,[0,4*lambda_R]);
set(b,'Color','g');
hold off
axis([0 2.5*lambda_R -0.2 1.2]);
title('Normalized Displacements by Depth')
ylabel('Normalized Amplitude')
xlabel('depth (m)')
```

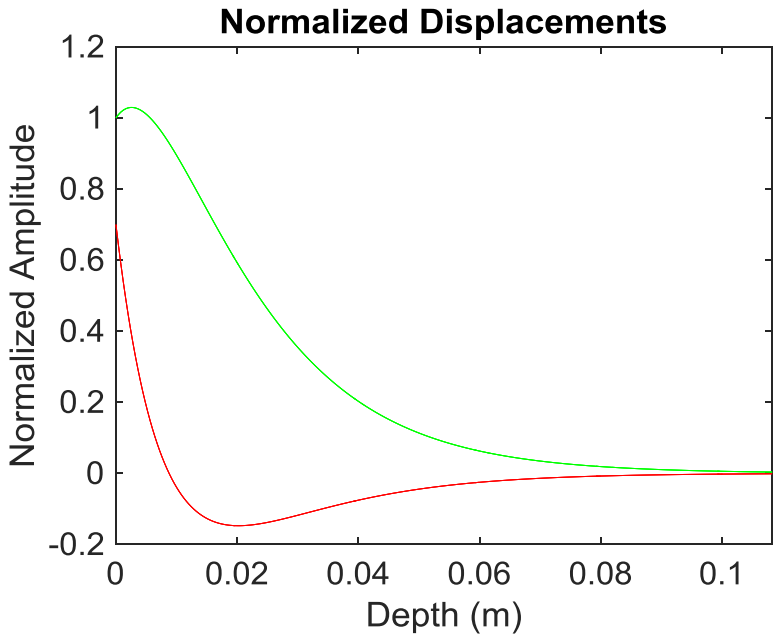

Figure C.1. Rayleigh wave properties (depth vs. amplitude).

REFERENCES

[1] C. Payan, V. Garnier, J. Moysan, P.A. Johnson, Determination of third order elastic constants in a complex solid applying coda wave interferometry, Appl. Phys. Lett. 94 (2009) 011904.

[2] J.N. Eiras, J. Monzó, J. Payá, T. Kundu, J.S. Popovics, Non-classical nonlinear feature extraction from standard resonance vibration data for damage detection, J. Acoust. Soc. Am. 135 (2014) EL82–EL87.

[3] C. Payan, T.J. Ulrich, P.Y. Le Bas, T. Saleh, M. Guimaraes, Quantitative linear and nonlinear resonance inspection techniques and analysis for material characterization: Application to concrete thermal damage., J. Acoust. Soc. Am. 136 (2014) 537–546.

[4] J. Chen, A.R. Jayapalan, J.Y. Kim, K.E. Kurtis, L.J. Jacobs, Rapid evaluation of alkali-silica reactivity of aggregates using a nonlinear resonance spectroscopy technique, Cem. Concr. Res. 40 (2010) 914–923.

[5] K.J. Leśnicki, J.-Y. Kim, K.E. Kurtis, L.J. Jacobs, Assessment of alkali–silica reaction damage through quantification of concrete nonlinearity, Mater. Struct. 46 (2013) 497–509.

[6] K.J. Leśnicki, J.-Y. Kim, K.E. Kurtis, L.J. Jacobs, Characterization of ASR damage in concrete using nonlinear impact resonance acoustic spectroscopy technique, NDT E Int. 44 (2011) 721–727.

[7] American Society of Civil Engineers (ASCE), 2013 Report card for America's infrastructure, http://www.infrastructurereportcard.org. (2013).

[8] S. Popovics, J.L. Rose, J.S. Popovics, The behaviour of ultrasonic pulses in concrete, Cem. Concr. Res. 20 (1990) 259–270.

[9] S.F. Selleck, E.N. Landis, M.L. Peterson, S.P. Shah, J.D. Achenbach, Ultrasonic investigation of concrete with distributed damage, ACI Mater. J. 95 (1998) 27–36.

[10] N.J. Carino, M. Sansalone, N.N. Hsu, A point source-point receiver, pulse-echo technique for flaw detection in concrete, ACI Mater. J. (1986) 199–208.

[11] J. Zhu, J.S. Popovics, Imaging concrete structures using air-coupled impact-echo, J. Eng. Mech. 133 (2007) 628–640.

[12] S.H. Kee, T. Oh, J.S. Popovics, R.W. Arndt, J. Zhu, Nondestructive bridge deck testing with air-coupled impact-echo and infrared thermography, ASCE J. Bridge Eng. 17 (2012) 928–939.

[13] R. Jones, Non destructive testing of concrete, University Press, 1962.

[14] ASTM C597-09, Standard test method for pulse velocity through concrete, Annual book of ASTM standards, (2009).

[15] G. Hevin, O. Abraham, H. Pcdersen, Characterisation of surface cracks with Rayleigh waves: a numerical model, NDT E Int. Sonderhcft. 31 (1998) 289–297.

[16] S.P. Shah, S. Chandra, Fracture of concrete subjected to cyclic and sustained loading, ACI Mater. J. 67 (1970) 816–827.

[17] V. Garnier, B. Piwakowski, O. Abraham, G. Villain, C. Payan, J.F. Chaix, Acoustic techniques for concrete evaluation: improvements, comparisons and consistency, Constr. Build. Mater. 43 (2013) 598–613.

[18] C. Payan, T.J. Ulrich, P.Y. Le Bas, M. Guimaraes, Quantitative linear and nonlinear resonant inspection techniques for characterizing thermal damage in concrete, Acoust. (2012).
[19] Y. Boukari, D. Bulteel, P. Rivard, N.E. Abriak, Combining nonlinear acoustics and physico-chemical analysis of aggregates to improve alkali-silica reaction monitoring, Cem. Concr. Res. 67 (2015) 44–51.
[20] T.J. Ulrich, P.A. Johnson, R.A. Guyer, Interaction dynamics of elastic waves with a complex nonlinear scatterer through the use of a time reversal mirror, Phys. Rev. Lett. 98 (2007) 104301.
[21] P. A Johnson, H. Savage, M. Knuth, J. Gomberg, C. Marone, Effects of acoustic waves on stick-slip in granular media and implications for earthquakes, Nature. 451 (2008) 57–60.
[22] P. A Johnson, X. Jia, Nonlinear dynamics, granular media and dynamic earthquake triggering, Nature. 437 (2005) 871–874.
[23] R. A. Guyer, P. A. Johnson, Nonlinear mesoscopic elasticity: Evidence for a new class of materials, Phys. Today. 52 (1999) 30–36.
[24] Z. Zhang, P.B. Nagy, W. Hassan, Analytical and numerical modeling of non-collinear shear wave mixing at an imperfect interface, Ultrasonics. 65 (2016) 165–176.
[25] J.H. Cantrell, Substructural organization, dislocation plasticity and harmonic generation in cyclically stressed wavy slip metals, Proc. R. Soc. A Math. Phys. Eng. Sci. 460 (2004) 757–780.
[26] V.E. Nazarov, A.M. Sutin, Nonlinear elastic constants of solids with cracks, J. Acoust. Soc. Am. 102 (1997) 3349–3354.
[27] J.-Y. Kim, J.-S. Lee, A micromechanical model for nonlinear acoustic properties of interfaces between solids, J. Appl. Phys. 101 (2007) 043501.
[28] P. Antonaci, C.L.E. Bruno, P.G. Bocca, M. Scalerandi, A.S. Gliozzi, Nonlinear ultrasonic evaluation of load effects on discontinuities in concrete, Cem. Concr. Res. 40 (2010) 340–346.
[29] C. Payan, V. Garnier, J. Moysan, P. A Johnson, Applying nonlinear resonant ultrasound spectroscopy to improving thermal damage assessment in concrete, J. Acoust. Soc. Am. 121 (2007) EL125–EL130.
[30] M. Scalerandi, M. Griffa, P. Antonaci, M. Wyrzykowski, P. Lura, Nonlinear elastic response of thermally damaged consolidated granular media, J. Appl. Phys. 113 (2013) 154902.
[31] L.E. Malvern, Introduction to the Mechanics of a Continuous Medium, Prentice-Hall, Inc., 1969.
[32] J.D. Achenbach, Wave Propagation in Elastic Solids, Elsevier B.V., 1973.
[33] Viktorov, Rayleigh and Lamb waves: physical theory and applications, Plenum Press (1967).
[34] Y. Lin, W.C. Su, Use of stress waves for determining the depth of surface-opening cracks in concrete structures, ACI Mater. J. 93 (1996) 464–505.
[35] M. Sansalone, J.M. Lin, W.B. Streett, Determining the depth of surface-opening cracks using impact-generated stress waves and time-of-flight techniques, ACI Mater. J. 95 (1998).
[36] C.-W. In, Defect characterization in heterogeneous civil materials using ultrasound,

Diss, Georgia Institute of Technology (2013).
[37] G. Kim, C.-W. In, J.-Y. Kim, K.E. Kurtis, L.J. Jacobs, Air-coupled detection of nonlinear Rayleigh surface waves in concrete–application to microcracking detection, NDT E Int. 67 (2014) 64–70.
[38] J.S. Popovics, J.L. Rose, Survey of developments in ultrasonic NDE of concrete, IEEE Trans. Ultrason. Ferroelectr. Freq. Control. 41 (1994) 140–143.
[39] K. Hoegh, L. Khazanovich, Extended synthetic aperture focusing technique for ultrasonic imaging of concrete, NDT E Int. 74 (2015) 33–42.
[40] F. Rajabipour, E. Giannini, C. Dunant, J.H. Ideker, M.D.A. Thomas, Alkali–silica reaction: Current understanding of the reaction mechanisms and the knowledge gaps, Cem. Concr. Res. 76 (2015) 130–146.
[41] A. V. Saetta, R. V. Vitaliani, Experimental investigation and numerical modeling of carbonation process in reinforced concrete structures: Part I: Theoretical formulation, Cem. Concr. Res. 34 (2004) 571–579.
[42] P.J.M. Monteiro, K.E. Kurtis, Time to failure for concrete exposed to severe sulfate attack, Cem. Concr. Res. 33 (2003) 987–993.
[43] J. Zhu, J.S. Popovics, F. Schubert, Leaky Rayleigh and Scholte waves at the fluid–solid interface subjected to transient point loading, J. Acoust. Soc. Am. 116 (2004) 2101–2110.
[44] J.S. Popovics, W.J. Song, M. Ghandehari, K. V. Subramaniam, J.D. Achenbach, S.P. Shah, Application of surface wave transmission measurements for crack depth determination in concrete, ACI Struct. J. 97 (2000) 127–135.
[45] J.S. Popovics, N. Ryden, A. Gibson, S. Alzate, I.L. Al-Qadi, New developments in NDE methods for pavements, AIP Conf. Proc. 975 (2008) 1320–1327.
[46] D.T. Blackstock, Fundamentals of physical acoustics, John Wiley & Sons, Inc, New York, (2000).
[47] L.E. Kinsler, A.R. Frey, A.B. Coppens, J.V. Sanders, Fundamentals of acoustics, 4th Edition, Wiley-VCH (1999).
[48] T.P. Philippidis, D.G. Aggelis, Experimental study of wave dispersion and attenuation in concrete, Ultrasonics. 43 (2005) 584–595.
[49] F. Saint-Pierre, P. Rivard, G. Ballivy, Measurement of alkali-silica reaction progression by ultrasonic waves attenuation, Cem. Concr. Res. 37 (2007) 948–956.
[50] A. Ruiz M., P.B. Nagy, Diffraction correction for precision surface acoustic wave velocity measurements, J. Acoust. Soc. Am. 112 (2002) 835–842.
[51] B. Kim, J.-Y. Kim, Characterization of ultrasonic properties of concrete, Mech. Res. Commun. 36 (2009) 207–214.
[52] W. Punurai, J. Jarzynski, J. Qu, J.Y. Kim, L.J. Jacobs, K.E. Kurtis, Characterization of multi-scale porosity in cement paste by advanced ultrasonic techniques, Cem. Concr. Res. 37 (2007) 38–46.
[53] G. Kim, J.-Y. Kim, K.E. Kurtis, L.J. Jacobs, Sensitivity of acoustic nonlinearity parameter to the microstructural changes in cement-based materials, AIP Conf. Proc. 1650 (2015) 1431–1439.
[54] R. Weaver, Ultrasonics in an aluminum foam, 36 (1998).
[55] G. Kim, C.-W. In, J.-Y. Kim, L.J. Jacobs, K.E. Kurtis, Nondestructive detection and characterization of carbonation in concrete, AIP Conf. Proc. 1581 (2014) 805–813.
[56] D.P. Schurr, J.Y. Kim, K.G. Sabra, L.J. Jacobs, Damage detection in concrete using

coda wave interferometry, NDT E Int. 44 (2011) 728–735.
[57] F. Deroo, J.-Y. Kim, J. Qu, K. Sabra, L.J. Jacobs, Detection of damage in concrete using diffuse ultrasound., J. Acoust. Soc. Am. 127 (2010) 3315–3318.
[58] G. Kim, J.-Y. Kim, K.E. Kurtis, L.J. Jacobs, Y. Le Pape, M. Guimaraes, Quantitative evaluation of carbonation in concrete using nonlinear ultrasound, Mater. Struct. 49 (2016) 399–409.
[59] F. Bouchaala, C. Payan, V. Garnier, J.P. Balayssac, Carbonation assessment in concrete by nonlinear ultrasound, Cem. Concr. Res. 41 (2011) 557–559.
[60] Q.A. Vu, V. Garnier, J.F. Chaix, C. Payan, M. Lott, J.N. Eiras, Concrete cover characterisation using dynamic acousto-elastic testing and Rayleigh waves, Constr. Build. Mater. 114 (2016) 87–97.
[61] J.H. Cantrell, Fundamentals and applications of monlinear ultrasonic nondestructive evaluation, CRC Press (2004).
[62] J.-Y. Kim, L.J. Jacobs, J. Qu, J.W. Littles, Experimental characterization of fatigue damage in a nickel-base superalloy using nonlinear ultrasonic waves, J. Acoust. Soc. Am. 120 (2006) 1266–1273.
[63] E.G. Daub, D.R. Shelly, R.A. Guyer, P.A. Johnson, Brittle and ductile friction and the physics of tectonic tremor, Geophys. Res. Lett. 38 (2011) 38–41.
[64] M.C. Remillieux, R.A. Guyer, C. Payan, T.J. Ulrich, Decoupling Nonclassical Nonlinear Behavior of Elastic Wave Types, Phys. Rev. Lett. 116 (2016) 115501.
[65] M. Liu, G. Tang, L.J. Jacobs, J. Qu, A nonlinear wave mixing method for detecting Alkali-Silica reactivity of aggregates, AIP Conf. Proc. 1430 (2012) 1524–1531.
[66] M.A. Breazeale, D.O. Thompson, Finite-amplitude ultrasonic waves in aluminum, Appl. Phys. Lett. 3 (1663) 77–78.
[67] J.H. Cantrell, W.T. Yost, Nonlinear Ultrasonic Characterization of Fatigue Microstructures, Int. J. Fatigue 23 (2001) 487–490.
[68] Y. Shui, I.Y. Solodov, Nonlinear properties of Rayleigh and Stoneley waves in solids, J. Appl. Phys. 64 (2016) 6155–6165.
[69] K.H. Matlack, J.-Y. Kim, L.J. Jacobs, J. Qu, Review of second harmonic generation measurement techniques for material state determination in metals, J. Nondestruct. Eval. 34 (2015) 1–23.
[70] J. Herrmann, Generation and detection of higher harmonics in Rayleigh waves using laser ultrasound, Thesis, Georgia Institute of Technology (2005).
[71] S. V Walker, J. Kim, J. Qu, L.J. Jacobs, NDT & E International Fatigue damage evaluation in A36 steel using nonlinear Rayleigh surface waves, NDT E Int. 48 (2012) 10–15.
[72] A. Ruiz, N. Ortiz, A. Medina, J.Y. Kim, L.J. Jacobs, Application of ultrasonic methods for early detection of thermal damage in 2205 duplex stainless steel, NDT E Int. 54 (2013) 19–26.
[73] S. Thiele, J. Kim, J. Qu, L.J. Jacobs, Air-coupled detection of nonlinear Rayleigh surface waves to assess material nonlinearity, Ultrasonics. 54 (2014) 1470–1475.
[74] J. Herrmann, J.-Y. Kim, L.J. Jacobs, J. Qu, J.W. Littles, M.F. Savage, Assessment of material damage in a nickel-base superalloy using nonlinear Rayleigh surface waves, J. Appl. Phys. 99 (2006) 124913.
[75] D.T. Zeitvogel, K.H. Matlack, J. Kim, L.J. Jacobs, P.M. Singh, J. Qu, NDT & E International Characterization of stress corrosion cracking in carbon steel using

nonlinear Rayleigh surface waves, NDT E Int. 62 (2014) 144–152.
[76] G. Kim, J.-Y. Kim, K.E. Kurtis, L.J. Jaocbs, Drying shrinkage in concrete assessed by nonlinear ultrasound, Cem. Concr. Res. Accepted (2016).
[77] R.A. Guyer, P.A. Johnson, R.A. Guyer, P.A. Johnson, Nonlinear mesoscopic elasticity: Evidence for a new calss, Phys. Today. 52 (1999) 30–36.
[78] J.A. TenCate, E. Smith, R.A. Guyer, Universal slow dynamics in granular solids, Phys. Rev. Lett. 85 (2000) 1020–1023.
[79] K.R. Mccall, R.A. Guyer, Equation of state and wave propagation in hysteretic nonlinear elastic materials, J. Geophys. Res. 99 (1994) 23887–23897.
[80] J. Chen, A.R. Jayapalan, J.-Y. Kim, K.E. Kurtis, L.J. Jacobs, Nonlinear wave modulation spectroscopy method for ultra-accelerated alkali-silica reaction assessment, ACI Mater. J. 106 (2009) 340–348.
[81] R. Snieder, A. Grêt, H. Douma, J. Scales, Coda wave interferometry for estimating nonlinear behavior in seismic velocity, Science 295 (2002) 2253–2255.
[82] E. Larose, S. Hall, Monitoring stress related velocity variation in concrete with a $2x10^{-5}$ relative resolution using diffuse ultrasound., J. Acoust. Soc. Am. 125 (2009) 1853–1856.
[83] F. Moradi-Marani, S.A. Kodjo, P. Rivard, C.P. Lamarche, Nonlinear acoustic technique of time shift for evaluation of alkali-silica reaction damage in concrete structures, ACI Mater. J. 111 (2014) 581–592.
[84] J.N. Eiras, Q.A. Vu, M. Lott, J. Payá, V. Garnier, C. Payan, Dynamic acousto-elastic test using continuous probe wave and transient vibration to investigate material nonlinearity, Ultrasonics 69 (2016) 29–37.
[85] T. Ju, J.D. Achenbach, L.J. Jacobs, M. Guimaraes, J. Qu, Ultrasonic nondestructive evaluation of alkali – silica reaction damage in concrete prism samples, Mater. Struct. (2017) 1–13.
[86] P.K. Mehta, P.J.M. Monteiro, Concrete: Microstructure, Properties, and Materials, Third editon, McGraw-Hill, 2006.
[87] D.P. Bentz, A review of early-age properties of cement-based materials, Cem. Concr. Res. 38 (2008) 196–204.
[88] B. Persson, Experimental studies on shrinkage of high-performance concrete, Cem. Concr. Res. 28 (1998) 1023–1036.
[89] J. Bisschop, J.G.M. Van Mier, Effect of aggregates on drying shrinkage microcracking in cement-based composites, Mater. Struct. 35 (2002) 453–461.
[90] G.W. Scherer, Theory of Drying, J. Am. Ceram. Soc. 73 (1990) 3–14.
[91] Z.P. Bazant, S. Prasannan, Solidification theory for concrete creep. II: Verification and application, J. Eng. Mech. 115 (1990) 1704–1725.
[92] S. Mindess, J.F. Young, D. Darwin, Concrete, Prentice Hall, (2003).
[93] R. Breitenbücher, H. Ibuk, Experimentally based investigations on the degradation-process of concrete under cyclic load, Mater. Struct. 39 (2006) 717–724.
[94] M. Omar, A. Loukili, G. Pijaudier-Cabot, Y. Le Pape, Creep-damage coupled effects: experimental investigation on bending beams with various sizes, J. Mater. Civ. Eng. 21 (2009) 65–72.
[95] C.-L. Hwang, J.F. Young, Drying shrinkage of portland cement pastes I. Microcracking during drying, Cem. Concr. Res. 14 (1984) 585–594.
[96] Z.P. Bazănt, W.J. Raftshol, Effect of cracking in drying and shrinkage specimens,

Cem. Concr. Res. 12 (1982) 209–226.
[97] H.R. Samaha, K.C. Hover, Influence of microcracking on the mass transport properties of concrete, ACI Mater. J. 89 (1992) 416–424.
[98] F. Collins, J.G. Sanjayan, Effect of pore size distribution on drying shrinking of alkali-activated slag concrete, Cem. Concr. Res. 30 (2000) 1401–1406.
[99] M.L. Wilson, S.H. Kosmatka, Design and control of concrete mixtures, Portland Cement Association (PCA):USA (2011).
[100] Z. Grasley, D. Lange, M. D'Ambrosia, Internal relative humidity and drying stress gradients in concrete, Mater. Struct. 39 (2006) 901–909.
[101] J. Castro, D. Bentz, J. Weiss, Effect of sample conditioning on the water absorption of concrete, Cem. Concr. Compos. 33 (2011) 805–813.
[102] P. Grassl, H.S. Wong, N.R. Buenfeld, Influence of aggregate size and volume fraction on shrinkage induced micro-cracking of concrete and mortar, Cem. Concr. Res. 40 (2010) 85–93.
[103] G. Pickett, Effect of aggregate on shrinkage of concrete and a hypothesis concerning shrinkage, J. Proc. 52 (1956) 581–590.
[104] M. Lopez, L.F. Kahn, K.E. Kurtis, Characterization of elastic and time-dependent deformations in high performance lightweight concrete by image analysis, Cem. Concr. Res. 39 (2009) 610–619.
[105] J.S. Nadeau, R. Bennett, S. Mindess, Acoustic emission in the drying of hardened cement paste and mortar, J. Am. Ceram. Soc. 64 (1980) 410–415.
[106] T.R. Naik, V.M. Malhotra, J.S. Popovics, The ultrasonic pulse velocity method, Handbook on nondestructive testing of concrete (2004) 169–188.
[107] D.P. Bentz, M.R. Geiker, K.K. Hansen, Shrinkage-reducing admixtures and early-age desiccation in cement pastes and mortars, Cem. Concr. Res. 31 (2001) 1075–1085.
[108] P. Lura, B. Pease, G.B. Mazzotta, F. Rajabipour, J. Weiss, Influence of shrinkage-reducing admixtures on development of plastic shrinkage cracks, ACI Mater. J. 104 (2007) 187–194.
[109] J. Weiss, P. Lura, F. Rajabipour, G. Sant, Performance of shrinkage-reducing admixtures at different humidities and at early ages, ACI Mater. J. 105 (2008) 478–486.
[110] F. Rajabipour, G. Sant, J. Weiss, Interactions between shrinkage reducing admixtures (SRA) and cement paste's pore solution, Cem. Concr. Res. 38 (2008) 606–615.
[111] V.G. Papadakis, C.G. Vayenas, M.N. Fardis, Experimental investigation and mathematical modeling of the concrete carbonation problem, Chem. Eng. Sci. 46 (1991) 1333–1338.
[112] V.G. Papadakis, C.G. Vayenas, M.N. Fardis, Fundamental modelling and experimental investigation of concrete carbonation, Am. Concr. Inst. Mater. J. 88 (1991) 363–373.
[113] L.J. Parrott, D.C. Killoh, Carbonation in a 36 year old, in situ concrete, Cem. Concr. Res. 19 (1989) 649–656.
[114] C. Dow, F.P. Glasser, Calcium carbonate efflorescence on Portland cement and building materials, Cem. Concr. Res. 33 (2003) 147–154.
[115] M. Fernández Bertos, S.J.R. Simons, C.D. Hills, P.J. Carey, A review of accelerated

carbonation technology in the treatment of cement-based materials and sequestration of CO2, J. Hazard. Mater. 112 (2004) 193–205.
[116] P.J.M. Monteiro, L. Clodic, F. Battocchio, W. Kanitpanyacharoen, S.R. Chae, J. Ha, H.-R. Wenk, Incorporating carbon sequestration materials in civil infrastructure: A micro and nano-structural analysis, Cem. Concr. Compos. 40 (2013) 14–20.
[117] P.A.M. Basheer, S.E. Chidiac, A.E. Long, Predictive models for deterioration of concrete structures, Constr. Build. Mater. 10 (1996) 27–37.
[118] E. Rozière, A. Loukili, F. Cussigh, A performance based approach for durability of concrete exposed to carbonation, Constr. Build. Mater. 23 (2009) 190–199.
[119] G.H. Koch, M.P.H. Brongers, N.G. Thompson, Y.P. Virmani, J.H. Payer, Corrosion cost and preventive strategies in the United States, No. FHWA-RD-01-156 (2002).
[120] K. Kobayashi, Y. Uno, Influence of alkali on carbonation of concrete, part I. Preliminary tests with mortar specimens, Cem. Concr. Res. 19 (1989) 821–826.
[121] G. Villain, G. Platret, Two experimental methods to determine carbonation profiles in concrete, ACI Mater. J. 103 (2006) 265–271.
[122] M. Thiery, G. Villain, P. Dangla, G. Platret, Investigation of the carbonation front shape on cementitious materials : effects of the chemical kinetics, Cem. Concr. Res. 37 (2007) 1047–1058.
[123] D.R. Moorehead, Cementation by the carbonation of hydrated lime, Cem. Concr. Res. 16 (1986) 700–708.
[124] R.B. Holland, Durability of precast prestressed concrete piles in marine environments, Diss, Georgia Institute of Technology (2012).
[125] J. Vanzo, A nanochemomechanical investigation of carbonated cement paste, Thesis. Massachusetts Institute of Technology (2009).
[126] B. Johannesson, P. Utgenannt, Microstructural changes caused by carbonation of cement mortar, Cem. Concr. Res. 31 (2001) 925–931.
[127] J. Jerga, Physico-mechanical properties of carbonated concrete, Constr. Build. Mater. 18 (2004) 645–652.
[128] M.I. Khan, C.J. Lynsdale, Strength, permeability, and carbonation of high-performance concrete, Cem. Concr. Res. 32 (2002) 123–131.
[129] C.D. Atis, Accelerated carbonation and testing of concrete made with fly ash, Constr. Build. Mater. 17 (2003) 147–152.
[130] F.P. Torgal, S. Miraldo, J.A. Labrincha, J. De Brito, An overview on concrete carbonation in the context of eco-efficient construction : Evaluation , use of SCMs and/or RAC, Constr. Build. Mater. 36 (2012) 141–150.
[131] A. Younsi, P. Turcry, E. Rozière, A. Aït-Mokhtar, A. Loukili, Performance-based design and carbonation of concrete with high fly ash content, Cem. Concr. Compos. 33 (2011) 993–1000.
[132] V.G. Papadakis, Effect of supplementary cementing materials on concrete resistance against carbonation and chloride ingress, Cem. Concr. Res. 30 (2000) 291–299.
[133] S. Kamali, M. Moranville, S. Leclercq, Material and environmental parameter effects on the leaching of cement pastes : experiments and modelling, Cem. Concr. Res. 38 (2008) 575–585.
[134] V.G. Papadakis, M.N. Fardis, C.G. Vayenas, Effect of composition, environmental factors and cement-lime mortar coating on concrete carbonation, Mater. Struct. 25 (1992) 293–304.

[135] G. De Schutter, K. Audenaert, Evaluation of water absorption of concrete as a measure for resistance against carbonation and chloride migration, Mater. Struct. 37 (2004) 591–596.
[136] N.I. Fattuhi, Concrete carbonation as influenced by curing regime, Cem. Concr. Res. 18 (1988) 426–430.
[137] V. Rostami, Y. Shao, A.J. Boyd, Z. He, Microstructure of cement paste subject to early carbonation curing, Cem. Concr. Res. 42 (2012) 186–193.
[138] D. Hobbs, Alkali-silica reaction in concrete, Thomas Telford, London, (1988).
[139] K.J. Folliard, M.D Thomas, K.E. Kurtis, Guidelines for the use of lithium to mitigate or prevent ASR, No. FHWA-RD-03-047 (2003).
[140] K.E. Kurtis, P.J.M. Monteiro, J.T. Brown, W. Meyer-Ilse, Imaging of ASR gel by soft X-ray microscopy, Cem. Concr. Res. 28 (1998) 411–421.
[141] X. Hou, R.J. Kirkpatrick, L.J. Struble, P.J.M. Monteiro, Structural investigations of alkali silicate gels, J. Am. Ceram. Soc. 88 (2005) 943–949.
[142] E. Garcia-Diaz, J. Riche, D. Bulteel, C. Vernet, Mechanism of damage for the alkali-silica reaction, Cem. Concr. Res. 36 (2006) 395–400.
[143] R. Helmuth, D. Stark, S. Diamond, M.-R. Micheline, Alkali-silica reactivity: an overview of research, Contract: http://onlinepubs.trb.org/onlinepubs/shrp/SHRP-C-342.pdf. (1993).
[144] J.A. Farny, B. Kerkhoff, Diagnosis and control of alkali-aggregate reactions in concrete, Portl. Cem. Assoc. (1997).
[145] Z.P. Bazant, A. Steffens, Mathematical model for kinetics of alkali-silica reaction in concrete, Cem. Concr. Res. 30 (2000) 419–428.
[146] M.B. Haha, E. Gallucci, A. Guidoum, K.L. Scrivener, Relation of expansion due to alkali silica reaction to the degree of reaction measured by SEM image analysis, Cem. Concr. Res. 37 (2007) 1206–1214.
[147] C.L. Collins, J.H. Ideker, G.S. Willis, K.E. Kurtis, Examination of the effects of LiOH, LiCl, and LiNO3 on alkali-silica reaction, Cem. Concr. Res. 34 (2004) 1403–1415.
[148] X. Feng, M.D.A. Thomas, T.W. Bremner, K.J. Folliard, B. Fournier, New observations on the mechanism of lithium nitrate against alkali silica reaction (ASR), Cem. Concr. Res. 40 (2010) 94–101.
[149] ASTM C1260-14, Standard test method for potential alkali reactivity of aggregates (mortar-bar method), Annual book of ASTM standards, (2014).
[150] ASTM C1293-08, Standard test method for determination of length change of concrete due to alkali-silica reaction, Annual book of ASTM standards, (2008).
[151] M. Thomas, B. Fournier, K. Folliard, J. Ideker, M. Shehata, Test methods for evaluating preventive measures for controlling expansion due to alkali-silica reaction in concrete, Cem. Concr. Res. 36 (2006) 1842–1856.
[152] D. Lu, B. Fournier, P.E. Grattan-Bellew, Evaluation of accelerated test methods for determining alkali-silica reactivity of concrete aggregates, Cem. Concr. Compos. 28 (2006) 546–554.
[153] A.G. Vayghan, F. Rajabipour, J.L. Rosenberger, Composition–rheology relationships in alkali–silica reaction gels and the impact on the Gel's deleterious behavior, Cem. Concr. Res. 83 (2016) 45–56.
[154] S. Multon, A. Sellier, M. Cyr, Chemo-mechanical modeling for prediction of alkali

silica reaction (ASR) expansion, Cem. Concr. Res. 39 (2009) 490–500.
[155] S. Multon, A. Sellier, Multi-scale analysis of alkali-silica reaction (ASR): Impact of alkali leaching on scale effects affecting expansion tests, Cem. Concr. Res. 81 (2016) 122–133.
[156] K.M. Nemati, P.J.M. Monteiro, K.L. Scrivener, Analysis of compressive stress-induced cracks in concrete, ACI Mater. J. 95 (1998) 617–630.
[157] R. John, S.P. Shah, Y.-S. Jeng, A fracture mechanics model to predict the rate sensitivity of mode I fracture of concrete, Cem. Concr. Res. 17 (1987) 249–262.
[158] C. Mazzotti, M. Savoia, Nonlinear creep damage model for concrete under uniaxial compression, J. Eng. Mech.129 (2003) 1065–1075.
[159] M. Lopez, L.F. Kahn, K.E. Kurtis, Characterization of elastic and time-dependent deformations in normal strength and high performance concrete by image analysis, Cem. Concr. Res. 37 (2007) 1265–1277.
[160] P.J. Sereda, R.F. Feldman, E.G. Swenson, Effect of sorbed water on some mechanical properties of hydrated portland cement pastes and compacts, Highway Research Board Special Report 90 (1966).
[161] R.L. Carrasquillo, F.O. Slate, A.H. Nilson, Microcracking and behavior of high strength concrete subjected to short-term loading, ACI J. 78 (1981) 179–186.
[162] M.F. Hamilton, D.T.Blackstock, Nonlinear Acoustics, Academic Press, San Diego, CA, (1998).
[163] J.B. Kim, D.G. Song, K.Y. Jhang, Absolute measurement and relative measurement of ultrasonic nonlinear parameters, Res. Nondestruct. Eval. Accepted (2016).
[164] M. Smith, G. Kim, J.-Y. Kim, K.E. Kurtis, L.J. Jacobs, Second harmonic generation using nonlinear Rayleigh surface waves in stone, AIP Conf. Proc. 1650 (2015) 1423–1430.
[165] ACI Committee 211, Standard practice for selecting proportions for normal, heavyweight and mass concrete, American concrete institute, Farmington Hills, (1991).
[166] ASTM C150/C150M-12, Standard specification for portland cement, Annual book of ASTM standards, (2012).
[167] J. Weiss, P. Lura, F. Rajabipour, G. Sant, Performance of shrinkage redcution admixture at different humidities and at early ages, ACI Materails J. 105 (2008) 478–486.
[168] W.J. Weiss, S.P. Shah, Restrained shrinkage cracking : the role of shrinkage reducing admixtures and specimen geometry, Mater. Struct. 35 (2002) 85–91.
[169] B. Rongbing, S. Jian, Synthesis and evaluation of shrinkage-reducing admixture for cementitious materials, Cem. Concr. Res. 35 (2005) 445–448.
[170] R.P. L Bertolini, B Elsener, P Pedeferri, Corrosion of steel in concrete: prevention, diagnosis, repair, Wiley-VCH, (2004).
[171] S. Haupert, G. Renaud, J. Rivière, M. Talmant, P.A. Johnson, P. Laugier, High-accuracy acoustic detection of nonclassical component of material nonlinearity, J. Acoust. Soc. Am. 130 (2011) 2654–2661.
[172] ASTM C143-15, Standard test method for slump of hydraulic-cement concrete, Annual book of ASTM standards, (2015).
[173] ASTM C138/C138M-13, Standard test method for density (unit weight), yield, and air content (gravimetric) of concrete, Annual book of ASTM standards, (2013).

[174] ASTM C231/C231M-14, Standard test method for air content of freshly mixed concrete by the pressure method, Annual book of ASTM standards, (2014).
[175] ASTM C39-14, Standard test method for compressive strength of cylindrical concrete specimens, Annual book of ASTM standards, (2012).
[176] N. Smaoui, M.A. Bérubé, B. Fournier, B. Bissonnette, B. Durand, Effects of alkali addition on the mechanical properties and durability of concrete, Cem. Concr. Res. 35 (2005) 203–212.
[177] P. Rossi, J.-L. Tailhan, F. Le Maou, L. Gaillet, E. Martin, Basic creep behavior of concretes investigation of the physical mechanisms by using acoustic emission, Cem. Concr. Res. 42 (2012) 61–73.
[178] A. Carpinteri, G. Lacidogna, N. Pugno, Structural damage diagnosis and life-time assessment by acoustic emission monitoring, Eng. Fract. Mech. 74 (2007) 273–289.
[179] J.-F. Chaix, I. Lillamand, M.-A. Ploix, V. Garnier, G. Corneloup, Study of acoustoelasticity behavior of concrete material under uniaxial compression, J. Acoust. Soc. Am. 4 (2008) 045014.
[180] P. Shokouhi, A. Zoëga, H. Wiggenhauser, G. Fischer, Surface wave velocity-stress relationship in uniaxially loaded concrete, ACI Mater. J. 109 (2012) 141–148.
[181] D.P. Schurr, J.Y. Kim, K.G. Sabra, L.J. Jacobs, Damage detection in concrete using coda wave interferometry, NDT E Int. 44 (2011) 728–735.
[182] C. Payan, V. Garnier, J. Moysan, P.A. Johnson, Determination of third order elastic constants in a complex solid applying coda wave interferometry, Appl. Phys. Lett. 94 (2009) 36–39.
[183] S.I. Rokhlin, J.-Y. Kim, In situ ultrasonic monitoring of surface fatigue crack initiation and growth from surface cavity, Int. J. Fatigue. 25 (2003) 41–49.
[184] D.C. Jansen, S.P. Shah, Effect of Length on Compressive Strain Softening of Concrete, J. Eng. Mech. 123 (1997) 25–35.
[185] ASTM C512/C512M-10. Standard test method for creep of concrete in compression, Annual book of ASTM standards, (2010).
[186] G. Sant, B. Lothenbach, P. Juilland, G.L. Saout, J. Weiss, K. Scrivener, The origin of early age expansions induced in cementitious materials containing shrinkage reducing admixtures, Cem. Concr. Res. 41 (2011) 218–229.
[187] E. Fehling, M. Schmidt, S. Stürwald, Ultra high performance concrete (UHPC), Kassel university press GmbH, (2008).
[188] D.J. Shull, E.E. Kim, M.F. Hamilton, E.A. Zabolotskaya, Diffraction effects in nonlinear Rayleigh wave beams, J. Acoust. Soc. Am. 97 (1995) 2126–2137.